AD NUMBER

AD819547

NEW LIMITATION CHANGE

TO

Approved for public release, distribution unlimited

FROM

Distribution authorized to U.S. Gov't. agencies and their contractors; Critical Technology; SEP 1967. Other requests shall be referred to Air Force Arnold Engineering Development Center, Arnold AFB, TN.

AUTHORITY

AEDC/IN Memo, 12 May 1995

AEDC-TR-67-148

COMPARISON OF THEORETICAL AND EXPERIMENTAL PRESSURE AND HEAT-TRANSFER DISTRIBUTIONS ON THREE BLUNT NOSED CYLINDERS IN HYPERSONIC FLOW

R. K. Matthews and R. H. Eaves, Jr.

ARO, Inc.

September 1967

VON KÁRMÁN GAS DYNAMICS FACILITY
ARNOLD ENGINEERING DEVELOPMENT CENTER
AIR FORCE SYSTEMS COMMAND
ARNOLD AIR FORCE STATION, TENNESSEE

NOTICES

When U. S. Government drawings specifications, or other data are used for any purpose other than a definitely related Government procurement operation, the Government thereby incurs no responsibility nor any obligation whatsoever, and the fact that the Government may have formulated, furnished, or in any way supplied the said drawings, specifications, or other data, is not to be regarded by implication or otherwise, or in any manner licensing the holder or any other person or corporation, or conveying any rights or permission to manufacture, use, or sell any patented invention that may in any way be related thereto.

Qualified users may obtain copies of this report from the Defense Documentation Center.

References to named commercial products in this report are not to be considered in any sense as an endorsement of the product by the United States Air Force or the Government.

AEDC-TR-67-148

COMPARISON OF THEORETICAL AND EXPERIMENTAL PRESSURE AND HEAT-TRANSFER DISTRIBUTIONS ON THREE BLUNT NOSED CYLINDERS IN HYPERSONIC FLOW

R. K. Matthews and R. H. Eaves, Jr.
ARO, Inc.

This document is subject to special export controls and each transmittal to foreign governments or foreign nationals may be made only with prior approval of Arnold Engineering Development Center (AETS).

AF - AEDC
Arnold AFS Tenn

FOREWORD

The work reported herein was sponsored by the Arnold Engineering Development Center (AEDC), Air Force Systems Command (AFSC), under Program Element 65402234.

The results of research presented were obtained by ARO, Inc. (a subsidiary of Sverdrup & Parcel and Associates, Inc.), contract operator of AEDC, AFSC, Arnold Air Force Station, Tennessee, under Contract AF40(600)-1200. The work was done under ARO Project Numbers VT3116, VT2715, and VT2707, and the manuscript was submitted for publication on June 23, 1967.

The authors wish to express their appreciation to L. L. Trimmer of the Hypersonic Branch and to P. C. Shelton, Jr., of the Hypervelocity Branch, von Kármán Gas Dynamics Facility (VKF), AEDC, for their assistance in obtaining the experimental data.

This technical report has been reviewed and is approved.

Donald H. Meyer	Leonard T. Glaser
Major, USAF	Colonel, USAF
AF Representative, VKF	Director of Test
Directorate of Test	

ABSTRACT

Pressure and heat-transfer data over flow-aligned cylinders with three nose shapes (hemisphere, flat-face, and rounded-shoulder flat-face) have been obtained at nominal Mach numbers of 6, 8, 10, and 19 and over the Reynolds number range of 0.009 x 10^6 to 2.16 x 10^6, based on model diameter. The experimental pressure and heat-transfer distributions are compared with theoretical predictions and with selected previously published data from other facilities. The agreement between the experimental results and selected theories for the hemisphere cylinder model is good. However, the pressure and heat-transfer distributions on the other two configurations could not be adequately predicted over the entire model surface.

CONTENTS

APPENDIXES

I. ILLUSTRATIONS

II. TABLES

NOMENCLATURE

b	Model skin thickness, ft
C_D	Nose drag coefficient (obtained by integrating the experimental pressure distributions)
C_p	Pressure coefficient, $(p - p_\infty)/q_\infty$
$C_{p_{max}}$	Maximum pressure coefficient, $(p_s - p_\infty)/q_\infty$
c	Model skin specific heat, Btu/lb_m °R
d	Model diameter, in.
H	Total enthalpy, Btu/lb_m
ℓ	Model length, in.
M	Mach number
p	Pressure, psia
q	Dynamic pressure, psia
$\dot{q}$	Heat-transfer rate, Btu/ft^2 sec
R	Model cylinder radius, in.
Re_∞	Free-stream unit Reynolds number, ft^{-1} or $in.^{-1}$ as noted
$Re_{\infty,d}$	Reynolds number based on cylinder diameter
r	Radius of model cross section, in.
s	Distance along model surface measured from forward stagnation point, plus along upper surface, in.
St	Stanton number, $\frac{\dot{q}}{\rho_\infty u_\infty (H_o - H_w)}$

T	Temperature, °R
t	Time, sec
u	Velocity, ft/sec
w	Model skin specific density, lb_m/ft^3
x'	Distance along model axis measured from model bow shock, in.
x''	Distance along model axis measured from nose-cylinder tangency point, in.
Δ	Bow shock stand-off distance, in.
γ	Ratio of specific heats
θ	Angle between a normal to the model surface and the free-stream velocity vector, radians
ρ	Density, lb_m/ft^3
σ	Angle between tangent to model surface and free-stream velocity vector, deg

SUBSCRIPTS

e	Local conditions at the edge of the boundary layer
o	Stilling chamber stagnation conditions
SH	Model shoulder (tangent point) conditions
s	Model stagnation conditions
w	Model wall conditions
∞	Free-stream conditions

SUPERSCRIPT

*	Critical conditions (i.e., conditions where the velocity is equal to the local speed of sound)

SECTION I
INTRODUCTION

The designers of hypersonic configurations must be able to make a reasonable prediction of the flow field around the body in order to estimate vehicle performance and structural loadings. The use of blunt nosed configurations is dictated by the heating problems encountered at hypersonic speeds. Therefore, the designer is faced with the task of predicting the flow field over a blunt nosed body which is characterized by subsonic, transonic, and supersonic flow regions.

The solution of the subsonic and transonic blunt body problem has been the subject of considerable research; various blunt body solutions are reviewed by Van Dyke in Refs. 1 and 2. The supersonic flow field on a blunt body can be obtained from the commonly used method of characteristics. Of course, the validity of theoretical predictions depends upon their agreement with experimental data. However, there is a definite scarcity of experimental data on blunt shapes at hypersonic Mach numbers which can be used to evaluate available theories. This report presents data on a cylinder with three types of nose bluntness (hemisphere, flat-face, and rounded-shoulder flat-face) at Mach numbers 6, 8, 10, and 19.

The hemisphere model is the most commonly studied blunt body and has been designated as an AGARD calibration model (Ref. 3). Clark in Ref. 4 has compiled hemisphere data over a Mach number range of 1.8 to 21 and developed empirical relations for the hemisphere stagnation point velocity gradient, sonic point, and drag coefficient. The flat-face model represents the extreme in nose bluntness and has been investigated analytically by Gold and Holt in Ref. 5. Kemp, Rose, and Detra (Ref. 6) originated the rounded-shoulder flat-face configuration in order to provide a more stringent test of the similarity-type solution used in heat-transfer theories.

The purpose of this report is to (1) evaluate available theories and discuss their range of applicability and (2) make available new data which may be correlated with other experimental data.

SECTION II
APPARATUS

2.1 WIND TUNNELS

The experimental data reported herein were obtained in five of the VKF hypersonic wind tunnels: Gas Dynamic Wind Tunnels, Hypersonic (B), (C), (E), (H), and (F).

2.1.1 Tunnels B, C, and E

Tunnels B and C are continuous, closed-circuit, variable density wind tunnels with axisymmetric contoured nozzles and 50-in.-diam test sections. Tunnel B operates at nominal Mach numbers of 6 and 8 at stagnation pressures from 20 to 250 psia and from 50 to 900 psia, respectively. Tunnel C operates at a nominal Mach number of 10 at stagnation pressures of 200 to 2000 psia. Stagnation temperatures up to 1350°R in Tunnel B and 1900°R in Tunnel C are utilized to prevent liquefaction of the air in the test section. The above operating conditions result in free-stream unit Reynolds numbers from 0.30×10^6 to 5.00×10^6 per foot in Tunnel B and from 0.30×10^6 to 2.35×10^6 per foot in Tunnel C. Tunnel C and its associated equipment are shown in Fig. 1a (top) (Appendix I). Details of Tunnel B are similar to those of Tunnel C. The test section tank and safety doors allow the model to be injected into the tunnels for a test run and then retracted for model cooling or model changes without interrupting the tunnel flow.

Tunnel E, Fig. 1b, is an intermittent, variable density wind tunnel with a flexible-plate-type nozzle and a 12- by 12-in. test section. The tunnel operates at Mach numbers from 5 to 8 at maximum stagnation pressures from 400 to 1600 psia, respectively, and stagnation temperatures sufficient to prevent liquefaction. Minimum stagnation pressures are about one-quarter of the maximum at each Mach number. The maximum free-stream unit Reynolds numbers are 15.6×10^6 and 6.5×10^6 at Mach numbers 5 and 8, respectively.

2.1.2 Tunnels H and F (Hotshots)

Tunnels H and F, Figs. 1c and d, are conical nozzle, hotshot, wind tunnels with 50- and 100-in.-diam test sections, respectively. These wind tunnels use nitrogen as the test gas and operate over a Mach number range of 18 to 21 and a free-stream unit Reynolds number range of 0.03 to 0.80×10^6 per foot. A standard shot is made by directly heating a small volume of nitrogen gas with a high current electric arc. When the electric arc discharges, the initially confined working gas ruptures a diaphragm located near the throat of a convergent-divergent nozzle. The pressurized gas then expands to the test section and dump tank through a conical nozzle (5-deg half-angle for the 50-in. Tunnel H and 4-deg half-angle for the 100-in. Tunnel F) providing useful run times of approximately 30 to 100 msec.

Recent refinements in Tunnel F have advanced its usefulness as a testing device. The recent advancements in Tunnel F (Ref. 7) include a high speed data acquisition system, a flow visualization system, high Reynolds number testing in the main test section and at Mach 15 in an upstream test section, free-flight testing techniques, and increased run times.

A more complete description of the VKF hypersonic wind tunnels may be found in Refs. 7 through 12.

2.2 MODELS AND INSTRUMENTATION

2.2.1 Pressure Models and Instrumentation

The model geometry, the basic model dimensions, and a list of the facilities where the models were tested are shown in Fig. 2. Model pressures were measured in Tunnel B with 15-psid transducers, and in Tunnel C with 1- and 15-psid transducers, switched in and out of the system automatically to allow measuring to the best precision. Model pressures in Tunnel E were measured with 5-psid transducers. From repeat calibrations, the estimated Tunnel B pressure measurement precision was ±0.003 psia. The estimated Tunnel C measurement precision was ±0.001 psia for pressures less than 1 psia and ±0.008 psia for pressures greater than 1 psia. The estimated Tunnel E pressure measurement precision was ±0.5 percent. Additional information concerning the instrumentation systems of the continuous tunnels may be found in Refs. 8 and 12.

Because of the short run times in the hotshot tunnels (30 to 100 msec), close-coupled variable-reluctance pressure transducers have been developed by Smotherman (Ref. 13) for the measurement of pitot and model pressures. The estimated Tunnel H and F pressure measurement precision is as follows:

p/p_s	0.007 to 0.02	0.02 to 1.0
Precision	±10 percent	±5 percent

2.2.2 Heat-Transfer Models and Instrumentation

The heat-transfer data in the continuous tunnels (B and C) were obtained by using thin-skin models (≈0.040 in.) and the transient technique described in Ref. 12. The thin-skin models had thermocouples spot-welded on the interior surface, and the wall thicknesses were measured at each thermocouple location. The hemisphere and flat-face heat-transfer models were constructed of 347 and 310 stainless steel, respectively. Values of specific heats were experimentally determined from samples of the model material for use in the data reduction. The variation of specific heats with temperature was also taken into account in the data reduction.

The estimated precision of the heat-transfer data in the continuous tunnels is as follows:

S_t/St_s	0.05 to 0.2	0.2 to 1.0
Precision	±15 percent	±6 percent

The heat-transfer data in the hotshot tunnels were obtained with calorimeter-type transducers which used thermocouples as temperature sensors. Ledford (Ref. 14) described these transducers in detail, and a complete description of hotshot instrumentation and recording equipment was given by Bynum in Ref. 15.

The estimated precision of the heat-transfer data in the hotshot tunnels is as follows:

St/St_s	0.009 to 0.03	0.03 to 1.0
Precision	±15 percent	±10 percent

SECTION III
PROCEDURE

3.1 TEST CONDITIONS AND PROCEDURES

A summary of the test conditions for the present data, as well as for referenced data, is given in Table I.

Because tunnel free-stream nonuniformities might distort blunt model pressure distributions (Refs. 4, 9, and 16), the models were positioned in the continuous tunnels at axial locations which had relatively uniform free-stream pitot pressure distributions. Also, in most cases, the symmetry of the pressure and heat-transfer distributions was checked by data on both the upper and lower model surfaces.

3.2 DATA REDUCTION

All pressure and heat-transfer distributions presented are nondimensionalized by stagnation point values which are listed in the data tabulations in Appendix II.

In the continuous tunnels, transient heat-transfer data were obtained by injecting the models into the airstream and recording model wall temperatures on magnetic tape at a rate of 20 times every second. A digital computer was used to fit a parabola through 21 consecutive temperature values centered at 0 5 sec after the model reached the tunnel centerline. The temperature-time derivative, dT_w/dt, was then obtained from the parabola and used in the heating rate equation

$$\dot{q} = wbc\, dT_w/dt \quad (1)$$

This equation neglects conduction and radiation losses which have been estimated to be less than 1 percent of the convective heating rates. In the hotshot tunnels, heating rates, $\dot{q}$, were measured directly by the use of calorimeter-type transducers.

Local Stanton numbers were obtained from:

$$St = \frac{\dot{q}}{\rho_\infty u_\infty (H_o - H_w)} \quad (2)$$

In the continuous tunnels, the total enthalpies, H_o and H_w, were calculated using measured values of T_o and T_w and the relationship $H = c_p T$ which assumes c_p = constant. The free-stream conditions in Tunnels B (M_∞ = 6 and 8) and E (M_∞ = 6) were calculated by assuming an isentropic expansion from the stilling chamber and the ideal gas relationships of Ref. 17. The Tunnel C (M_∞ = 10) flow properties were corrected for real gas effects by using the Beattie-Bridgeman equation of state and the procedures of Ref. 18. In the continuous tunnels, the ratio of model wall to tunnel stagnation temperature (T_w/T_o) ranged from approximately 0.25 to 0.50 for heat-transfer models and from 0.70 to 1.0 for pressure models. The method of determining flow conditions in the hotshot tunnels is briefly summarized as follows: instantaneous values of p_o and p_s are measured and an instantaneous value of $\dot{q}_s$ is inferred from a measurement of $\dot{q}_w$ using Lees' distribution (Ref. 19) or measured directly on a 2-in.-diam hemisphere cylinder heat probe (see Refs. 7 and 10). Velocity, hence enthalpy (H_o), is calculated from measured values of p_s, q_s, and the heat probe radius, using Fay-Riddell theory, Ref. 20; Newtonian pressure distribution near the stagnation point and zero dissociation are assumed. With values of p_o, p_s, and H_o known, the remaining flow conditions (M_∞, Re_∞, etc.) are calculated as described in Ref. 21. For the short run times experienced in the hotshot tunnels, the model wall temperature was essentially constant at 540°R (H_w = 133.7 Btu/lb$_m$); thus, the ratio (T_w/T_o) varied between 0.075 and 0.13 yielding "cold wall" conditions.

SECTION IV
THEORIES

This section presents a very brief discussion of the theories that are compared with the data in this report. All theories used are based on nominal free-stream Mach numbers and $\gamma = 1.4$, unless otherwise noted.

4.1 MODIFIED NEWTONIAN AND MODIFIED NEWTONIAN-PRANDTL-MEYER

In Ref. 22, Hayes and Probstein presented a thorough analysis of Newtonian theory and developed the equation

$$C_p = 2 \sin^2 \sigma \tag{3}$$

Lees (Ref. 23) suggested that for a blunt body with a detached bow shock the Newtonian theory could be modified to match stagnation point conditions by letting

$$C_p = C_{p_{max}} \sin^2 \sigma \tag{4}$$

where

$$C_{p_{max}} = \frac{p_s - p_\infty}{q_\infty}$$

Equation (4) may be written as:

$$\frac{p}{p_s} = \sin^2 \sigma + \frac{p_\infty}{p_s} \cos^2 \sigma \tag{5}$$

The modified Newtonian theory as used in this report is represented by Eq. (5).

In Ref. 24, Lees and Kubota developed the Modified Newtonian-Prandtl-Meyer theory. They showed that by matching the Newtonian pressure and pressure gradient with that given by the Prandtl-Meyer relation, better agreement with experimental pressure data was obtained in the hemisphere shoulder region ($1.0 < s/R < 1.6$). Wagner presented matching conditions as a function of free-stream Mach number in Ref. 25.

4.2 NUMERICAL SOLUTIONS

Numerical solutions using the inverse method suggested by Van Dyke (Ref. 1), and matched with the characteristic solution at $M_W \approx 1.05$, have been computed for the hemisphere cylinder model.

The inverse method starts with given free-stream conditions and an assumed shock shape. The flow equations from the shock to the body are then numerically integrated by a marching technique until the body shape producing the assumed shock is determined. The shock shape is iterated until the desired body is produced. As pointed out by Vaglio-Laurin and Ferri (Ref. 26), the basic weakness of the inverse method seems to be that slightly different shock shapes, which are difficult to distinguish from each other, can lead to radically different body shapes. This is one of the reasons that numerical solutions are presented only for the hemisphere cylinder model.

At high Mach numbers and sufficiently low Reynolds numbers (viz. hotshot tunnel conditions), boundary-layer effects become very important, as illustrated in Refs. 27, 28, and 29. Because of the thick boundary layers at these conditions, the "effective" body undergoes significant changes and can be approximated by adding the boundary-layer displacement thickness to the original geometric body. In this report, the method given in Ref. 27 was used to obtain the hemisphere cylinder numerical solutions for the conditions in Tunnels H and F. The inviscid flow field in an ideal (point) source flow was iterated with a viscous boundary-layer solution until there was negligible change in the "effective" body geometry and thus in the pressure distribution along the model. When boundary-layer effects were considered, the ideal source flow field in the inviscid layer was used for only the characteristics solution and not the Van Dyke blunt body solution. When boundary-layer effects were not considered (i. e. inviscid predictions), both the blunt body and characteristic solutions were based on parallel flow.

4.3 BELOTSERKOVSKII'S METHOD

The Belotserkovskii method of predicting the pressure distribution on a blunt body consists of dividing the shock layer, the region between the blunt nose and the detached shock wave, into one, two, or more strips depending on the accuracy desired. The equations of motion are integrated from the body to the boundary of each strip. The boundary conditions are obtained from conditions on the axis of symmetry and at the sonic point, which is fixed at the sharp corner on a flat-face model.

The application of Belotserkovskii's method to the configurations investigated in this report is limited to that presented by Gold and Holt in Ref. 5. They have obtained the first approximation to the flat-face model pressure distribution at $M_\infty = 5.8$.

4.4 VINOKUR'S SOLUTION

While Newtonian theory is remarkably accurate for spherical noses, it becomes very poor for blunter shapes as will be shown. Vinokur (Ref. 30) developed an approximate analytic solution for blunt body inviscid hypersonic flow based on a constant-density assumption. The use of this solution gives results which are not expected to be valid past the sonic point. This method is illustrated in Ref. 31 where the pressure distributions on a flat-face model, as well as on other configurations, was presented as a function of the density ratio across the detached shock wave. This ratio is the only parameter which need be specified when using the constant-density solution.

4.5 BLAST ANALOGY

The sudden, concentrated energy addition to the flow by a blunt nose body at hypersonic speeds may be regarded as analogous to an explosive release of energy. Lukasiewicz (Ref. 32) used this analogy and hypersonic small disturbance theory to develop simple equations which predict the pressure distribution and shock shape on axisymmetric bodies. The second approximation equation for the pressure distribution on axisymmetric bodies which was used in this report is as follows:

$$\frac{p}{p_\infty} = 0.067\ \frac{M_\infty^2\sqrt{C_D}}{x'/d} + 0.44 \tag{6}$$

The C_D values were obtained by integrating the pressure data and the x' values include the shock stand-off distance, Δ. Schlieren or shadowgraph pictures were used to determine the shock stand-off distances, and these values are tabulated later. In most cases the blast analogy is presented in terms of the ratio p/p_S which was obtained by multiplying Eq. (6) by p_∞/p_S, values of which are listed in the figures.

4.6 LOVE'S EQUATION

The deficiencies of blast wave theory in the prediction of inviscid induced pressures are mainly in two regions: near the nose and far downstream (viz., $p/p_\infty < 1.0$). Love (Ref. 33) used the blast wave pressure decay laws (Ref. 34) and attempted to correct these deficiencies. Love's equation is:

$$\frac{p}{p_s} = \left[\frac{1}{1+\left(\frac{x''}{d}\right)}\right]\frac{p_{SH}}{p_s} + \left\{\left[\frac{1}{1+\left(\frac{1}{\frac{x''}{d}}\right)}\right]^{\left(p_{SH}/p_\infty\right)}\right\}\left(\frac{p_\infty}{p_s}\right) \tag{7}$$

This expression assumes a known shoulder pressure ratio, p_{SH}/p_s, and decays from this ratio toward the free-stream static pressure ratio, p_∞/p_s, as the axial distance downstream increases. Of course, the question arises as to what value of shoulder pressure ratio should be used. For the hemisphere model at hypersonic Mach numbers, Love suggested a value of $p_{SH}/p_s = 0.045$ which agrees well with most of the present data and is the value used in this report. Clark's empirical equation (Ref. 4) predicted shoulder pressure ratios which were 4 and 16 percent higher than Love's value at Mach numbers 19 and 6, respectively; however, Clark's fairing included viscous effects and Mach numbers considerably below 6.

Attempting to predict the afterbody pressure distribution on the flat-face cylinder model by Love's method points out the main shortcoming in applying Love's equation. That is, the shoulder pressure for this model cannot be predicted and, in fact, the data show that it varies by approximately two orders of magnitude around the sharp corner. For this reason, Love's equation is not used to predict the afterbody pressures on the flat-face cylinder model.

The application of Love's expression to the rounded-shoulder flat-face cylinder is also somewhat questionable. However, since there is a well defined shoulder pressure at the tangency point of the nose and afterbody, the data are compared with Love's equation. From the present data, a shoulder pressure ratio of $p_{SH}/p_s = 0.045$ was used for Mach numbers 6, 8, and 10 and a value of $p_{SH}/p_s = 0.0585$ was used at Mach number 19 for the rounded-shoulder flat-face model.

4.7 LEES' THEORY

Lees discussed laminar heat-transfer distributions over blunt-nosed bodies at hypersonic speeds in Ref. 19 and developed the equation:

$$\frac{\dot{q}_w}{\dot{q}_s} = \frac{\left(\frac{1}{2}\right)\left(\frac{p}{p_s}\right)\left(\frac{u_e}{u_\infty}\right) r}{\left[\int_0^s \left(\frac{p}{p_s}\right)\left(\frac{u_e}{u_\infty}\right) r^2 \, ds\right]^{1/2}} \left\{\frac{R^{1/2}}{\left[\left(\frac{1}{u_\infty}\right)\left(\frac{du_e}{d\theta}\right)_s\right]^{1/2}}\right\} \tag{8}$$

for bodies of revolution. Given a pressure distribution, local conditions at the edge of the boundary layer (denoted by subscript e) can be calculated by assuming an isentropic expansion from the stagnation conditions behind a normal shock (denoted by subscript s). Stagnation point velocity gradients, $(du_e/d\theta)_s$, were experimentally investigated by Trimmer in Ref. 35. He correlated $[dM_e/d(s/s^*)]_s$ for blunt bodies at Mach numbers 6, 8, and 10. In order to use this correlation parameter, it is necessary to modify the bracketed quantity { } in Eq. (8). By using perfect gas isentropic flow relationships it can be shown that

$$\left\{ \frac{R^{1/2}}{\left[\left(\frac{1}{u_e}\right)\left(\frac{du_e}{d\theta}\right)\right]_s^{1/2}} \right\} \approx \frac{M_\infty^{1/2}\, R^{1/2}}{\left\{\left(\frac{T_o}{T_\infty}\right)^{1/2}\left[\frac{dM_e}{d\left(\frac{s}{R}\right)}\right]_s\right\}^{1/2}} \tag{9}$$

For the hemisphere model, $dM_e/d\left(\frac{s}{R}\right) = dM_e/\theta^* d\left(\frac{s}{s^*}\right)$ where $\theta^* \approx 0.72$ radians. For the flat-face model, $dM_e/d\left(\frac{s}{R}\right) = dM_e/d\left(\frac{s}{s^*}\right)$, since $s^* = R$ and for the rounded-shoulder flat-face model, $dM_e/d\left(\frac{s}{R}\right) \approx d\left(\frac{s}{s^*}\right)$. The values of $dM_e/d\left(\frac{s}{s^*}\right)$ used in this report are tabulated below:

Model	$dM/d\left(\frac{s}{s^*}\right)$	Source
Hemisphere	0.97	Numerical solution
Flat-face	0.29	Ref. 35; data
Rounded-shoulder flat-face	0.29	Ref. 35; implied from geometry and data correlation

SECTION V
RESULTS AND DISCUSSION

This section compares the present data with the theories discussed in Section IV and with previously published data acquired at hypersonic Mach numbers*. The pressure data over the models are presented in two groups of figures. The first group, Figs. 3 through 8, includes the

*The presentation of previous data is approximate since in many cases the data were taken from figures without fine grids.

pressure distribution from the stagnation point to the nose-cylinder tangency point. The tangency points in terms of s/R for the three models are given below:

Model	s/R
Hemisphere cylinder	1.57
Flat-face cylinder	1.00
Rounded-shoulder flat-face cylinder	1.14

The second group, Figs. 9 through 16, includes the cylindrical afterbody pressure distributions. Both the nose and afterbody heat-transfer data are presented as a single group, Figs. 17 through 21, since there is a very limited amount of afterbody heat-transfer data. The present data and the corresponding free-stream conditions may be found in Tables II through VI.

5.1 MODEL NOSE PRESSURE DISTRIBUTIONS

Theories and data on the hemisphere model at Mach numbers 6, 8, 10, and 19 are compared in Figs. 3a through d, respectively. Both the numerical solution (Van Dyke and characteristics based on inviscid parallel flow) and the modified-Newtonian Prandtl-Meyer theories are in good agreement with the data. As expected there was no discernible Reynolds number trend. In Fig. 3, as well as many of the following figures, data are presented from both the upper and lower model surfaces. These data are denoted by the same symbol appearing twice and normally coincide as they should for symmetric models. However, in some instances there is a discernible difference. This difference can probably be attributed to either data precision limitations or free-stream flow non-uniformity effects. In order to minimize these adverse effects and also for reasons of clarity, data at different Reynolds numbers are averaged in cases where there was no significant Reynolds number trend. An average of the present hemisphere data at each Mach number is compared in Fig. 4 with published data obtained after 1957. A similar comparison, Fig. 4 in Ref. 41, shows data obtained prior to 1957. The numerical solution predicts a very slight Mach number effect which is not discernible in the scatter of the data.

Theories and data on the flat-face model are compared in Fig. 5. Modified Newtonian theory does not provide a reasonable prediction of the pressure distribution on this model since it predicts a constant value of p/p_s over the entire model face. In Ref. 22, Hayes and Probstein suggested that better agreement between the data and Newtonian theory might be obtained if the shock angle were used rather than the body angle.

However, because of the difficulty of predicting blunt body shock shapes and other practical application problems, the body angle is normally used as was the case in this report. Vinokur's method yields the correct trend for the pressure distribution, but shows an increasing underprediction in level as the shoulder is approached. Belotserkovskii's first approximation (shown in Fig. 5a), although somewhat low near the shoulder, gives the best prediction of the pressure distribution on the flat-face model. Gold and Holt (Ref. 5) indicated that even better results could be attained with additional approximations. Again, as expected, no Reynolds number effect is indicated.

The averaged present data are compared in Fig. 6 with Belotserkovskii's solution as well as with previously published flat-face model pressure data. The $M_\infty \leq 10$ data agree quite well with only the Mach 19 data indicating a few percent departure from the data fairing; however, considering the precision of the Mach 19 data (see Fig. 5d) no further conclusions can be drawn.

A comparison of modified Newtonian theory with data obtained on the rounded-shoulder flat-face model at Mach numbers 6, 8, 10, and 19 is shown in Figs. 7a through d. Modified Newtonian theory is the only theory that is readily applicable to this model; however, the theory is as much as 25 percent high for $s/R \approx 0.8$. Averaged data at each Mach number are compared in Fig. 8 for the rounded-shoulder flat-face model and, as with the other models, there is no significant Mach number effect. The lack of Mach number effects on blunt nose bodies has been discussed by several authors (see Ref. 44 for example) and is referred to as the independence principle.

5.2 MODEL AFTERBODY PRESSURE DISTRIBUTIONS

Theoretical and experimental pressure distributions on the hemisphere cylinder model are compared in Fig. 9. The method of characteristics shows the best agreement with the data, although the data are generally a few percent high which may be caused by the boundary-layer growth along the model. However, if boundary-layer effects were the cause, the pressures would decrease for a sufficiently large increase in Reynolds number; but this trend is not detectable over the Reynolds number range investigated. Figure 9e does show that in the shoulder region ($s/R \approx 2$), the viscid predictions which include source flow and boundary-layer effects (source flow effects are negligible for the Tunnel F data) provide a significant improvement over the inviscid prediction shown in Fig. 9d. In Ref. 27, Eaves and Lewis provided additional insight into viscous and source flow effects on a hemisphere cylinder at conditions similar to those of Figs. 9d and e. The deficiencies in the blast analogy are seen mainly in two regions; near the nose at all Mach numbers (Figs. 9a through d) and far downstream at the lowest Mach number (Fig. 9a).

Love's equation, based on the blast wave pressure decay laws and empirically matched at the shoulder and far downstream, is as much as 25 percent below the data in some regions (e.g., Fig. 9c, $s/R \approx 8$). The sensitivity of Love's equation to shoulder pressure ratio (p_{SH}/p_s) is shown in Fig. 9a where two shoulder pressure ratios are assumed (Love's value of 0.045 and Clark's value of 0.053). Better agreement is obtained with Clark's value even though it is approximately 10 percent higher than the present shoulder data.

A comparison of an average of the present hemisphere cylinder pressure data at each Mach number with previously published data and with inviscid characteristics solutions is shown in Fig. 10. The agreement among the data and with the theory at similar Mach numbers is considered good. There is an obvious Mach number effect on the cylindrical afterbody; however, the shoulder pressures appear to be independent of Mach number and do not exhibit the trend predicted by the inviscid characteristic solutions. In fact, the shoulder pressures for $M_\infty > 5$ are within 6 percent of Love's value of 0.045. Also shown in Fig. 10 are free-stream static pressures at various Mach numbers calculated from an isentropic expansion ($\gamma = 1.4$). For $s/R \approx 13$, the Mach number 5 and 6 cylinder pressures are slightly overexpanded, whereas the pressures at higher Mach numbers shown an increasing degree of underexpansion.

Comparisons of the blast analogy with flat-face cylinder pressure data are presented in Fig. 11. The blast analogy prediction is within 10 percent of the data for $s/R > 5$ at all Mach numbers. For $s/R < 5$, the agreement is poor. Lukasiewicz (Ref. 32) points out that the blast analogy should not be expected to apply in the nose region since the assumptions of hypersonic small disturbance theory are violated. The difficulties of applying other theories to this model were discussed in Section IV. As mentioned previously, the shoulder pressure ($s/R \approx 1$) varies by approximately two orders of magnitude because of the extreme overexpansion around the sharp corner, and therefore, the application of Love's equation would be somewhat arbitrary. There was no detectable Reynolds number effect on the flat-face cylinder for $s/R > 3$. The effect of Reynolds number on the pressure distribution for $s/R < 3$ is best depicted in Fig. 11c. Figure 12 shows a separation bubble occurring in this region at $M_\infty = 6$ and $Re_{\infty_d} = 1.68 \times 10^6$ in VKF Tunnel E.

The exact mechanism of this separation is not obvious; however, it appears to be a combination of leading-edge separation (caused by the sharp corner) and separation caused by the adverse pressure gradient provided by the inviscid flow field. These two types of separation were described in Ref. 46.

Averaged pressure data at each Mach number are compared in Fig. 13 for the flat-face cylinder model. Data in the region where there was a Reynolds number effect ($1.0 < s/R < 2.3$) were not averaged. In general, the flat-face cylinder afterbody trends are similar to those exhibited on the hemisphere cylinder model (Fig. 10).

Comparisons of theories and rounded-shoulder flat-face cylinder pressure data are shown in Fig. 14. The blast analogy prediction is within approximately 10 percent of the data at all Mach numbers for values of $s/R > 5$. Love's prediction is as much as 45 percent below the data ($s/R \approx 8$), which demonstrates the magnitude of the error which can be encountered by indiscreet application of Love's theory. Even though there is a well defined shoulder pressure, it exists in a region of over-expanded pressures for $6 \leq M_\infty \leq 10$ and therefore the pressure increases immediately downstream while Love's equation predicts a pressure decrease. For $M_\infty = 19$ (Fig. 14d), Love overpredicts the rate of pressure decrease immediately downstream of the tangent point. As with the other models, there is no significant Reynolds number effect for $s/R > 3$ over the range investigated. Averaged pressure data at each Mach number are compared in Fig. 15 for the rounded-shoulder flat-face cylinder model.

As mentioned previously, the cylindrical afterbody pressure distributions at all Mach numbers exhibit similar trends. These trends are correlated by the blast analogy in Fig. 16. The x'/d coordinate is referenced to the bow shock location at the stagnation point (i.e., includes the stand-off distance). This choice of reference provided correlation nearer the shoulder than would be possible if the stand-off distances were neglected. Integrated pressure drag coefficients and values of shock stand-off distance ratioed to model diameter are tabulated in Fig. 16 for each configuration.

5.3 HEAT-TRANSFER DISTRIBUTIONS

Lees' distribution theory compared with hemisphere cylinder heat-transfer data at Mach numbers 8, 10, and 19 is shown in Figs. 17a through c. For $St/St_s > 0.2$, 95 percent of the data were within ±6 percent of Lees' theoretical distribution. For $St/St_s < 0.2$, random deviations from the theory of ±25 percent were observed. Since the hemisphere pressure data showed only slight viscous effects (primarily in the tangency region), no significant Reynolds number effects would be expected on the heat-transfer model and none were noted.

Figure 18 compares an average of the present hemisphere model heat-transfer data at each Mach number with some previously published data and with Lees' distribution at $M_\infty = 8$ and 19. The agreement among the data and with the theory is considered good. The scatter in the data below $St/St_s \approx 0.1$ is caused by the difficulty of measuring low heating rates. Laumann discussed this problem in Ref. 47.

In Figs. 19a and b, comparisons are presented between Lees' distribution theory, based on the empirical pressure data fairing of Fig. 6 and flat-face heat-transfer data at Mach numbers 10 and 19. The scatter in the data ($s/R < 1$) for a given Reynolds number and s/R imply that the heat-transfer distribution on this model is more difficult to measure than that of the hemisphere model since this type of scatter does not appear in the hemisphere heat-transfer data. This data scatter may be caused by an increased sensitivity of the flat-face model to free-stream flow nonuniformities as compared to the hemisphere model.

For $1 < s/R < 3$, the pressure data on the flat-face cylinder model exhibited a Reynolds number effect as was shown in Fig. 11c. A similar effect is indicated in Fig. 19b which shows the heat-transfer distribution on the flat-face cylinder model.

In Fig. 20 an average of the present flat-face model heat-transfer data at each Mach number is compared with the Lees' distribution of Fig. 19. Data in the region of the separation bubble were not averaged. For $s/R < 1$, 93 percent of the data are within +8 percent and -1 percent of Lees' predictions.

Lees' distribution theory is compared with rounded-shoulder flat-face cylinder heat-transfer data at $M_\infty = 19$ in Fig. 21. Lees' distribution is based on the pressure data fairing of Fig. 14d and is approximately 30 percent above the data for $s/R > 1$. Kemp, Rose, and Detra (Ref. 6) implied that their theory provides a better prediction of the heat-transfer distribution on this model. Unfortunately, detailed calculations of their theory for conditions corresponding to the present data are not available.

SECTION VI
CONCLUDING REMARKS

Pressure and heat-transfer data over flow-aligned cylinders with three nose shapes (hemispherical, flat-face, and rounded-shoulder flat-face) have been obtained at Mach numbers of 6, 8, 10, and 19 and over the Reynolds number range of 0.009×10^6 to 2.16×10^6, based on model diameter. The experimental pressure and heat-transfer distributions were compared with previously published data from other facilities and with applicable theories. The agreement among the data from the various facilities is considered very good. The limitations and range of applicability of the theories discussed showed that considerable care must be exercised when attempting to predict the pressure and/or heat-transfer distributions on even such basic configurations as those investigated in this report. The theories investigated were:

1. Modified Newtonian
2. Modified Newtonian Prandtl-Meyer
3. Van Dyke and characteristic solution (inviscid)
4. Van Dyke and characteristic solution (viscid)
5. Belotserkovskii's Method
6. Vinokur's Solution
7. Blast Analogy
8. Love's Equation
9. Lees' theory based on a theoretical pressure distribution
10. Lees' theory based on an empirical pressure distribution

A summary of the comparisons between the present data and the above theories is given in the following table.

Configurations ↓	Model Regions					
	Nose $0 < s/R \leq 0.9$		Shoulder $0.9 < s/R \leq 5$		Afterbody $5 < s/R \leq 15$	
	Pressure	Heat Transfer	Pressure	Heat Transfer	Pressure	Heat Transfer
Hemisphere Cylinder	② ③	⑨	④	⑨	③	ID
Flat-Face Cylinder	⑤	⑩	NA	NA	⑦	ID
Rounded-Shoulder Flat-Face Cylinder	N	N	N	N	⑦	ND

Legend: ⓧ Indicates that theoretical prediction number x (from above) was within ±10 percent of the VKF data at all Mach numbers over the entire s/R range listed.

N Indicates that none of the theories investigated were within ±10 percent of the VKF data.

NA Indicates that none of the theories investigated were applicable.

ND Indicates no data

ID Indicates insufficient data

REFERENCES

1. Van Dyke, M. E. "The Supersonic Blunt Slender Body Problem - Review and Extension." Journal of the Aeronautical Sciences, Vol. 25, 1958, pp. 485-495.

2. Van Dyke, M. D. "The Blunt Body Problem Revisited." Fundamental Phenomena in Hypersonic Flow, Cornell University Press, 1966, pp. 52-64.

3. AGARD Wind Tunnel and Model Testing Panel. "AGARD Wind Tunnel Calibration Models." AGARD Specification 2, September 1957.

4. Clark, E. L. "Hemisphere-Cylinder Pressure Distributions at Supersonic and Hypersonic Mach Numbers." AEDC-TR-66-179 (AD804001), December 1966.

5. Gold, R. and Holt, M. "Calculation of Supersonic Flow Past a Flat-Head Cylinder by Belotserkovskii's Method." AFOSR TN-59-199, March 1959.

6. Kemp, N. H., Rose, P. H., and Detra, R. W. "Laminar Heat Transfer around Blunt Bodies in Dissociated Air." Journal of the Aeronautical Sciences, Vol. 26, July 1959, pp. 421-430.

7. Weddington, E. D. and Griffith, B. J. "Calibration and Status of the AEDC-VKF 100-Inch Hotshot Tunnel F." AEDC-TR-66-191 (AD800778), October 1966.

8. Test Facilities Handbook (6th Edition). "von Kármán Gas Dynamics Facility, Vol. 4." Arnold Engineering Development Center, November 1966.

9. Sivells, J. C. "Aerodynamic Design and Calibration of the VKF 50-Inch Hypersonic Wind Tunnels." AEDC-TDR-62-230 (AD299774), March 1962.

10. Ball, H. W. "Calibration of the 100-Inch Hypervelocity Tunnel." AEDC-TDR-63-46 (AD298279), March 1963.

11. Lukasiewicz, J., Whitfield, J. D., and Jackson, R. "Aerodynamic Testing at Mach Numbers 15 to 22." Hypersonic Flow Research, Vol. 7, Academic Press, pp. 473-512, 1962.

12. Howard, C. M. and Wood, H. T., Jr. "Mechanical Design of the 50-Inch Mach 10-12 Tunnel." AEDC-TDR-62-299 (AD402781), April 1963.

13. Smotherman, W. E. "A Miniature Wafer-Style Pressure Transducer." AEDC-TR-60-11 (AD243875), October 1960.

14. Ledford, R. L. "A Device for Measuring Heat-Transfer Rate in Arc-Discharge Hypervelocity Wind Tunnels." AEDC-TDR-62-64 (AD275740), May 1962.

15. Bynum, D. S. "Instrumentation for the AEDC/VKF 100-Inch Hotshot Tunnel F." AEDC-TR-66-209 (AD804567), December 1966.

16. Cooper, M. and Mayo, E. E. "Measurements of Local Heat Transfer and Pressure on Six 2-Inch-Diameter Blunt Bodies at a Mach Number of 4.95 and at Reynolds Numbers per Foot Up to 81 x 10^6." NASA Memo 1-3-59L, March 1959.

17. Ames Research Staff. "Equations, Tables, and Charts for Compressible Flow." NACA Report 1135, 1953.

18. Randall, R. E. "Thermodynamic Properties of Air: Tables and Graphs Derived from the Beattie-Bridgeman Equation of State Assuming Variable Specific Heats." AEDC-TR-57-8 (AD135331), August 1957.

19. Lees, L. "Laminar Heat Transfer over Blunt-Nosed Bodies at Hypersonic Flight Speeds." Jet Propulsion, Vol. 26, No. 4, 1956, pp. 259-269.

20. Fay, J. A. and Riddell, F. R. "Theory of Stagnation Point Heat Transfer in Dissociated Air." Journal of the Aeronautical Sciences, Vol. 25, 1958, pp. 73-85.

21. Grabau, Martin, Smithson, H. K., Jr., and Little, Wanda J. "A Data Reduction Program for Hotshot Tunnels Based on the Fay-Riddell Heat-Transfer Rate Using Nitrogen at Stagnation Temperatures from 1500 to 5000°K." AEDC-TDR-64-50 (AD601070), June 1964.

22. Hayes, W. D. and Probstein, R. F. Hypersonic Flow Theory, Vol. 5, Academic Press, 1959, pp. 70.

23. Lees, Lester. "Hypersonic Flow." Fifth International Aeronautical Conference (Los Angeles, California, June 20-23, 1955), Institute of the Aeronautical Sciences, pp. 241-276.

24. Lees, L. and Kubota, T. "Inviscid Hypersonic Flow over Blunt-Nosed Slender Bodies." Journal of the Aeronautical Sciences, Vol. 24, No. 3, March 1957.

25. Wagner, Richard D., Jr. "Some Aspects of the Modified Newtonian and Prandtl-Meyer Expansion Method for Axisymmetric Blunt Bodies at Zero Angle of Attack." Journal of the Aeronautical Sciences, Vol. 26, 1959, pp. 851-852.

26. Vaglio-Laurin, R. and Ferri, A. "Theoretical Investigation of the Flow Field around Blunt-Nosed Bodies in Supersonic Flight." Journal of the Aeronautical Sciences, Vol. 25, 1958, pp. 761-770.

27. Eaves, R. H., Jr., and Lewis, C. H. "Combined Effects of Viscous Interaction and Ideal Source Flow on Pressure and Heat-Transfer Distributions over Hemisphere Cylinders at $M_\infty = 18$." AEDC-TR-65-158 (AD467447), July 1965.

28. Lewis, Clark H. and Whitfield, Jack D. "Theoretical and Experimental Studies of Hypersonic Viscous Effects." Paper presented at AGARD Specialists' Meeting on "Recent Developments in Boundary Layer Research." Naples, Italy, May 1965, Vol. III, AGARDograph 97.

29. Whitfield, Jack D. and Griffith, B. J. "Hypersonic Viscous Drag Effects on Blunt Slender Cones." AIAA Journal, Vol. 2, No. 10, October 1964, pp. 1714-1722.

30. Vinokur, M. "Hypersonic Flow around Bodies of Revolution which Are Generated by Conic Sections." Sixth Midwestern Conference of Fluid Mechanics (University of Texas, Austin, Texas, September 1959), pp. 232-253.

31. Vinokur, M. "The Distribution of Velocity, Pressure, and Laminar Heat Transfer on Blunt Bodies in Hypersonic Flow." LMSC/894815, Aerophysics Technical Note 3, May 1961.

32. Lukasiewicz, J. "Hypersonic Flow-Blast Analogy." AEDC-TR-61-4, June 1961; "Blast-Hypersonic Flow Analogy, Theory and Application." ARS Journal, Vol. 32, No. 9, September 1962, pp. 1341-1346.

33. Love, E. S. "Prediction of Inviscid Induced Pressures from Round Leading Edge Blunting at Hypersonic Speeds." ARS Journal, October 1959, pp. 792-794.

34. Cheng, H. K. and Pallone, A. J. "Inviscid Leading-Edge Effect in Hypersonic Flow." Journal of Aeronautical Sciences, Vol. 23, July 1956, pp. 700-702.

35. Trimmer, L. L. "A Study of the Blunt-Body Stagnation Point Velocity Gradient in Hypersonic Flow." Thesis, University of Tennessee, 1966.

36. Baer, A. L. "Pressure Distributions on a Hemisphere Cylinder at Supersonic and Hypersonic Mach Numbers." AEDC-TN-61-96 (AD261501), August 1961.

37. Kendall, J. M., Jr. "Experiments on Supersonic Blunt-Body Flows." Jet Propulsion Progress Report No. 20-372, February 1959.

38. Crawford, D. H. and McCauley, W. D. "Investigation of the Laminar Aerodynamic Heat-Transfer Characteristics of a Hemisphere-Cylinder in the Langley 11-Inch Hypersonic Tunnel at a Mach Number of 6.8." NACA Report 1323, 1957.

39. Reichle, H. G., Jr. "Hemisphere-Cylinder Pressure Distributions at Subsonic, Transonic, and Supersonic Mach Numbers." MTP-AERO-62-30, March 1962.

40. Ellison, R. K. "Turbulent Reference, Roughness, Leakage, and Pressure Tests for the Boeing Company Conducted in the CAL 48-Inch Hypersonic Shock Tunnel." CAL Report No. AA-1661-Y-1, June 1962.

41. Winkler, E. M. and Danberg, J. E. "Heat-Transfer Characteristics of a Hemisphere Cylinder at Hypersonic Mach Numbers." NAVORD Report 4259, April 1957.

42. Chones, A. J. "Heat-Transfer and Pressure Measurements on Flat-Faced Flared-Tail Circular Cylinders and Normal Disks." NAVORD Report 6669, June 1959.

43. Boison, J. C. and Curtiss, H. A. "An Experimental Investigation of Blunt Body Stagnation Point Velocity Gradient." ARS Journal, Vol. 29, February 1959, pp. 130-135.

44. Cox, R. N. and Crabtree, L. F. Elements of Hypersonic Aerodynamics, Academic Press, 1965, pp. 33-42.

45. Kuehn, Donald M. "Experimental and Theoretical Pressures on Blunt Cylinders for Equilibrium and Nonequilibrium Air at Hypersonic Speeds." NASA TN D-1979, November 1963.

46. Chapman, D. R., Kuehn, D. M., and Larson, H. K. "Investigation of Separated Flows in Supersonic and Subsonic Streams with Emphasis on the Effect of Transition." NACA TN 3869, March 1957.

47. Laumann, E. A. "Determining Aerodynamic Heating Rates Using Calorimetric Models in the Jet Propulsion Laboratory Hypersonic Wind Tunnel." JPL Technical Memorandum No. 33-121, March 1963.

APPENDIXES

I. ILLUSTRATIONS

II. TABLES

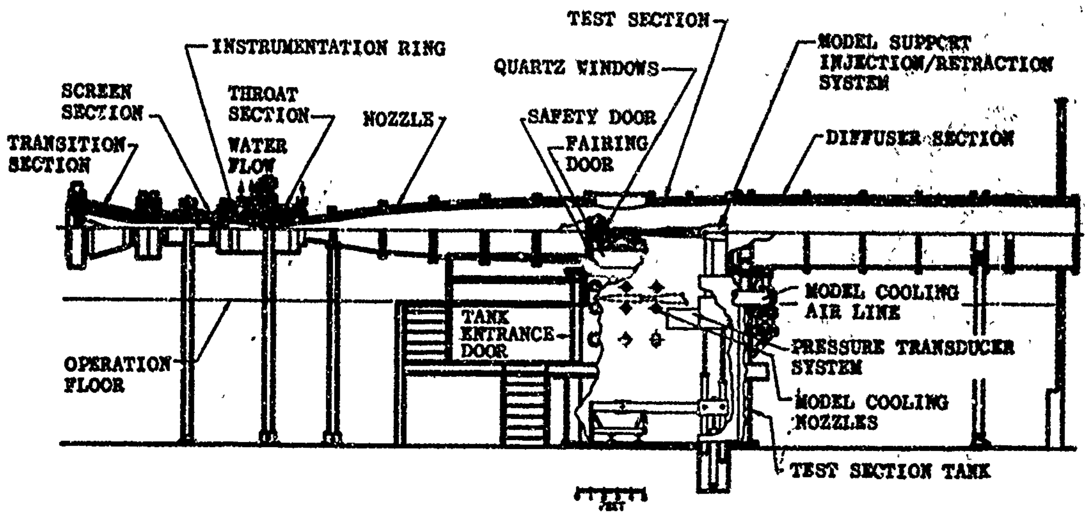

a. Tunnel C

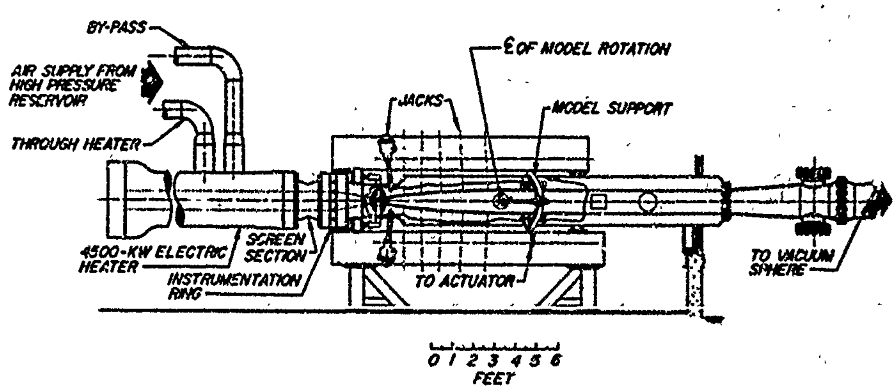

b. Tunnel E

Fig. 1 AEDC-VKF Wind Tunnels

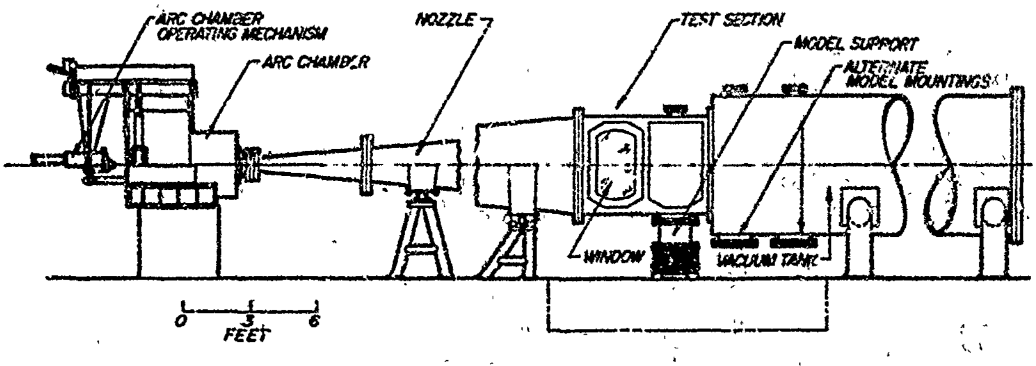

c. Tunnel H

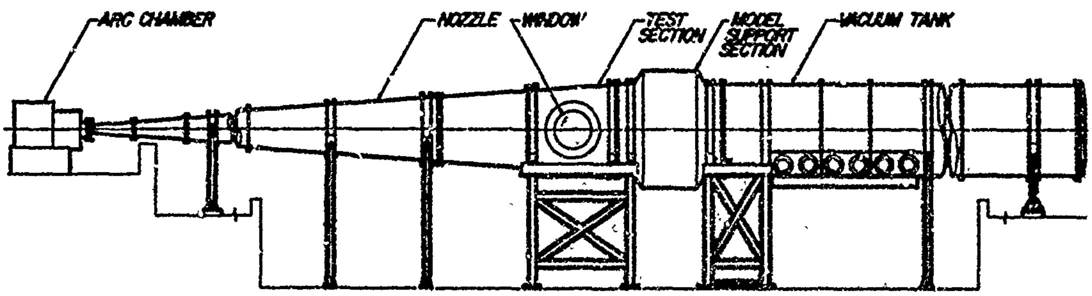

d. Tunnel F
Fig. 1 Concluded

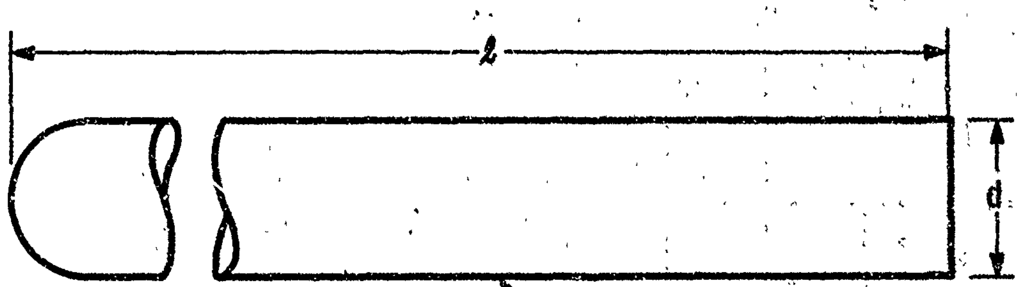

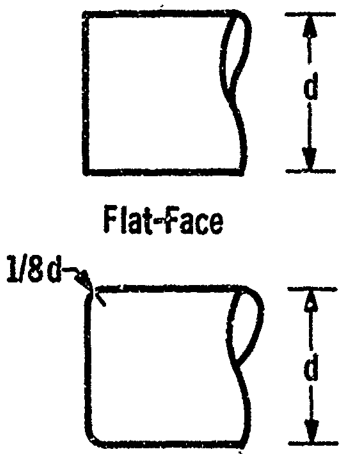

Hemisphere

d, in.	ℓ, in.	VKF Tunnel
5.8	39.15	B and C
4.0	6.0	H
1.0	13.5	H
4.0	29.0	F

Flat-Face

d, in.	ℓ, in.	VKF Tunnel
5.8	35.05	B and C
2.9	2.0	E
6.0	6.0	H
1.0	13.5	H

Rounded-Shoulder Flat-Face

d, in.	ℓ, in.	VKF Tunnel
5.8	34.80	B and C
6.0	6.0	H

Fig. 2 Model Description

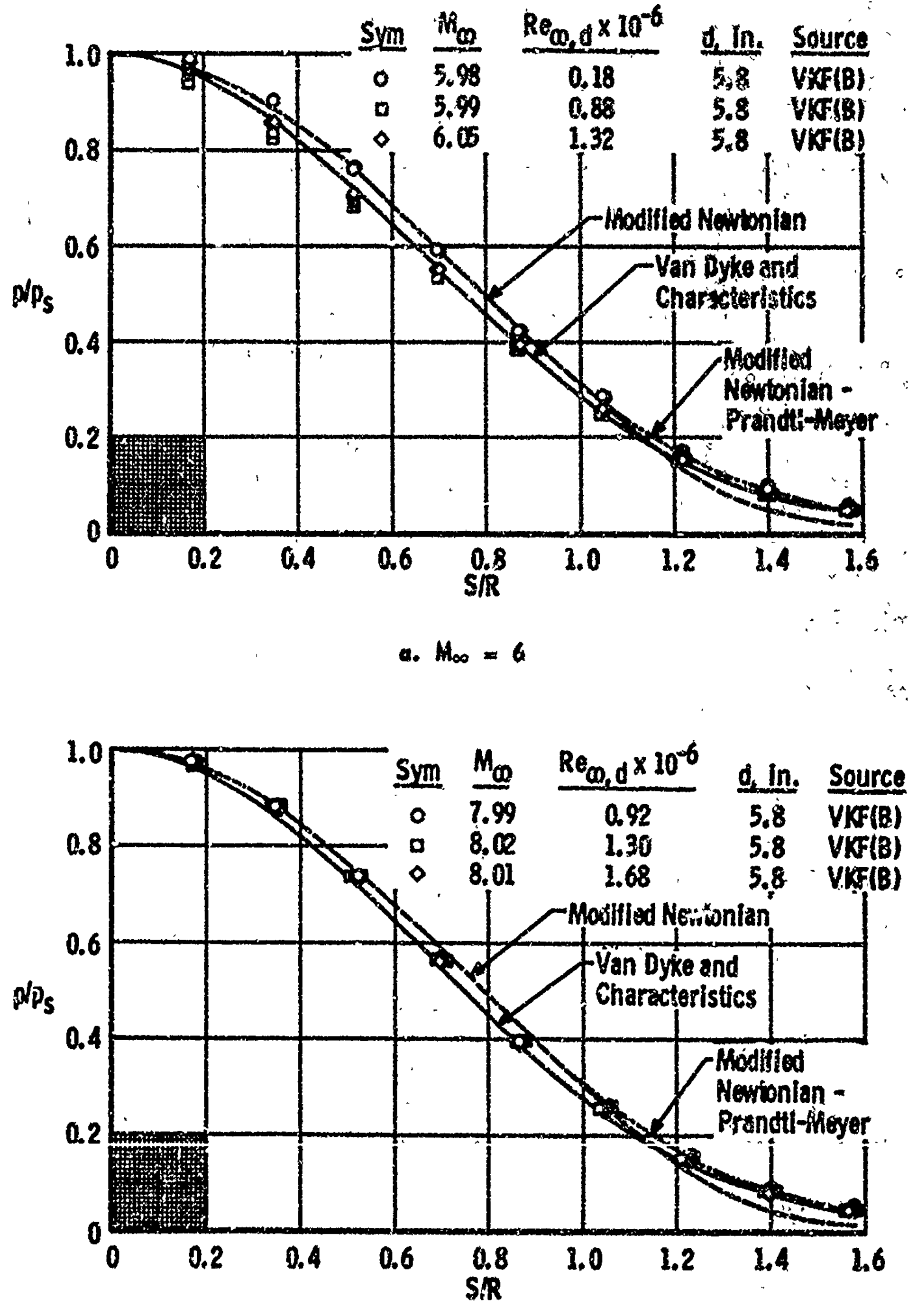

Fig. 3 Experimental and Theoretical Pressure Distributions on a Hemisphere Model

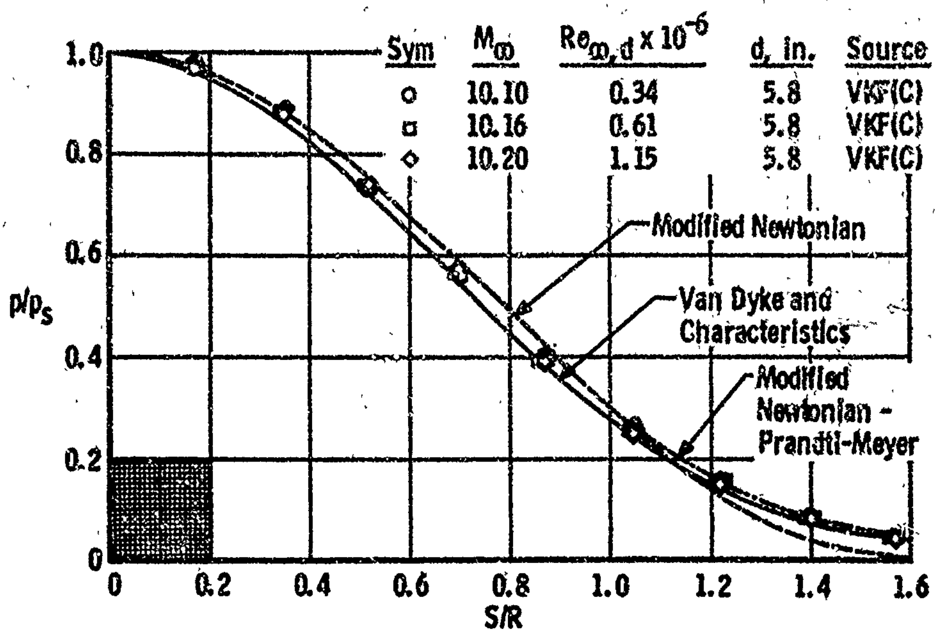

c. $M_\infty = 10$

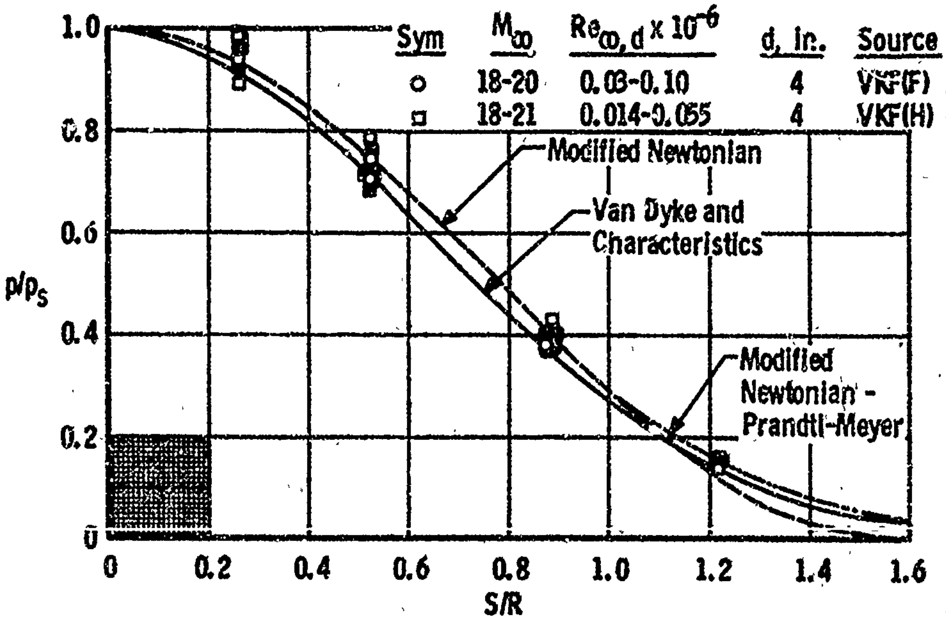

d. $M_\infty = 19$

Fig. 3 Concluded

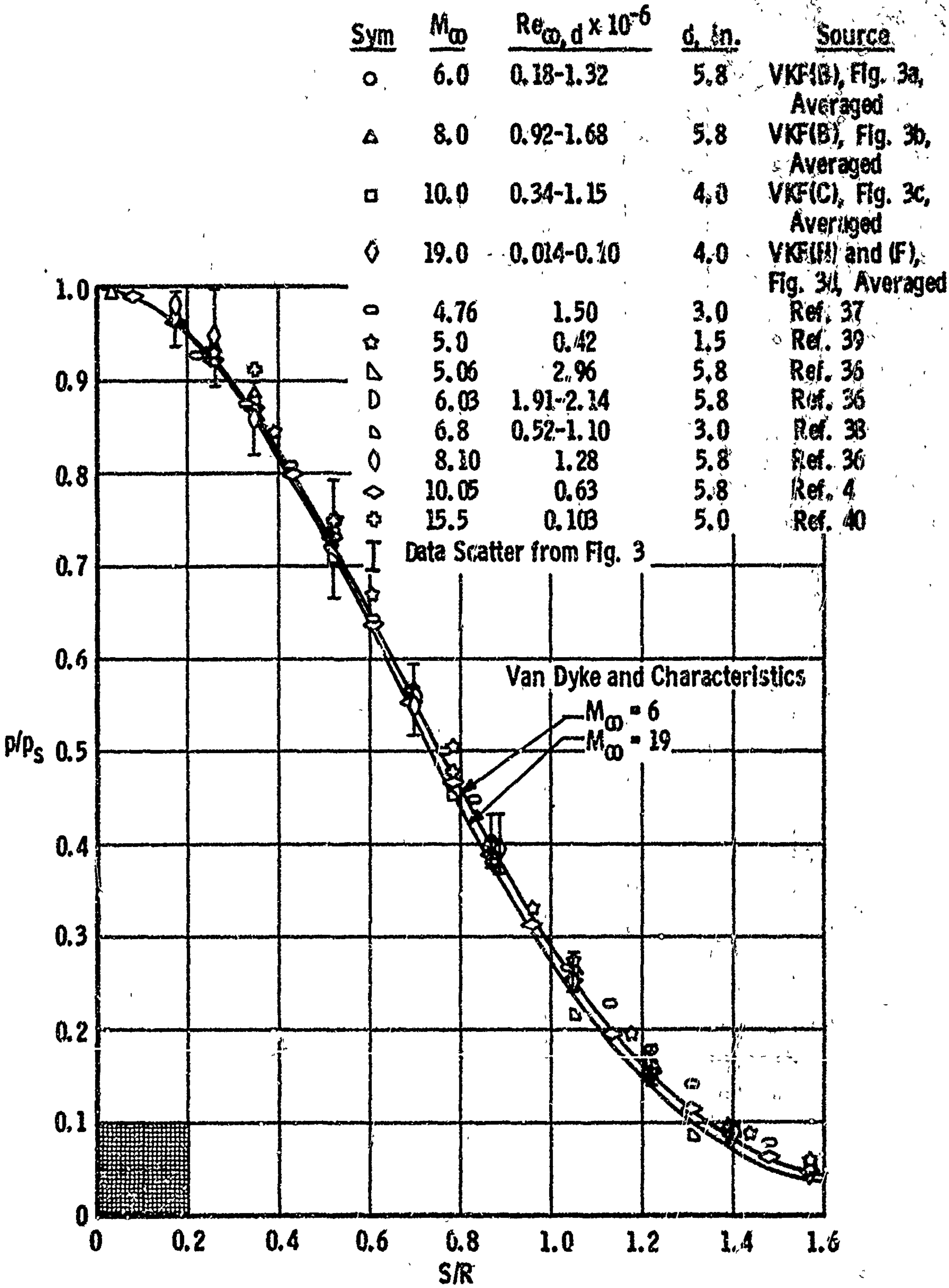

Fig. 4 Hemisphere Model Pressure Data Summary

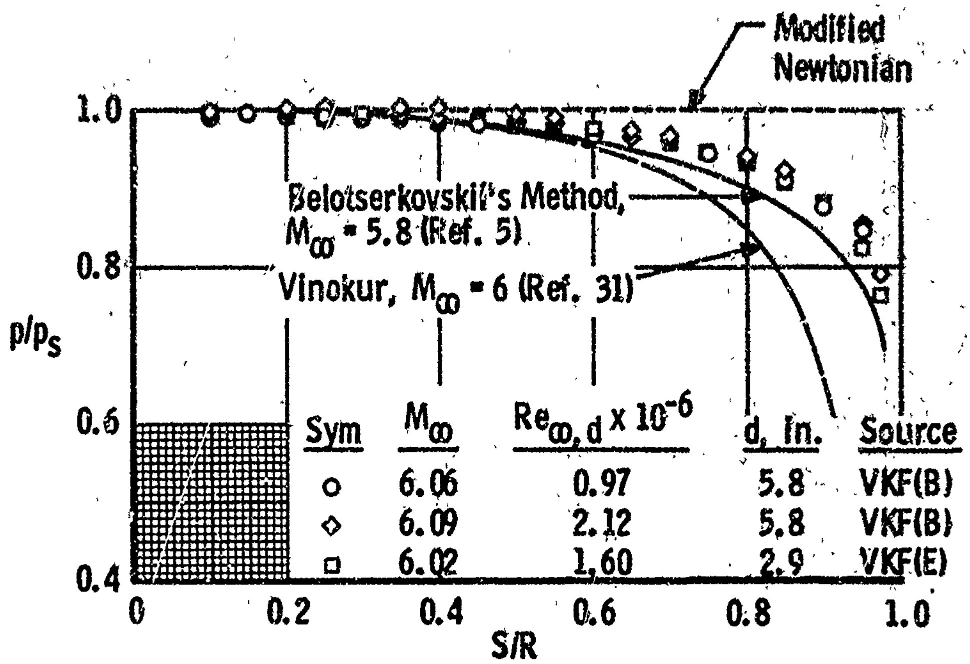

a. M_∞ = 6

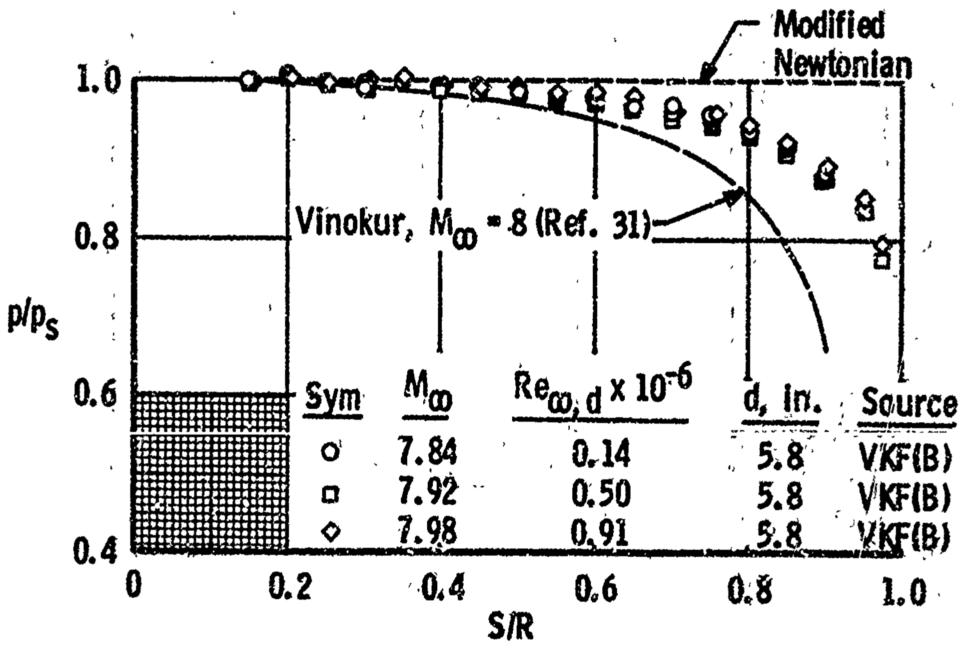

b. M_∞ = 8

Fig. 5 Experimental and Theoretical Pressure Distributions on a Flat-Face Model

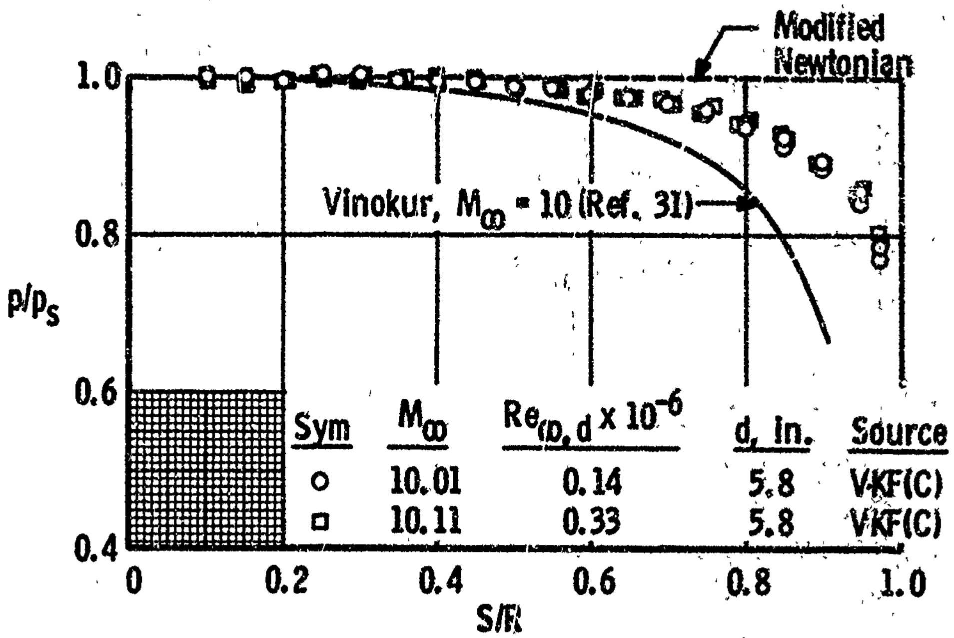

c. M_∞ = 10

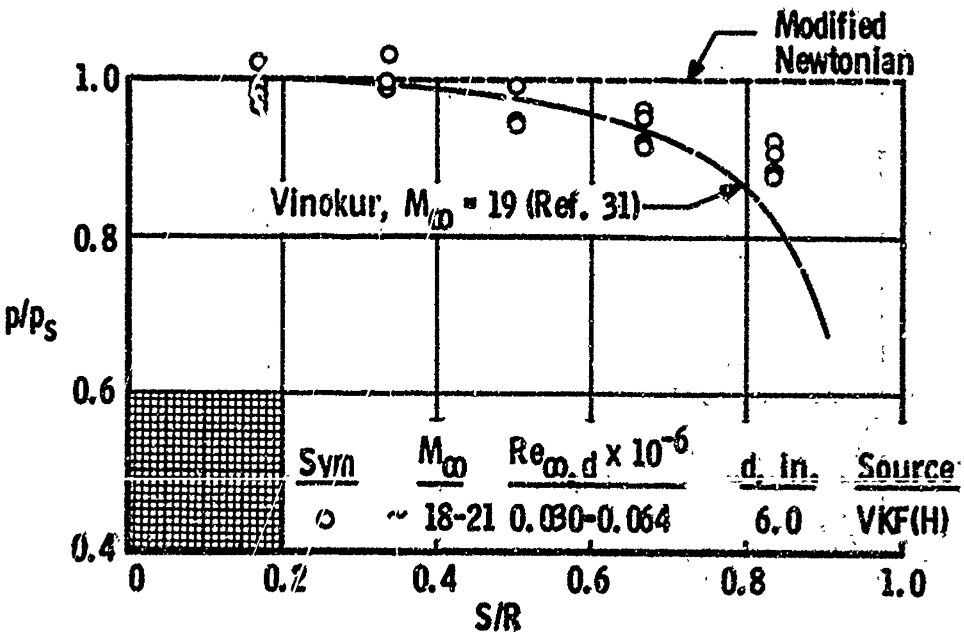

d. M_∞ = 19

Fig. 5 Concluded

Sym	M_∞	$Re_{\infty,d} \times 10^{-6}$	d, in.	Source
○	6.0	0.97-3.40	5.8, 2.9	VKF(B&E), Fig. 5a, Averaged
△	8.0	0.14-0.91	5.8	VKF(B), Fig. 5b, Averaged
□	10.0	0.14-0.33	5.8	VKF(C), Fig. 5c, Averaged
◇	19.0	0.030-0.064	6.0	VKF(H), Fig. 5d, Averaged
◊	4.76	1.25	2.5	Ref. 37
⬭	4.76	1.03	3.0	Ref. 43
◺	4.84	0.19-0.93	3.0	Ref. 42
D	5.3	0.19-0.93	3.0	Ref. 42
0	7.9	0.19-0.93	3.0	Ref. 42
I	Data Scatter from Fig. 5			

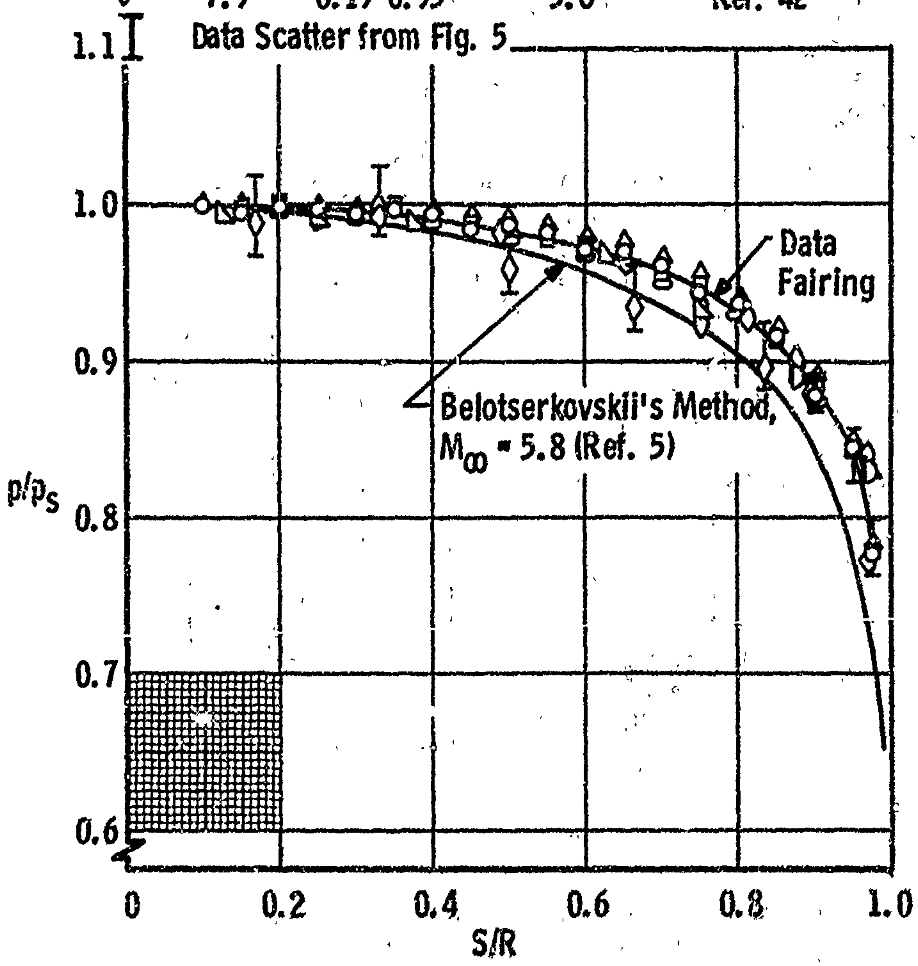

Fig. 6 Flat-Face Model Pressure Data Summary

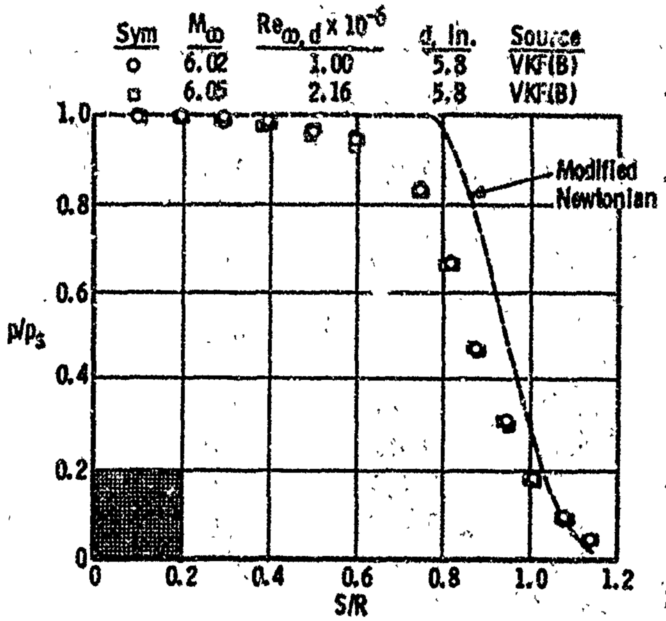

a. $M_\infty = 6$

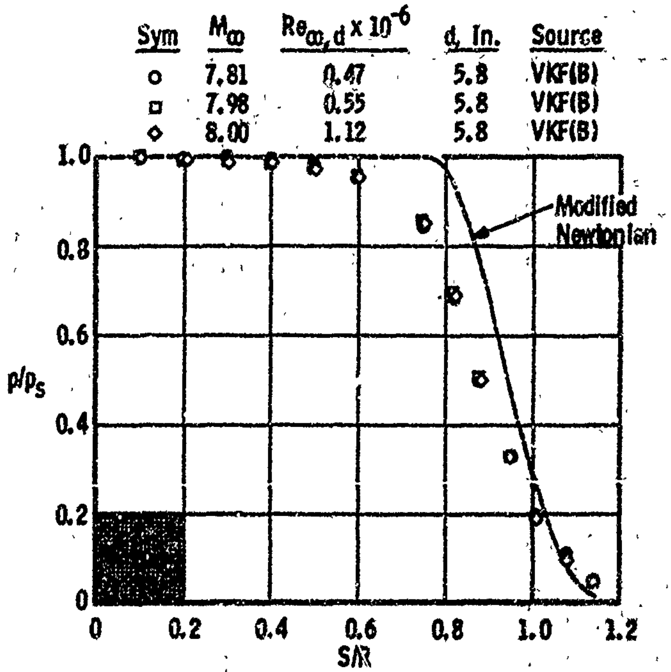

b. $M_\infty = 8$

Fig. 7 Experimental and Theoretical Pressure Distributions on a Rounded-Shoulder Flat-Face Model

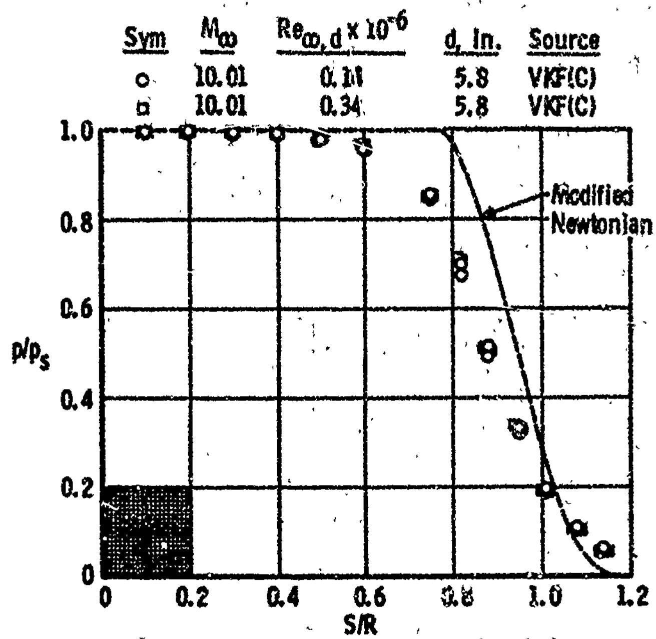

c. M_∞ = 10

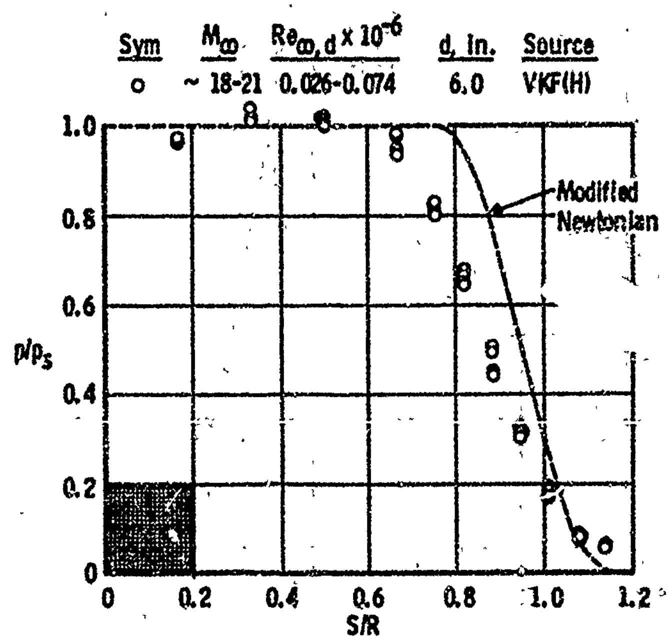

d. M_∞ = 19

Fig. 7 Concluded

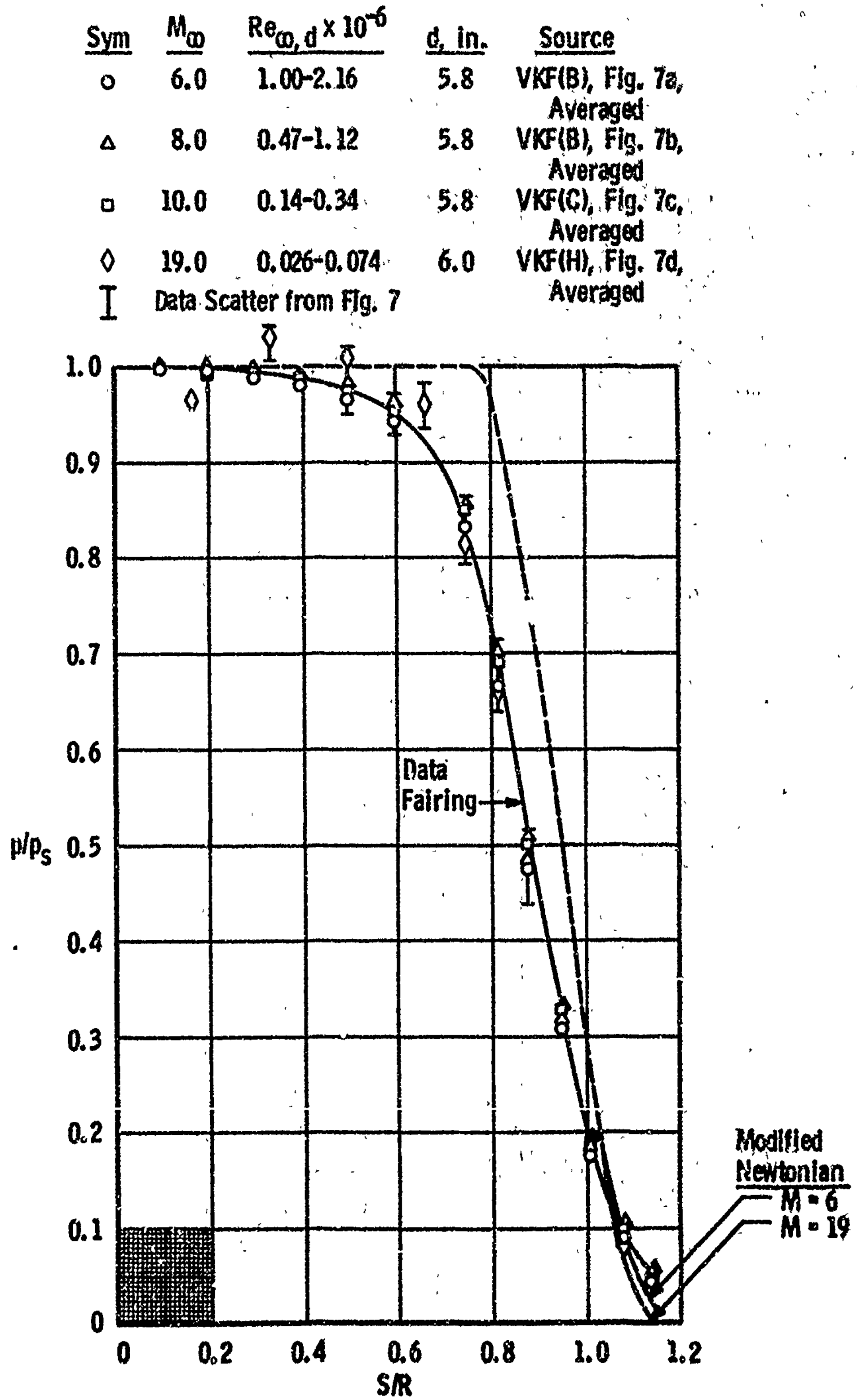

Fig. 8 Rounded-Shoulder Flat-Face Model Pressure Data Summary

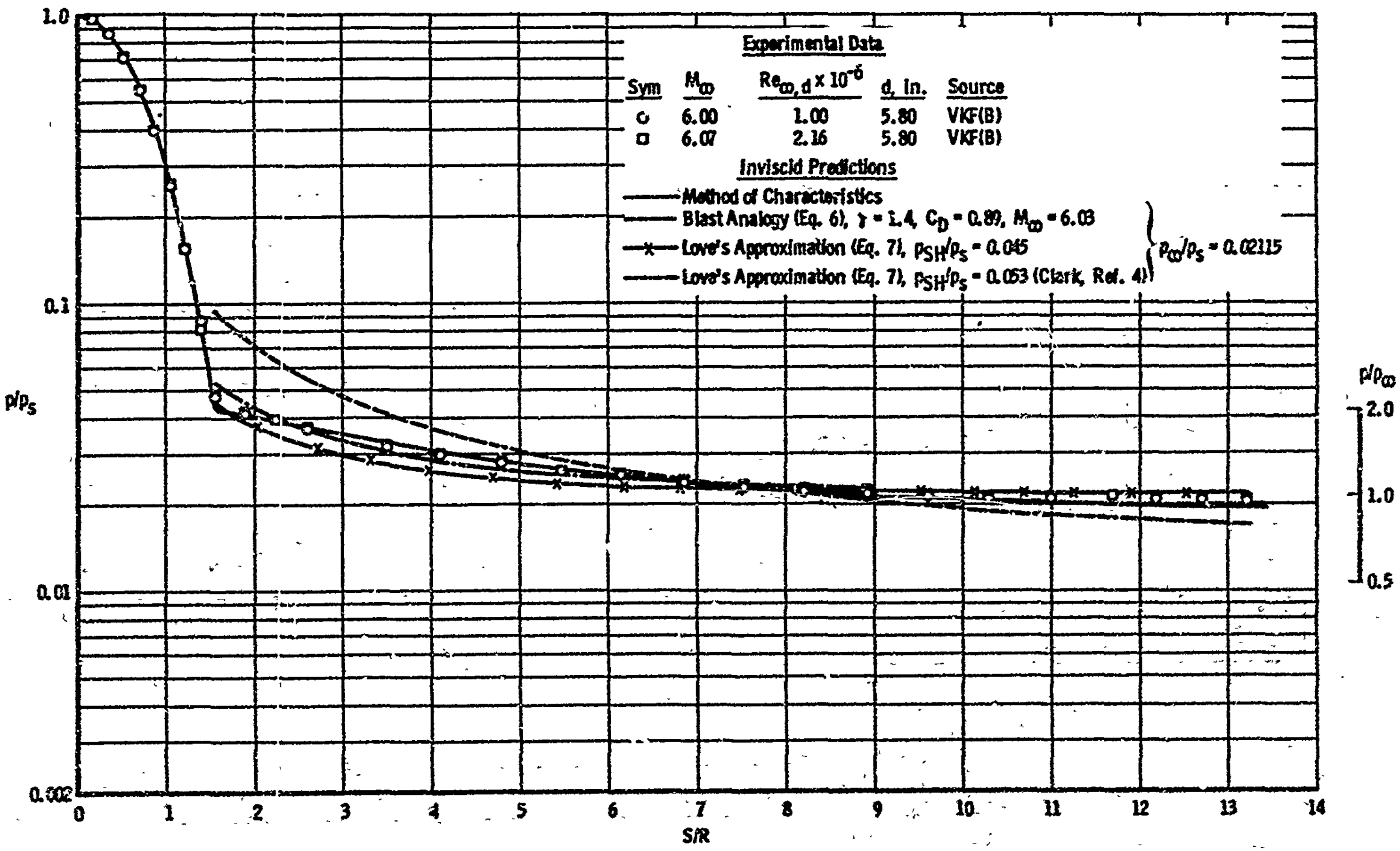

a. $M_\infty = 6$

Fig. 9 Experimental and Theoretical Pressure Distributions on a Hemisphere Cylinder Model

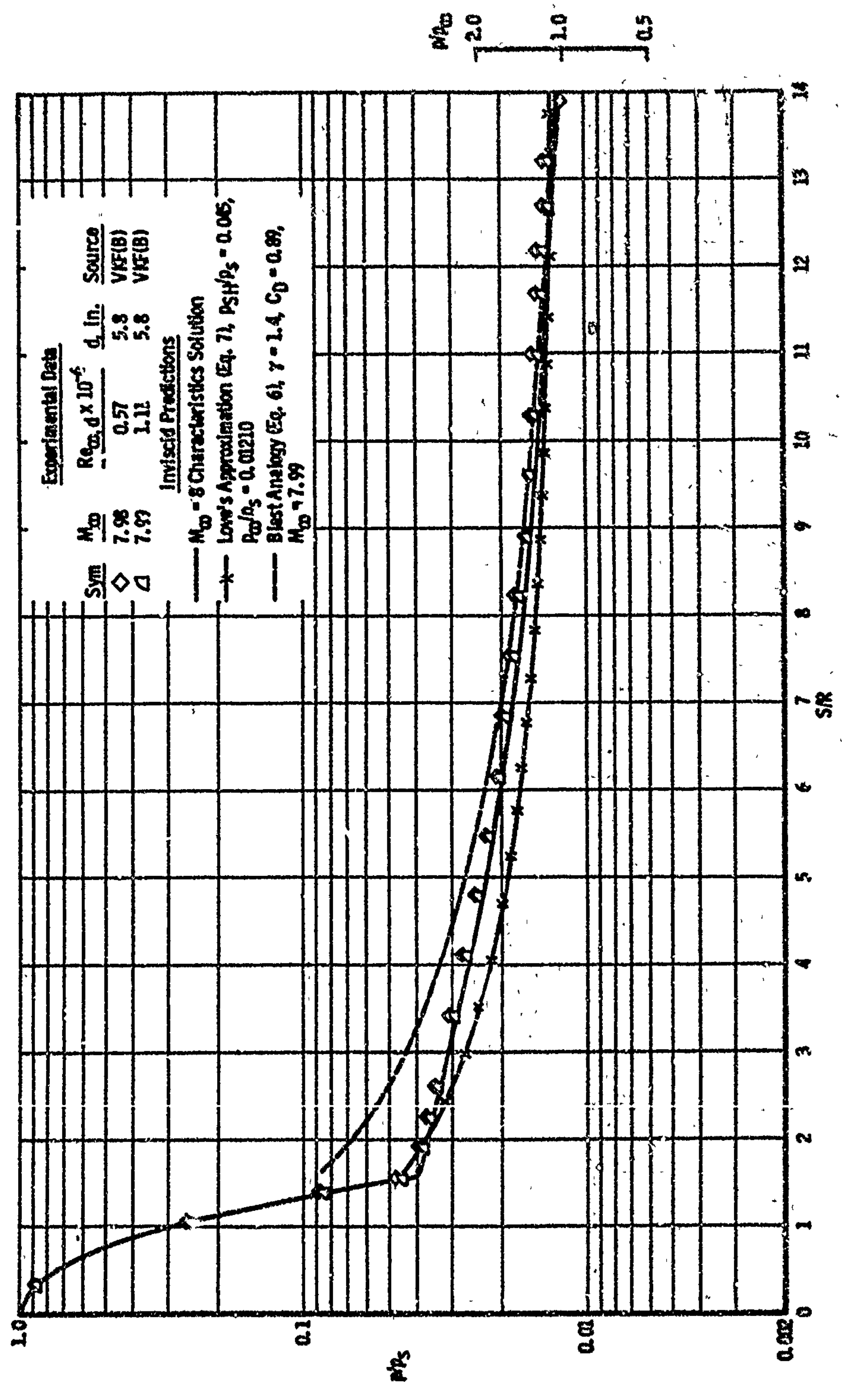

b. M_∞ = 8

Fig. 9 Continued

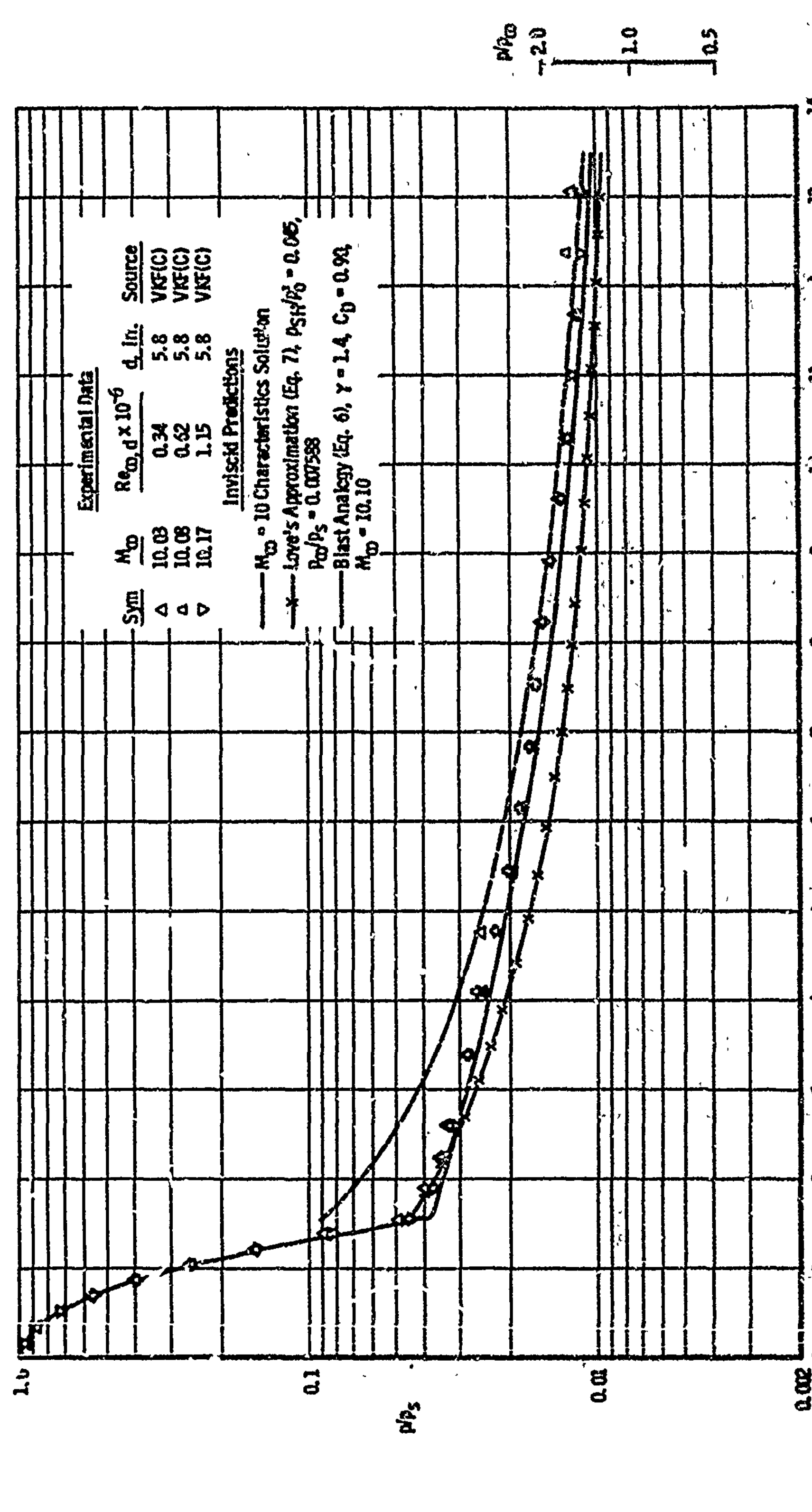

c. M_∞ = 10

Fig. 9 Continued

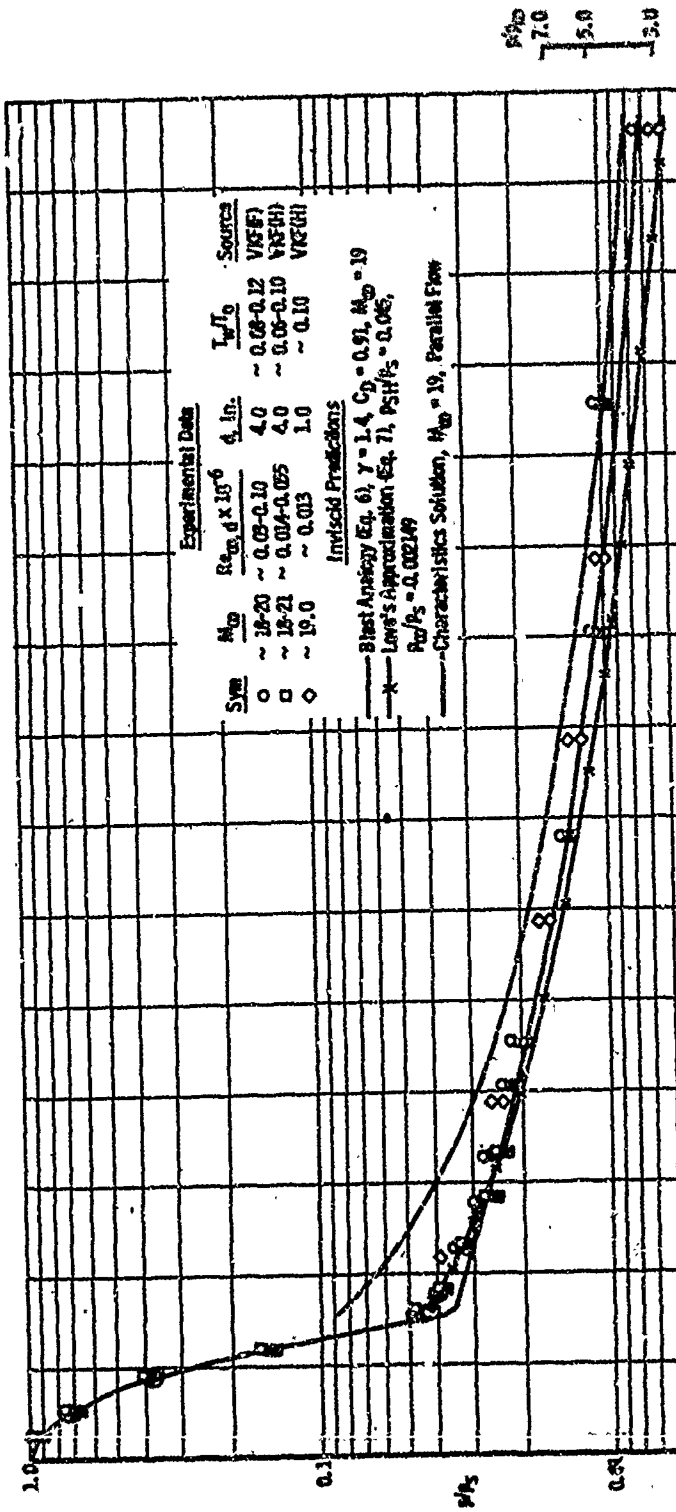

d. M_∞ = 19 (Comparison with Inviscid Theories)

Fig. 9 Continued

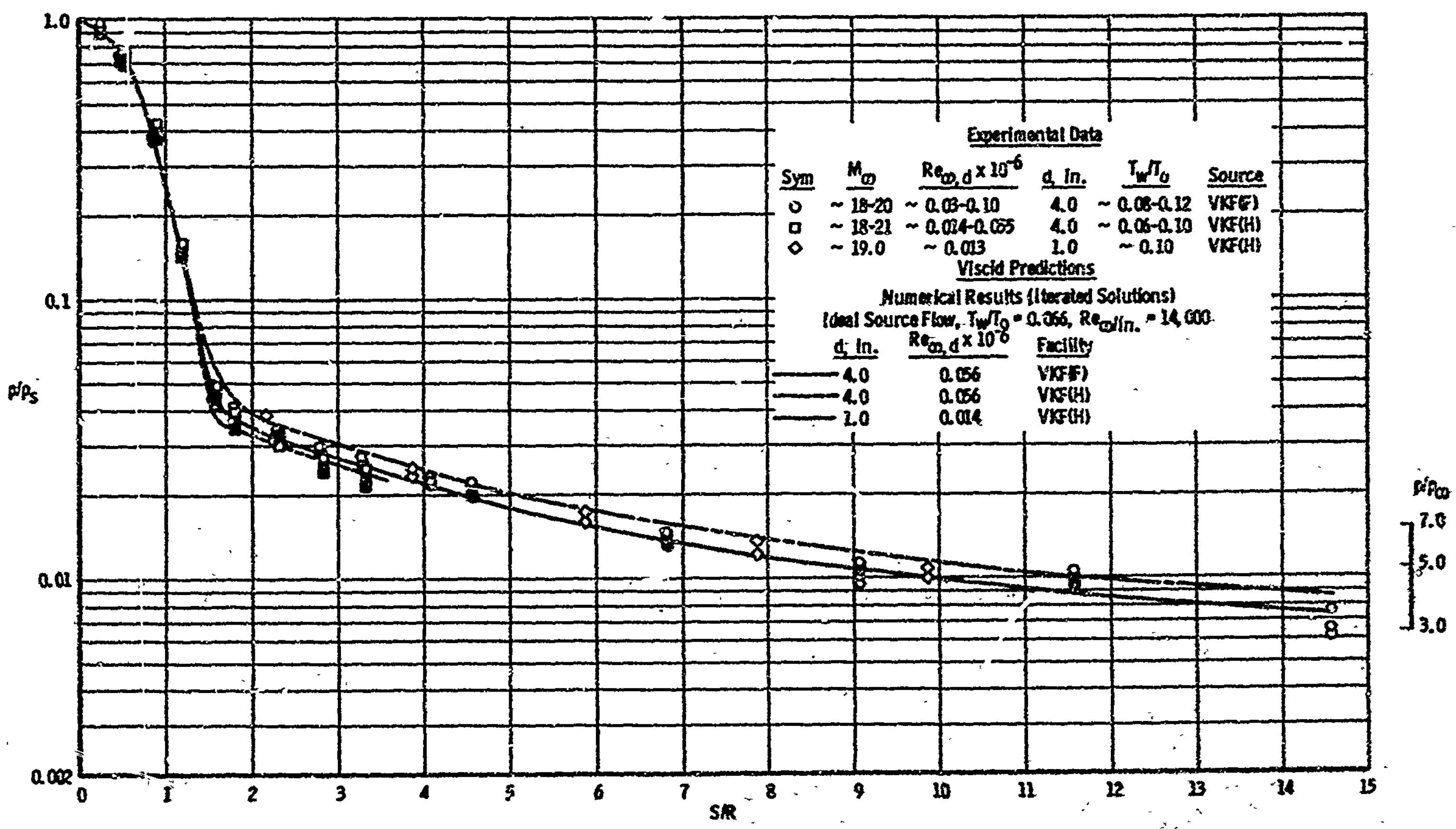

e. $M_\infty = 19$ (Comparison with Viscid Theories)

Fig. 9 Concluded

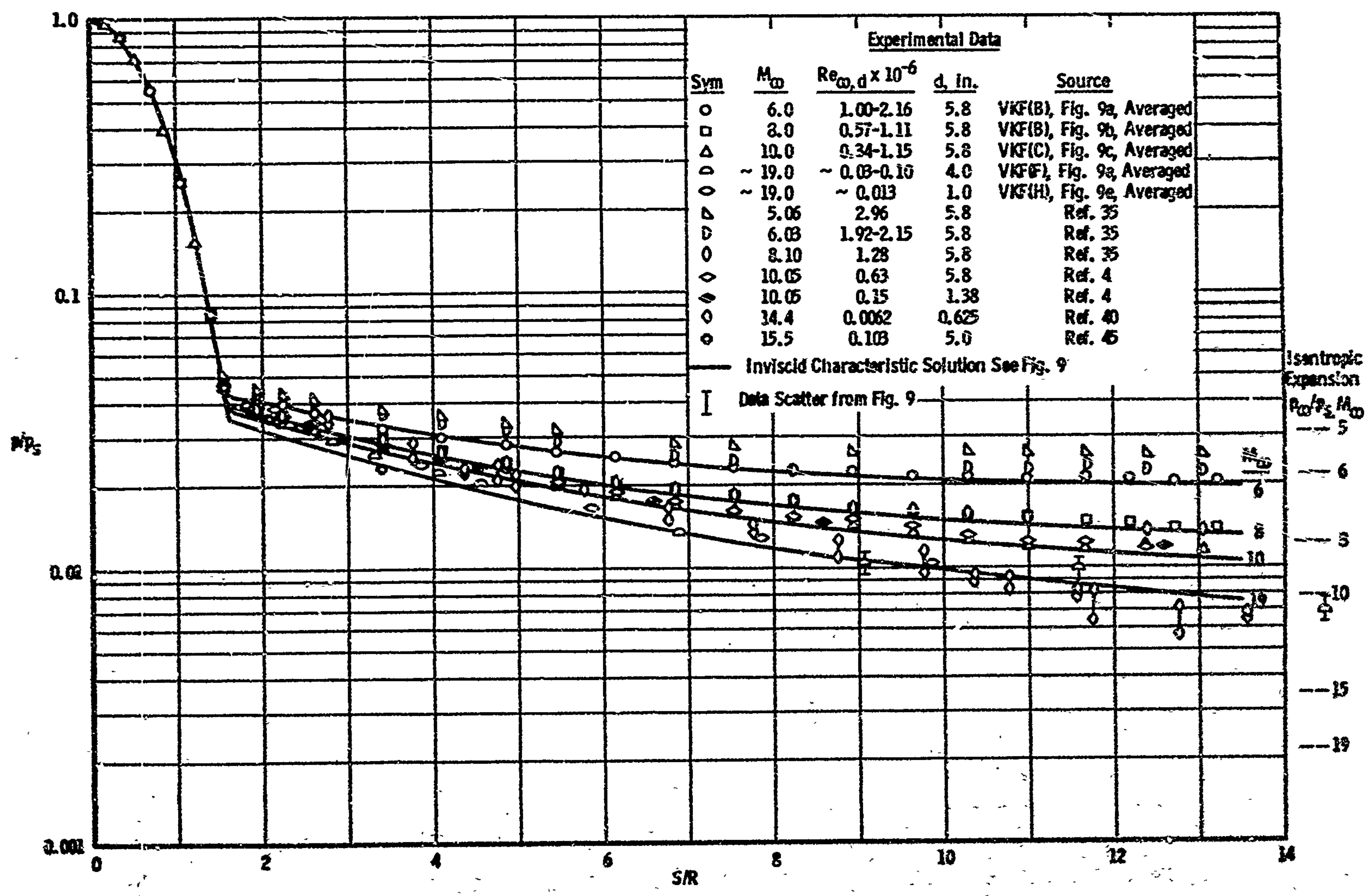

Fig. 10 Hemisphere Cylinder Model Pressure Data Summary

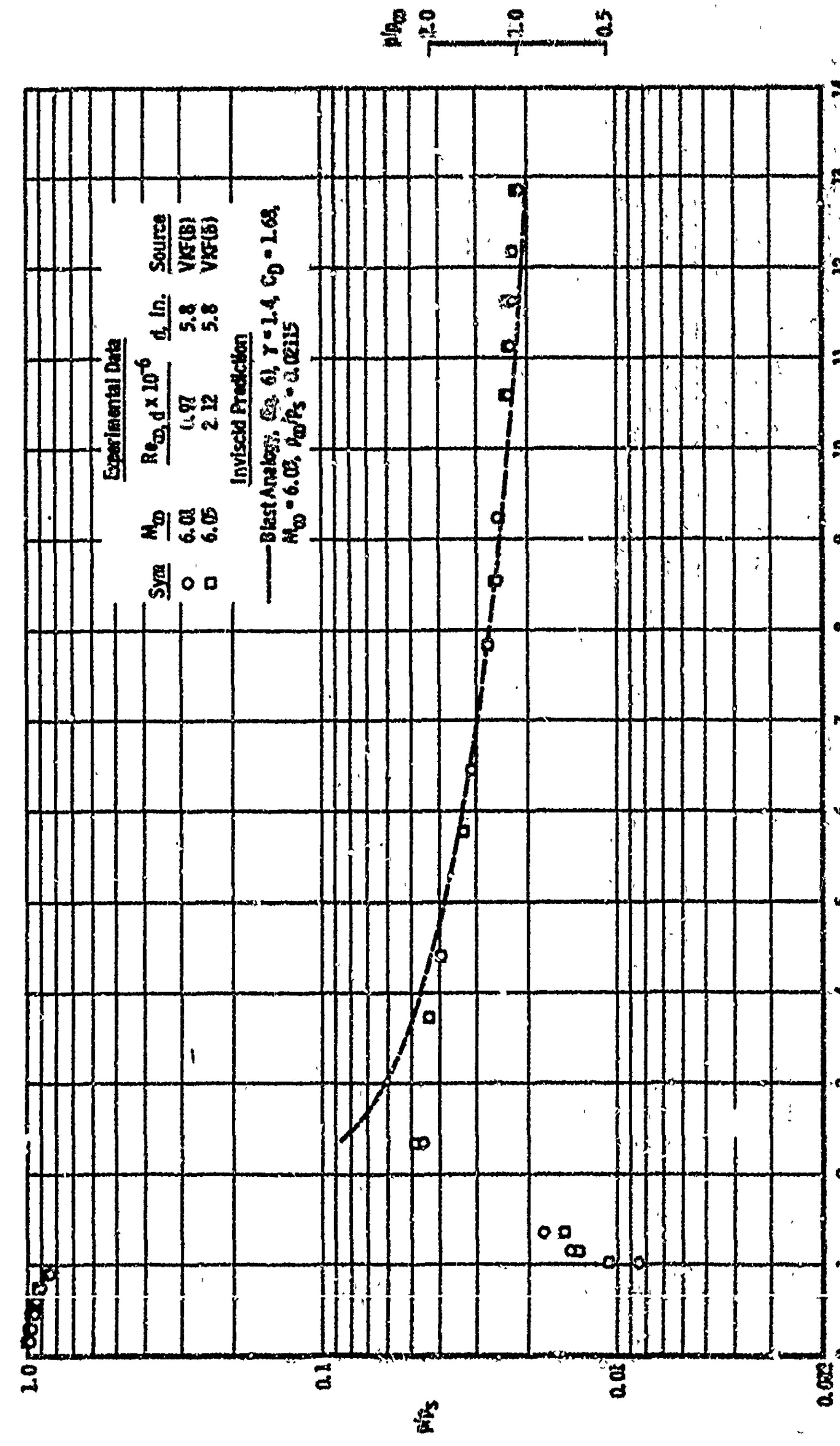

a. $M_\infty = 6$

Fig. 11 Experimental and Theoretical Pressure Distributions on a Flat-Face Cylinder Model

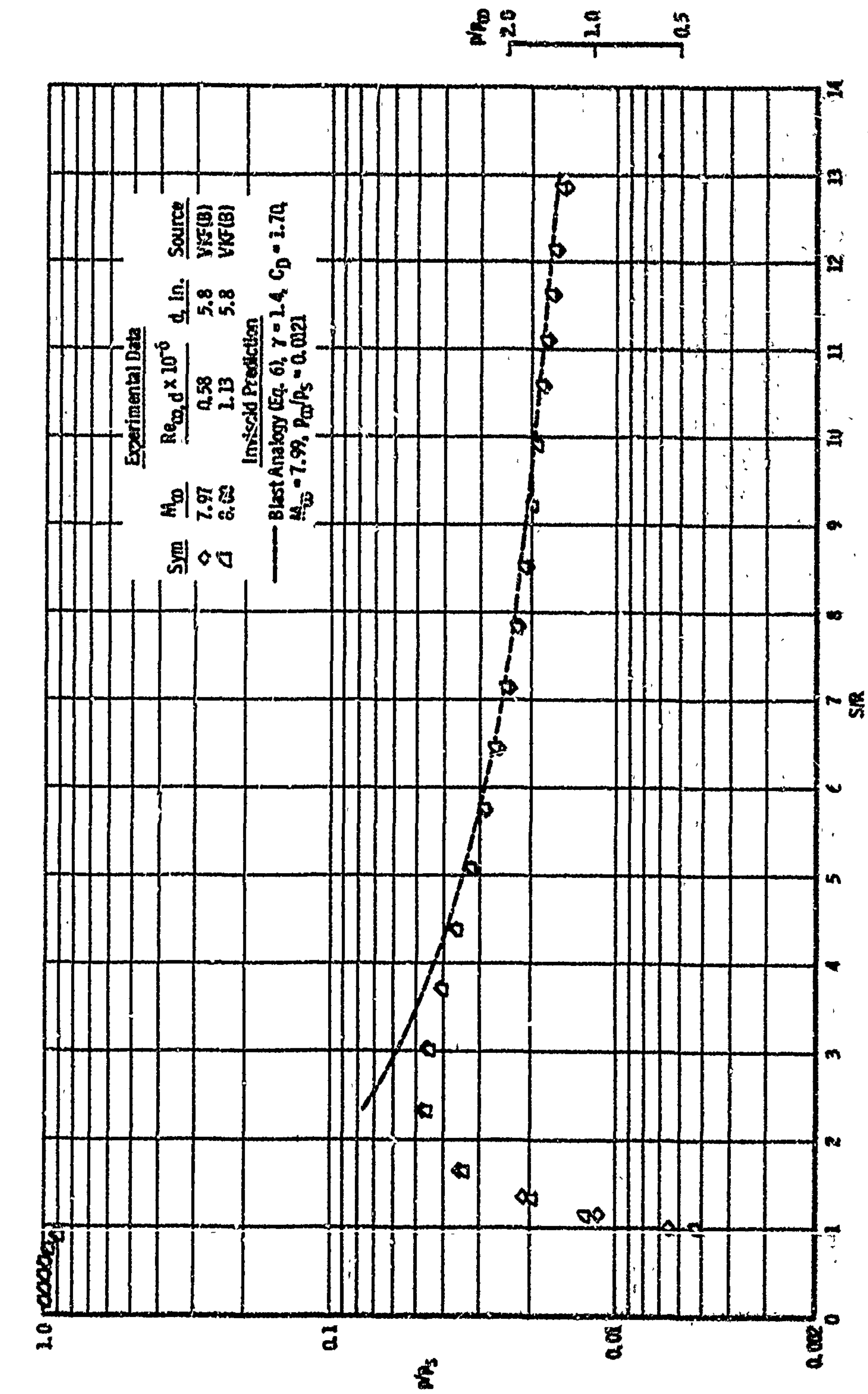

b. M_∞ = 8

Fig. 11 Continued

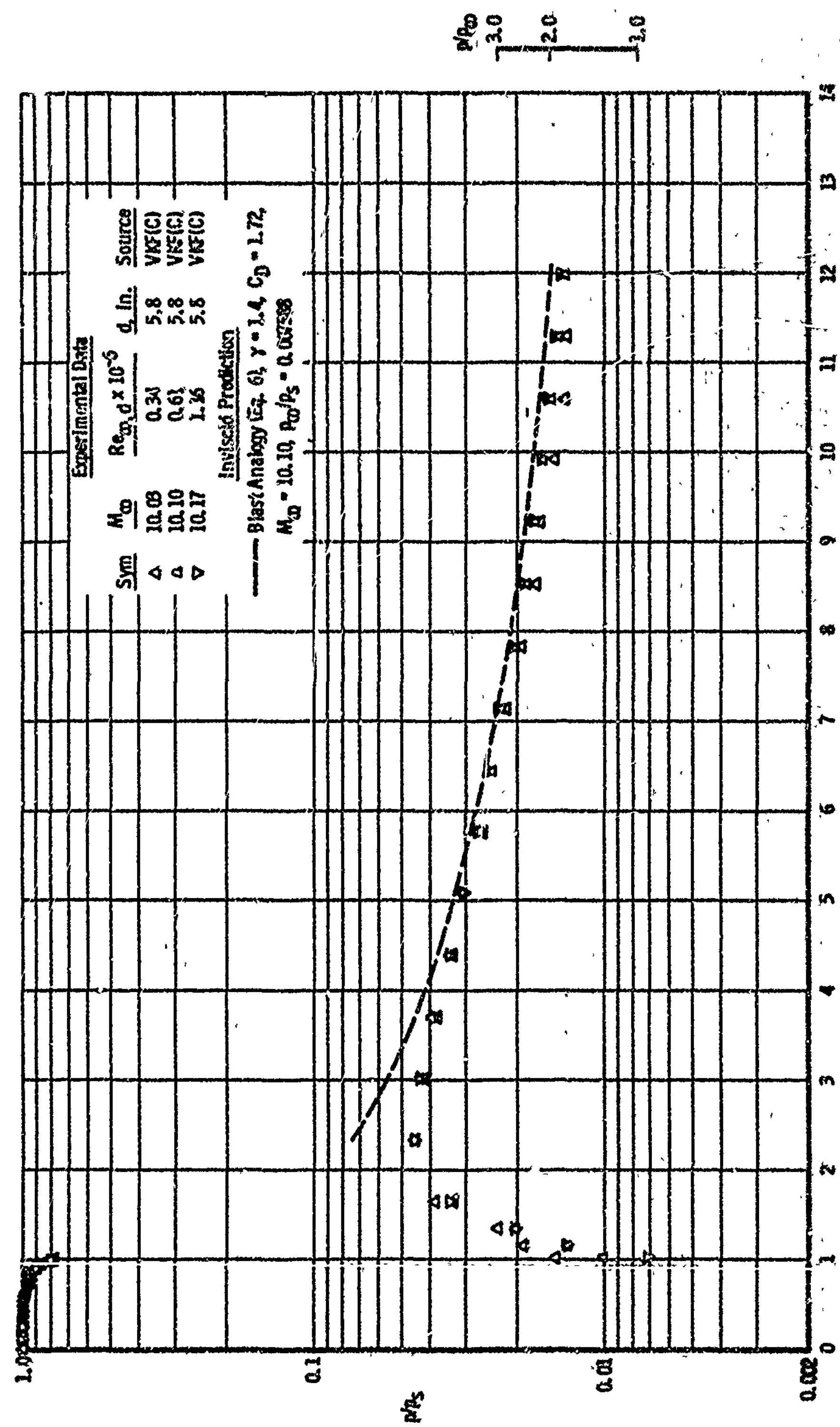

c. M_∞ = 10
Fig. 11 Continued

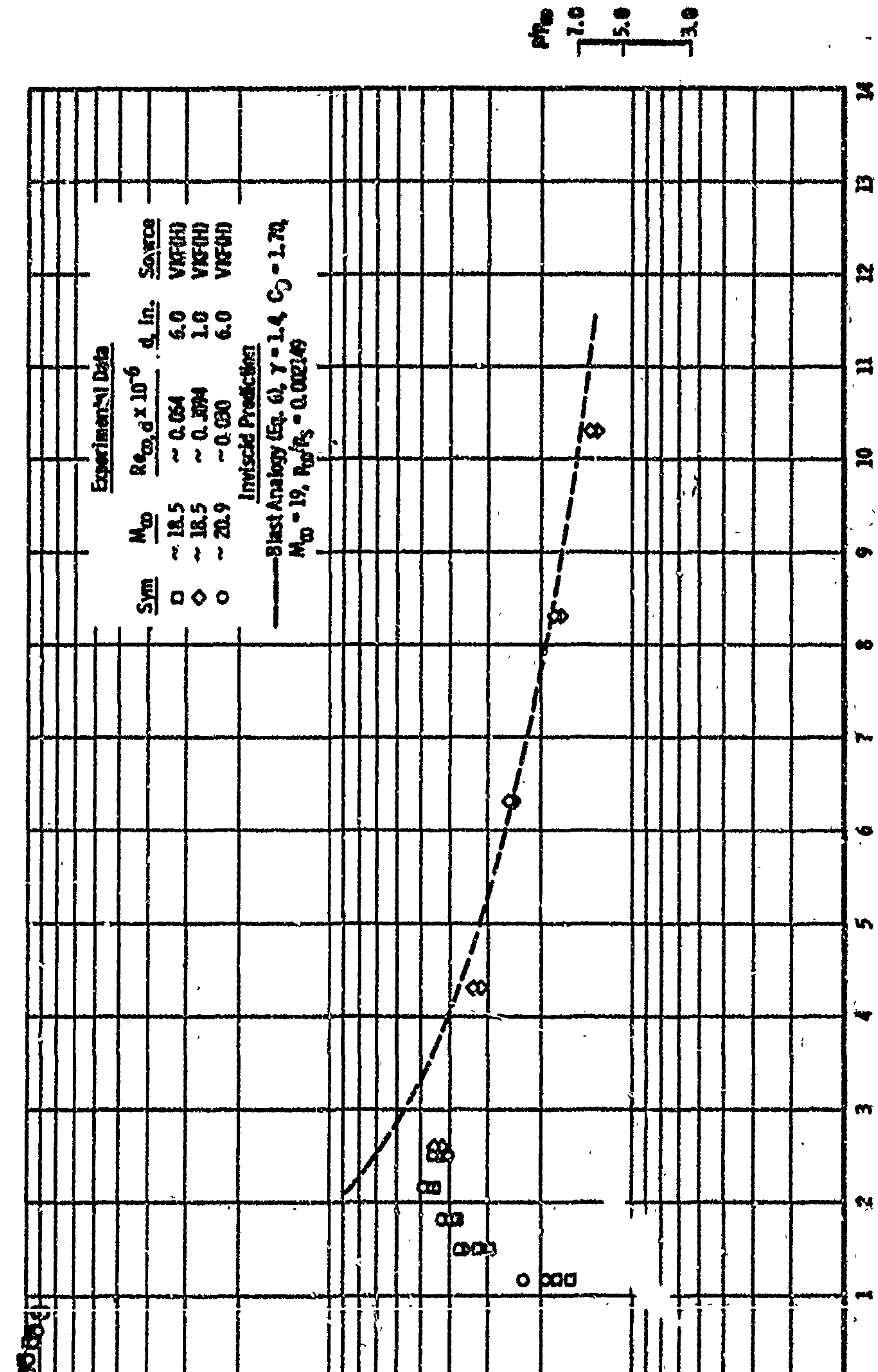

d. $M_\infty = 19$
Fig. 11 Concluded

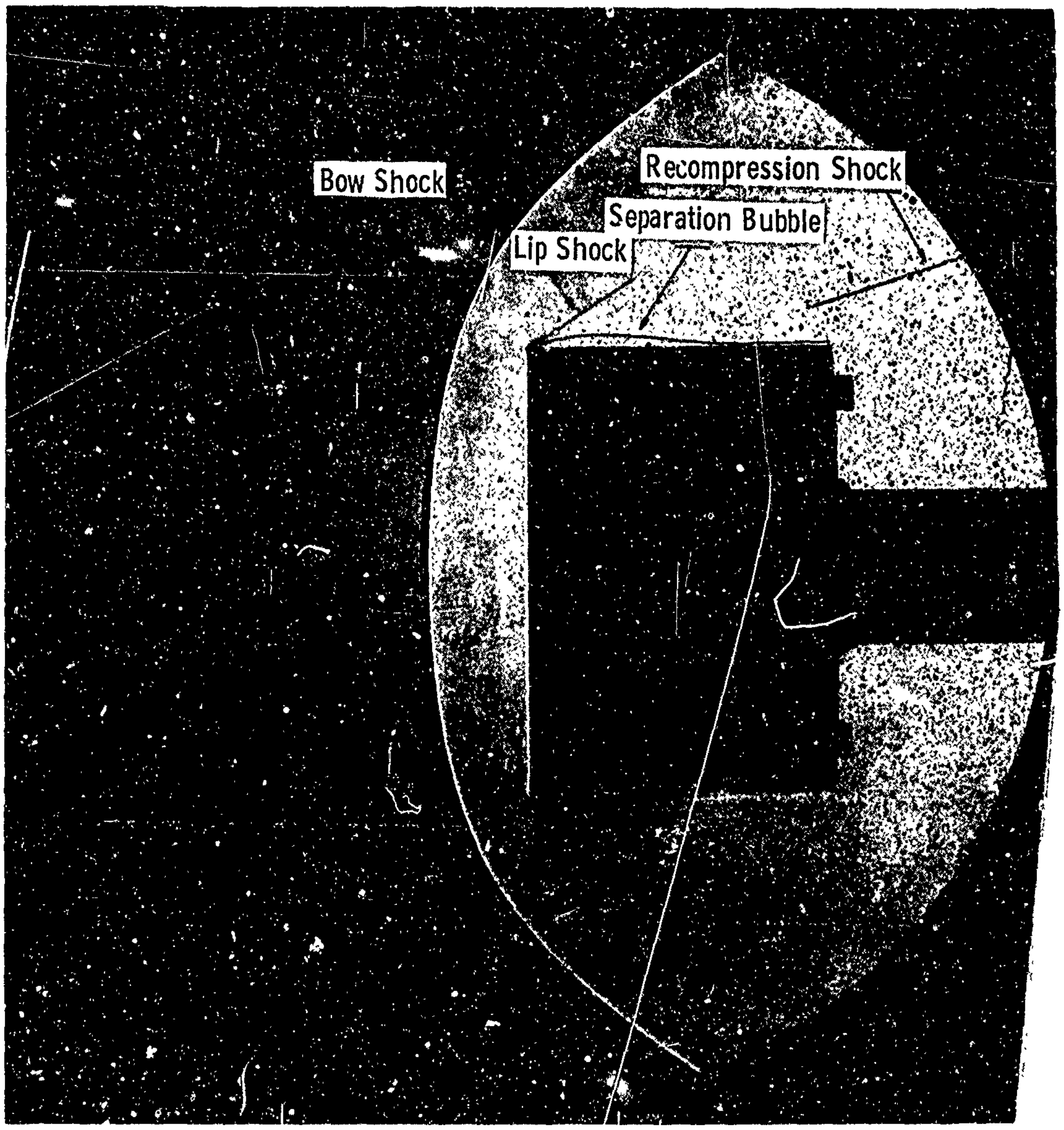

Fig. 12 Shadowgraph of Flat-Face Model at $M_\infty = 6$, $Re_{\infty_d} = 1.68 \times 10^6$, Tunnel E

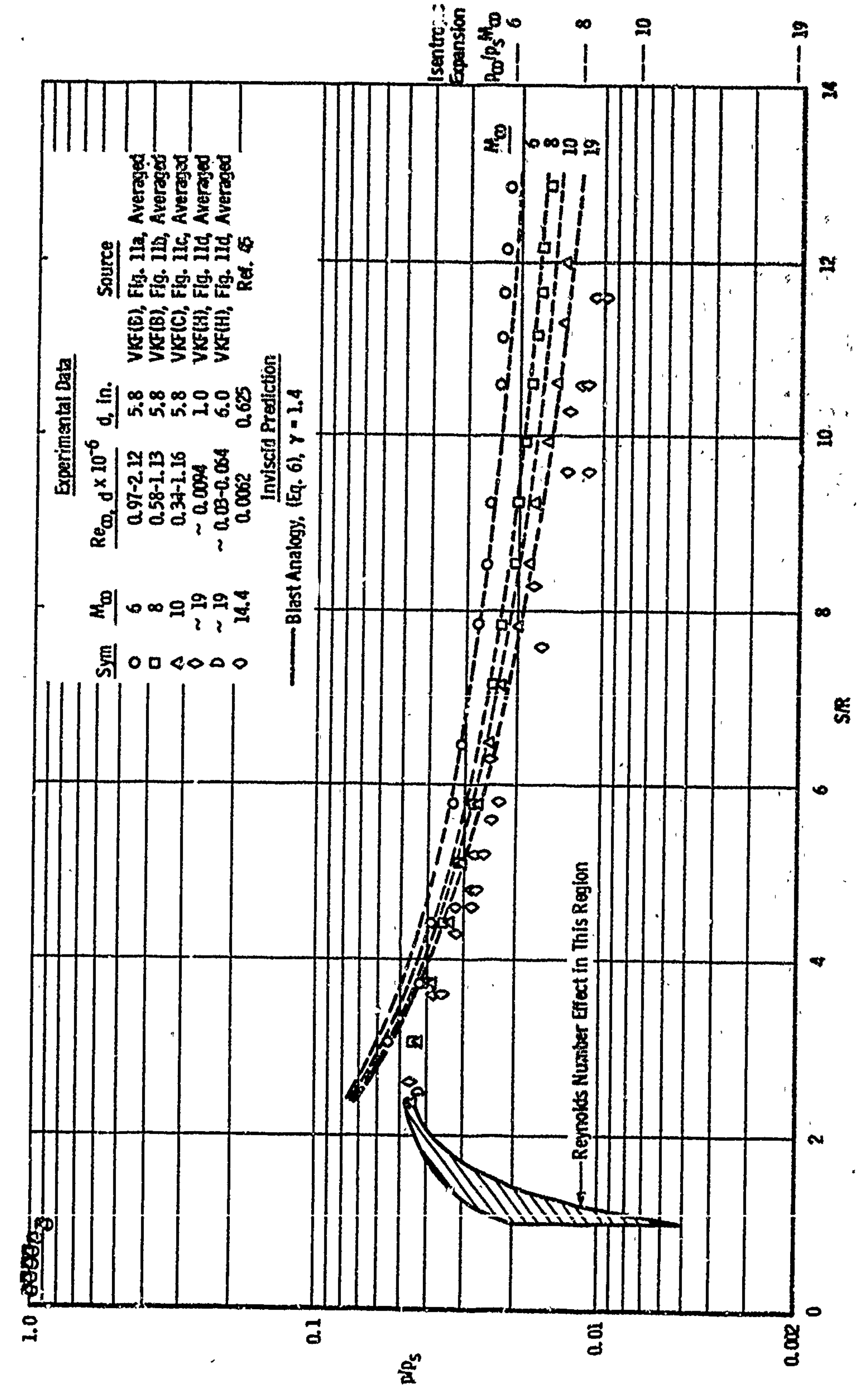

Fig. 13 Flat-Face Cylinder Model Pressure Data Summary

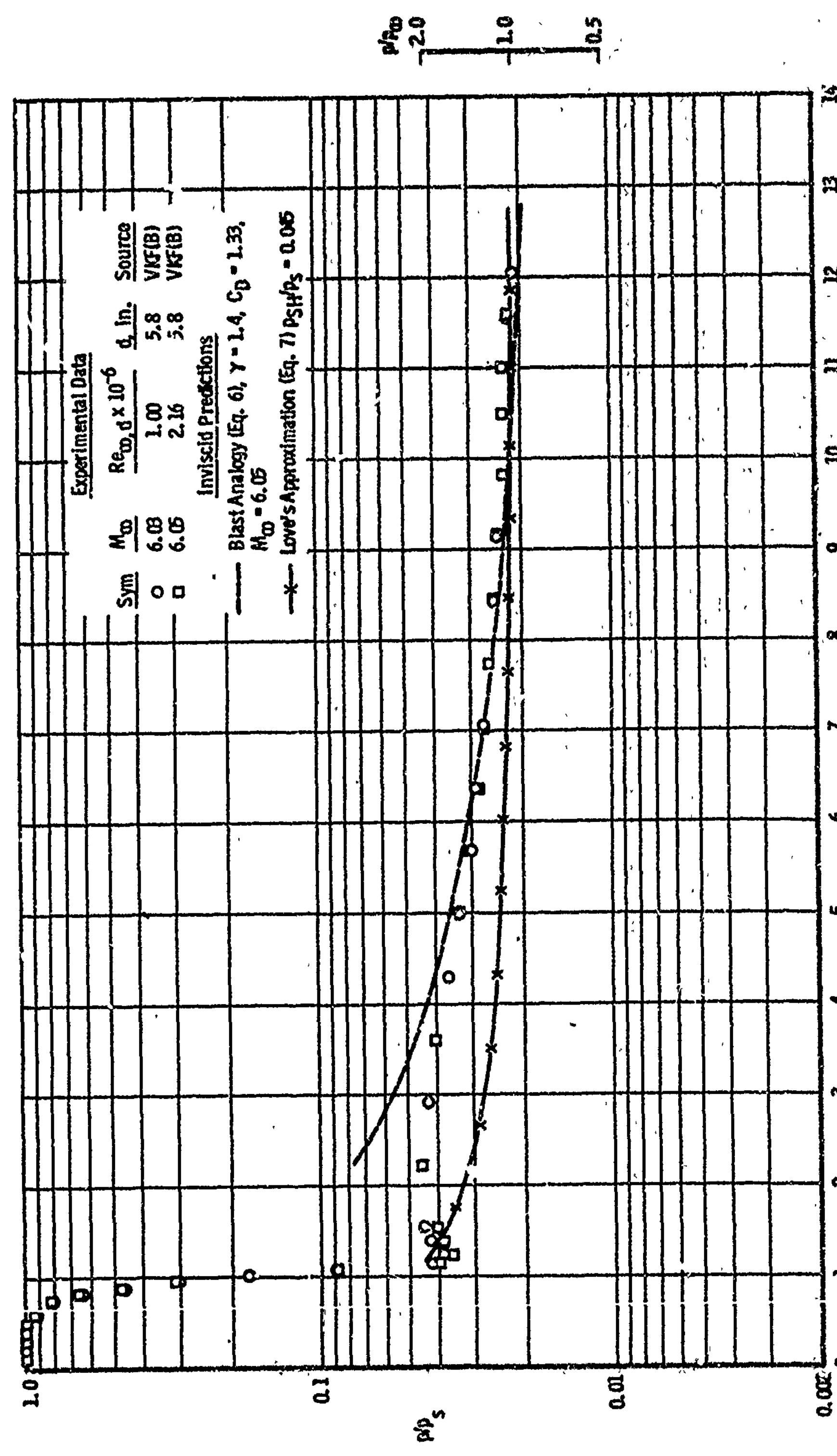

a. M_∞ = 6

Fig. 14 Experimental and Theoretical Pressure Distributions on a Rounded-Shoulder Flat-Face Cylinder Model

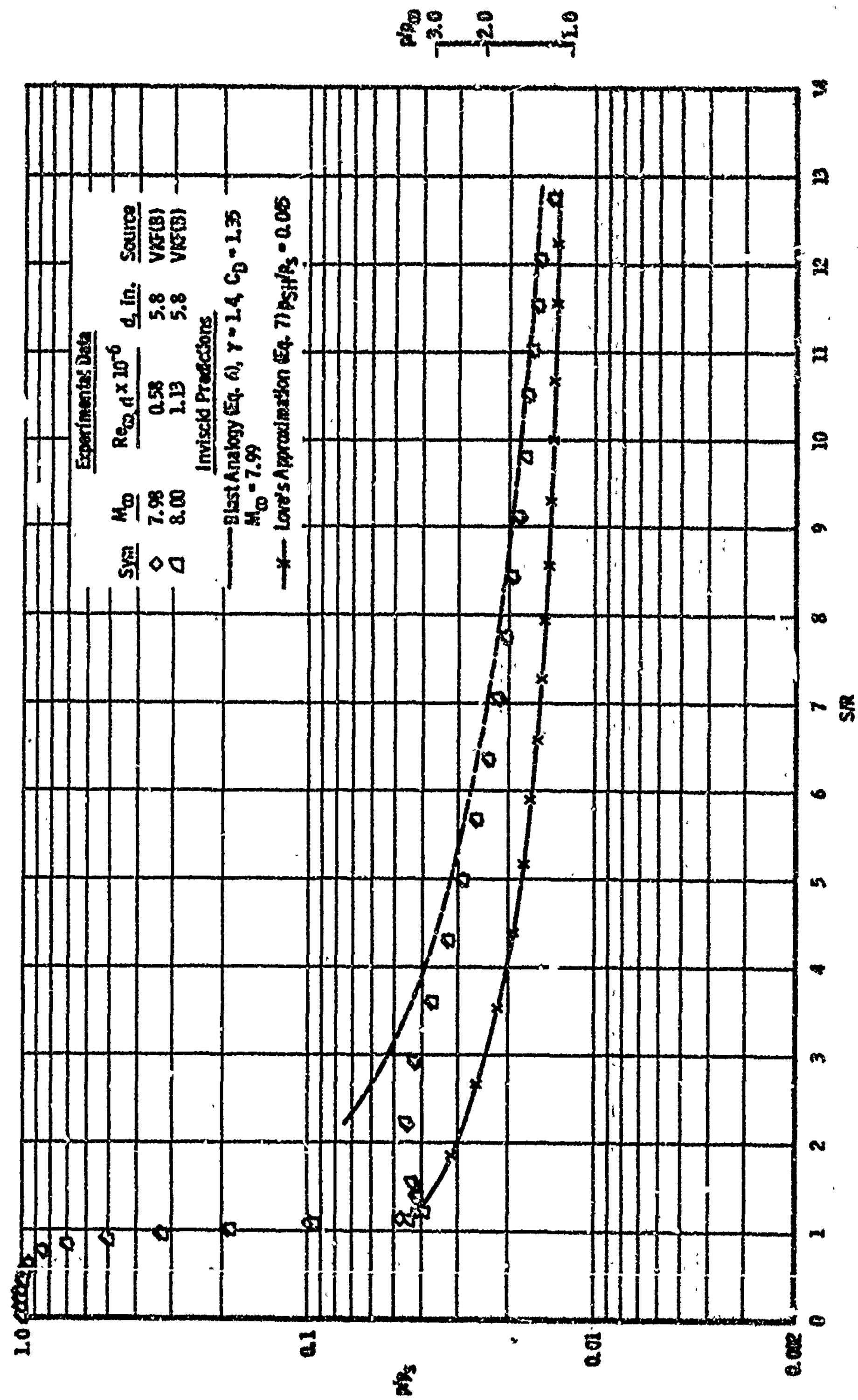

b. $M_\infty = 8$
Fig. 14 Continued

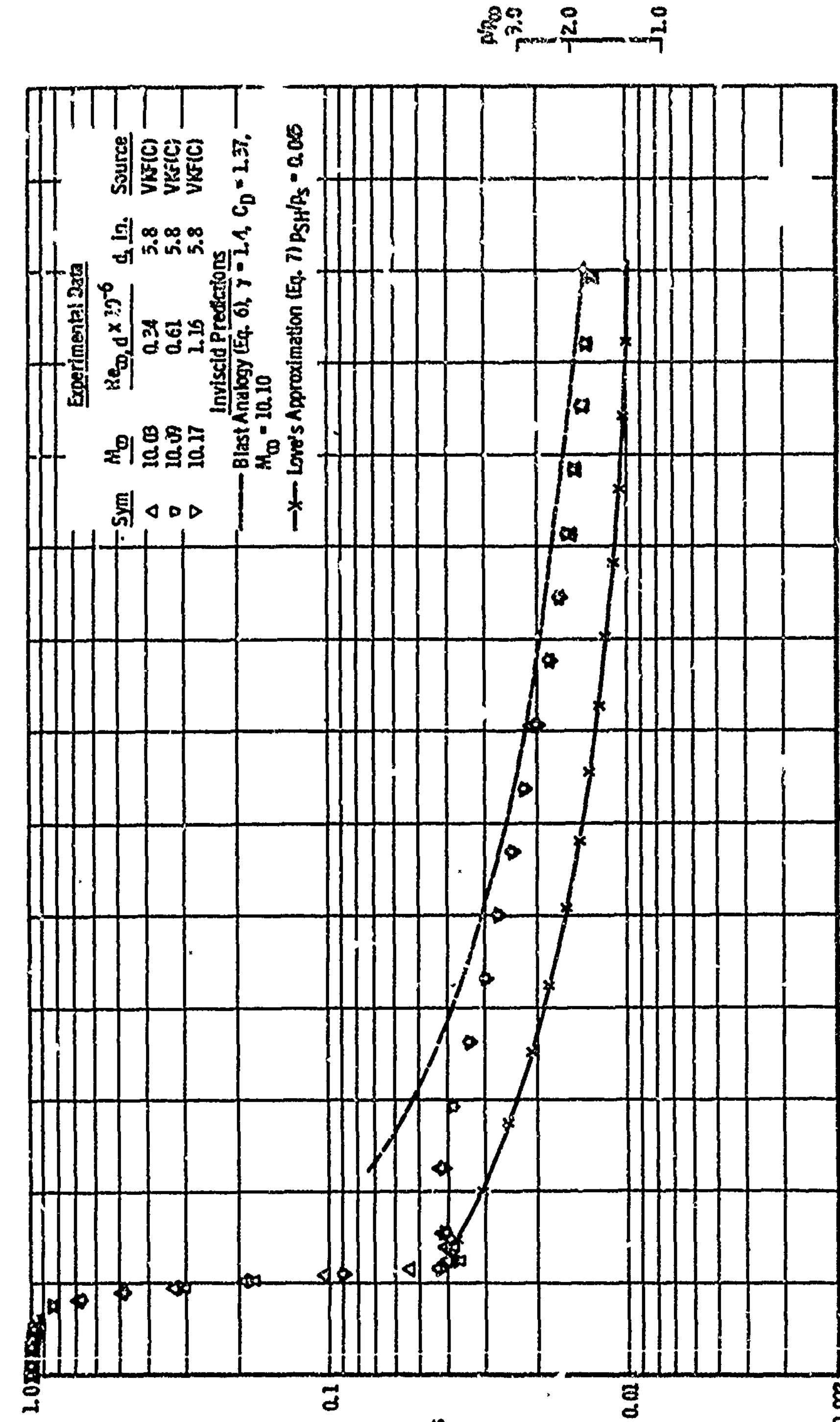

c. $M_\infty = 10$

Fig. 14 Continued

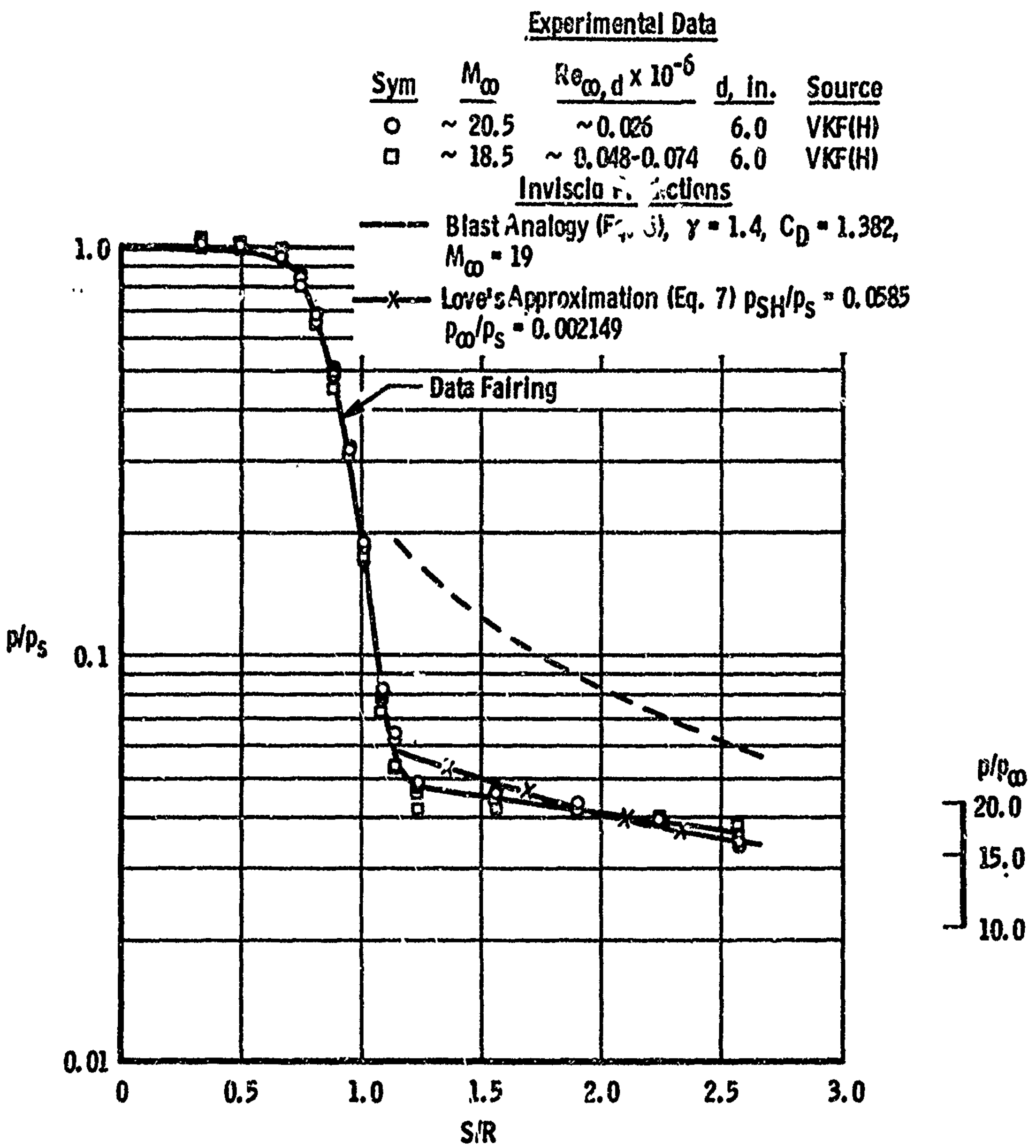

d. M_∞ = 19
Fig. 14 Concluded

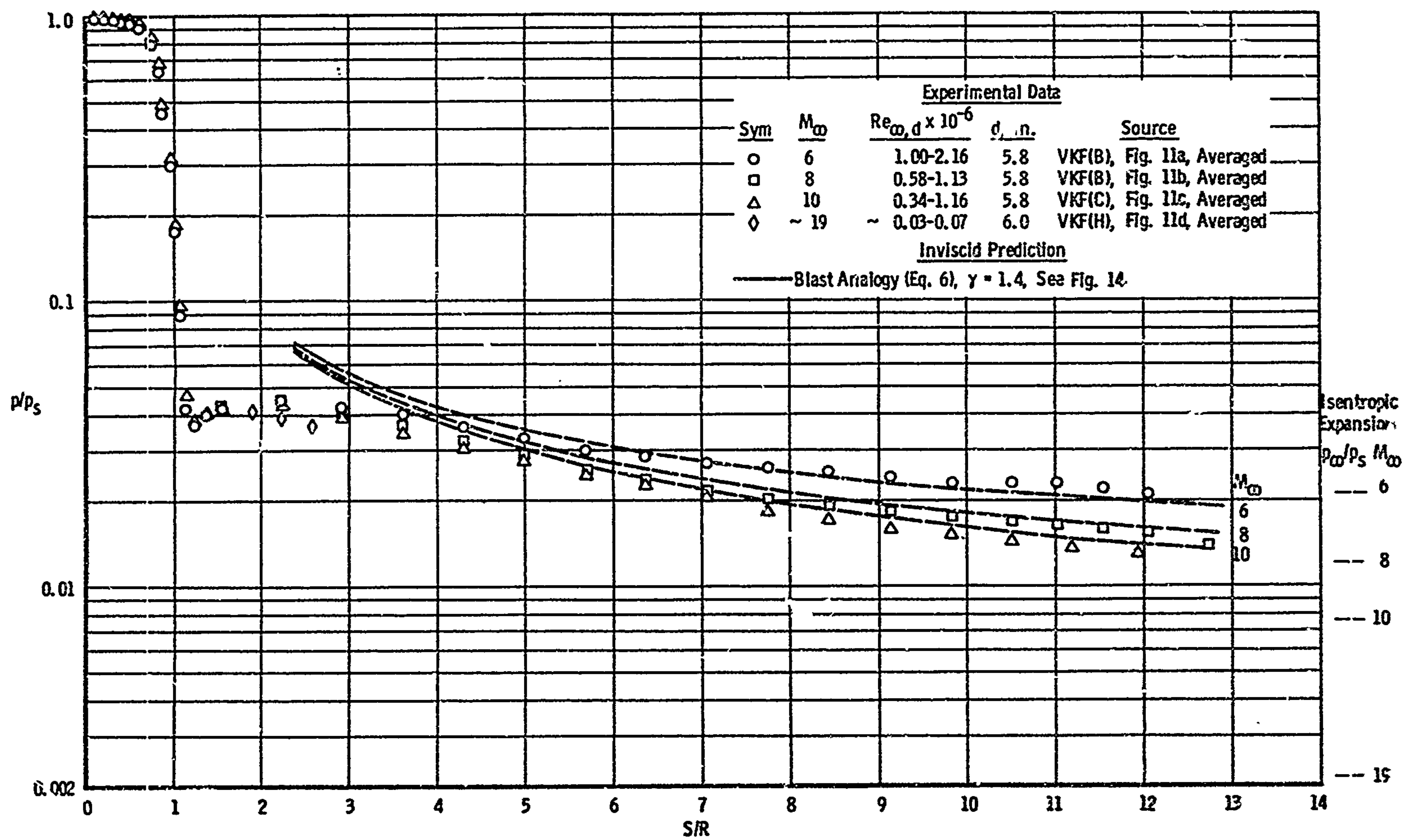

Fig. 15 Rounded-Shoulder Flat-Face Cylinder Model Pressure Data Summary

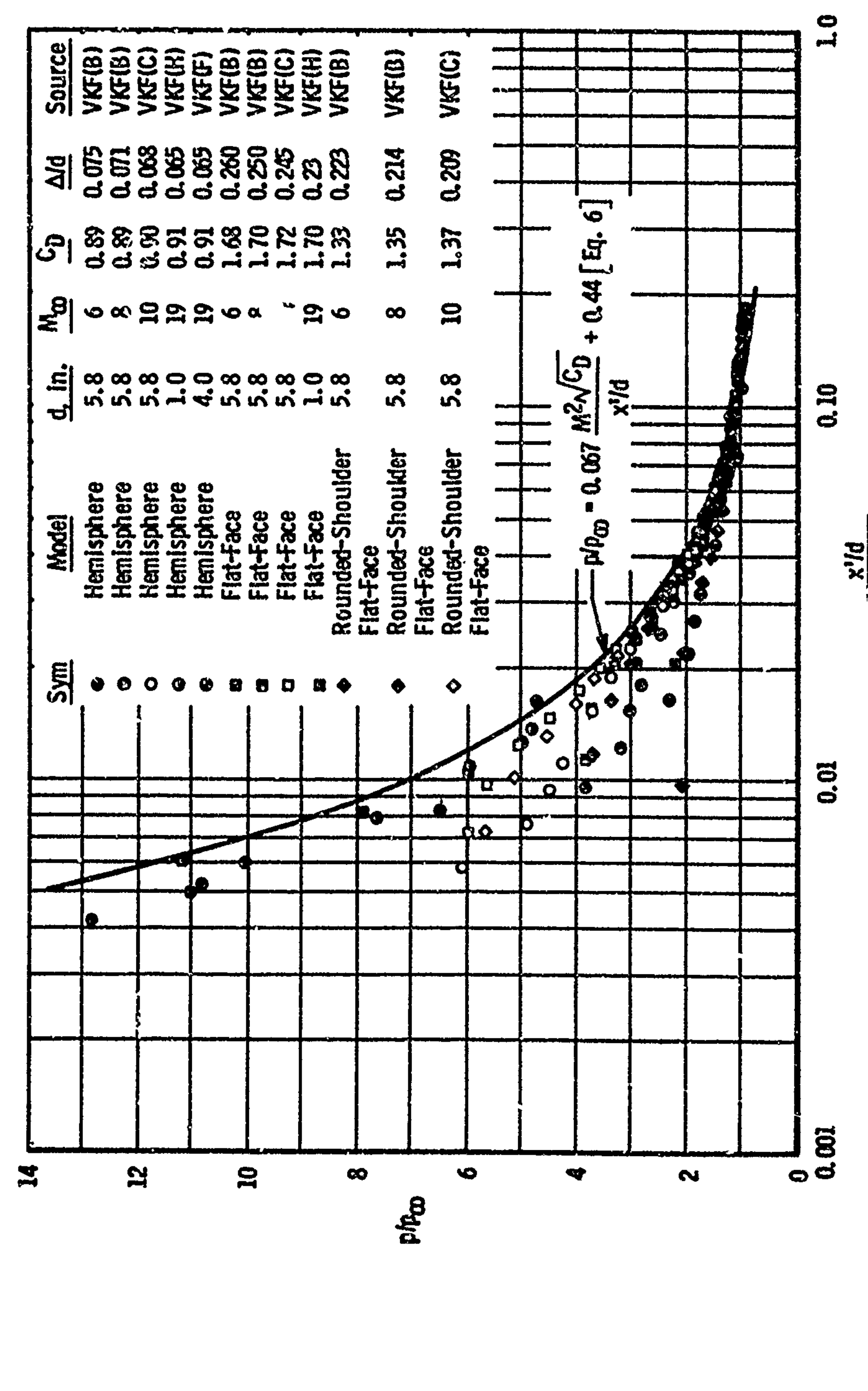

Fig. 16 Afterbody Pressure Distributions Correlated by the Blast Analogy

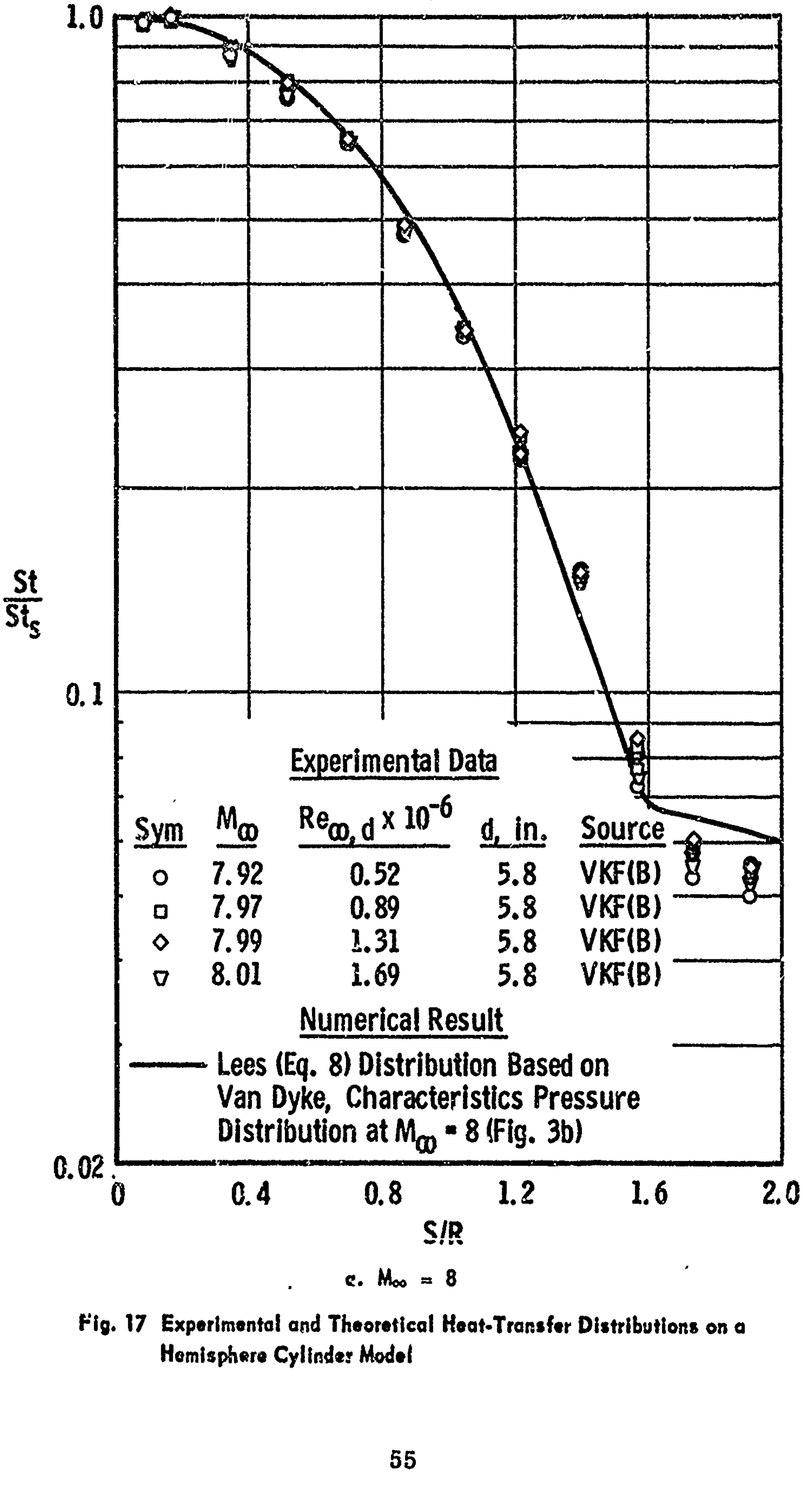

c. $M_\infty = 8$

Fig. 17 Experimental and Theoretical Heat-Transfer Distributions on a Hemisphere Cylinder Model

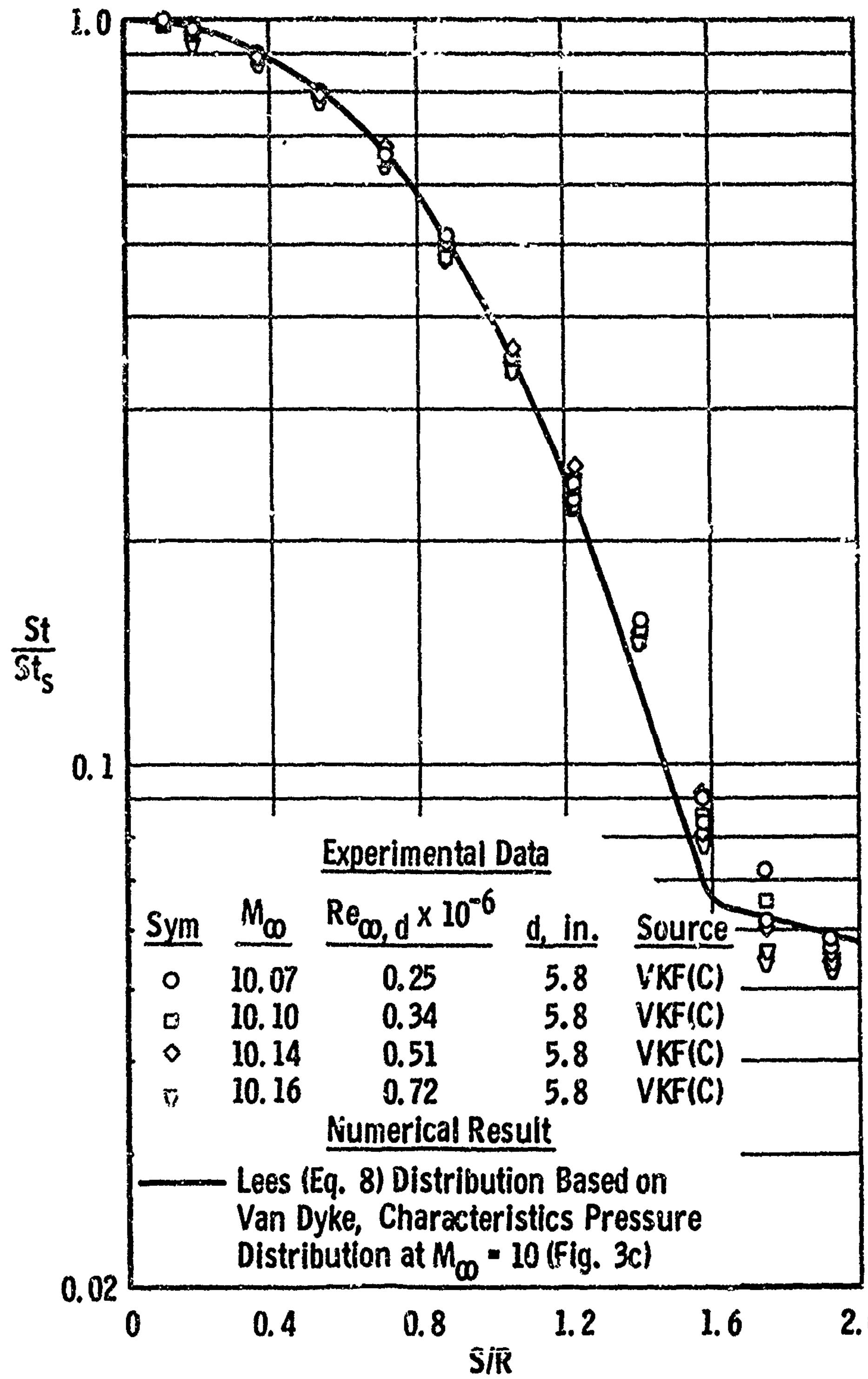

b. M_∞ = 10

Fig. 17 Continued

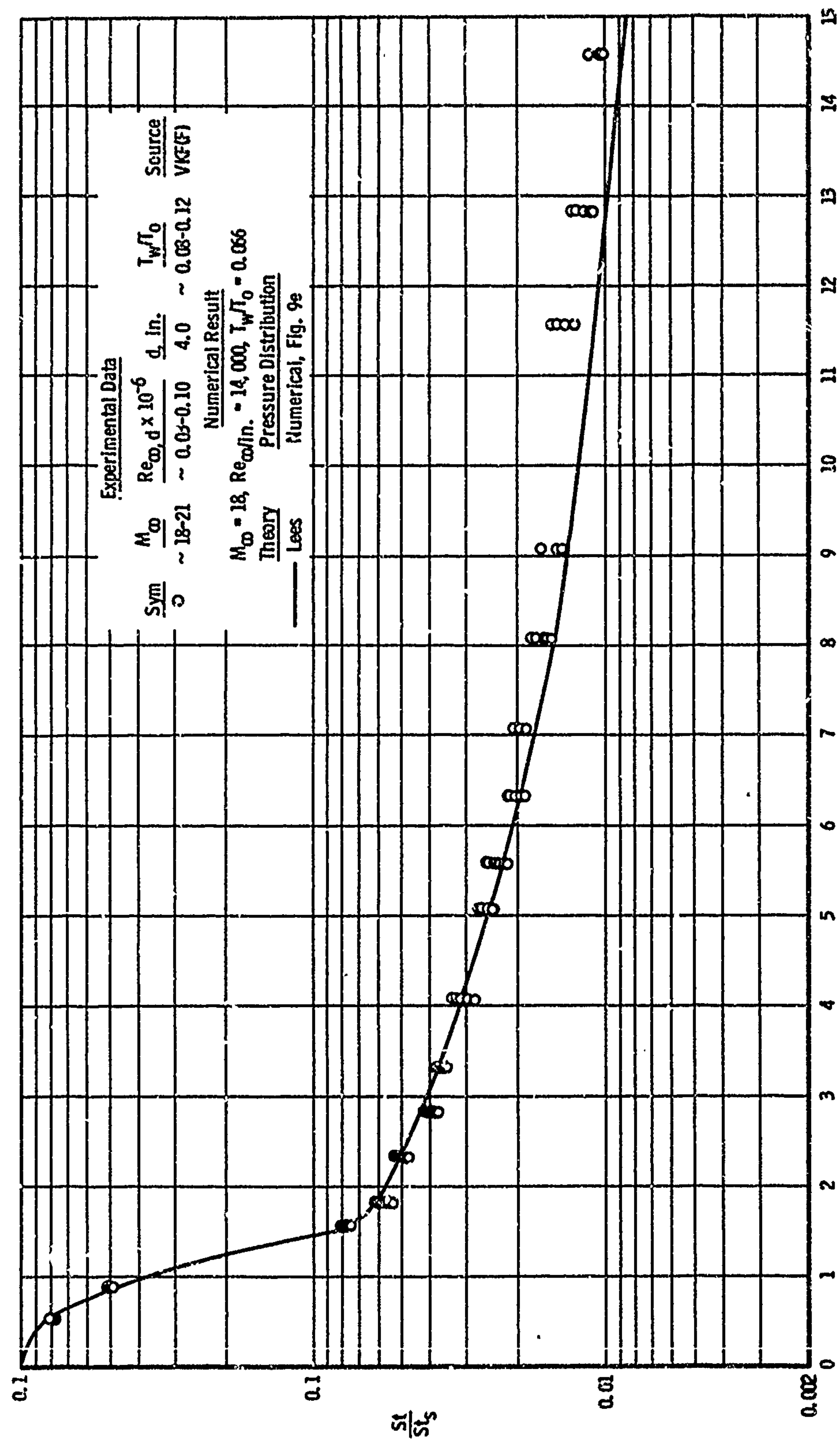

c. M_∞ = 19
Fig. 17 Concluded

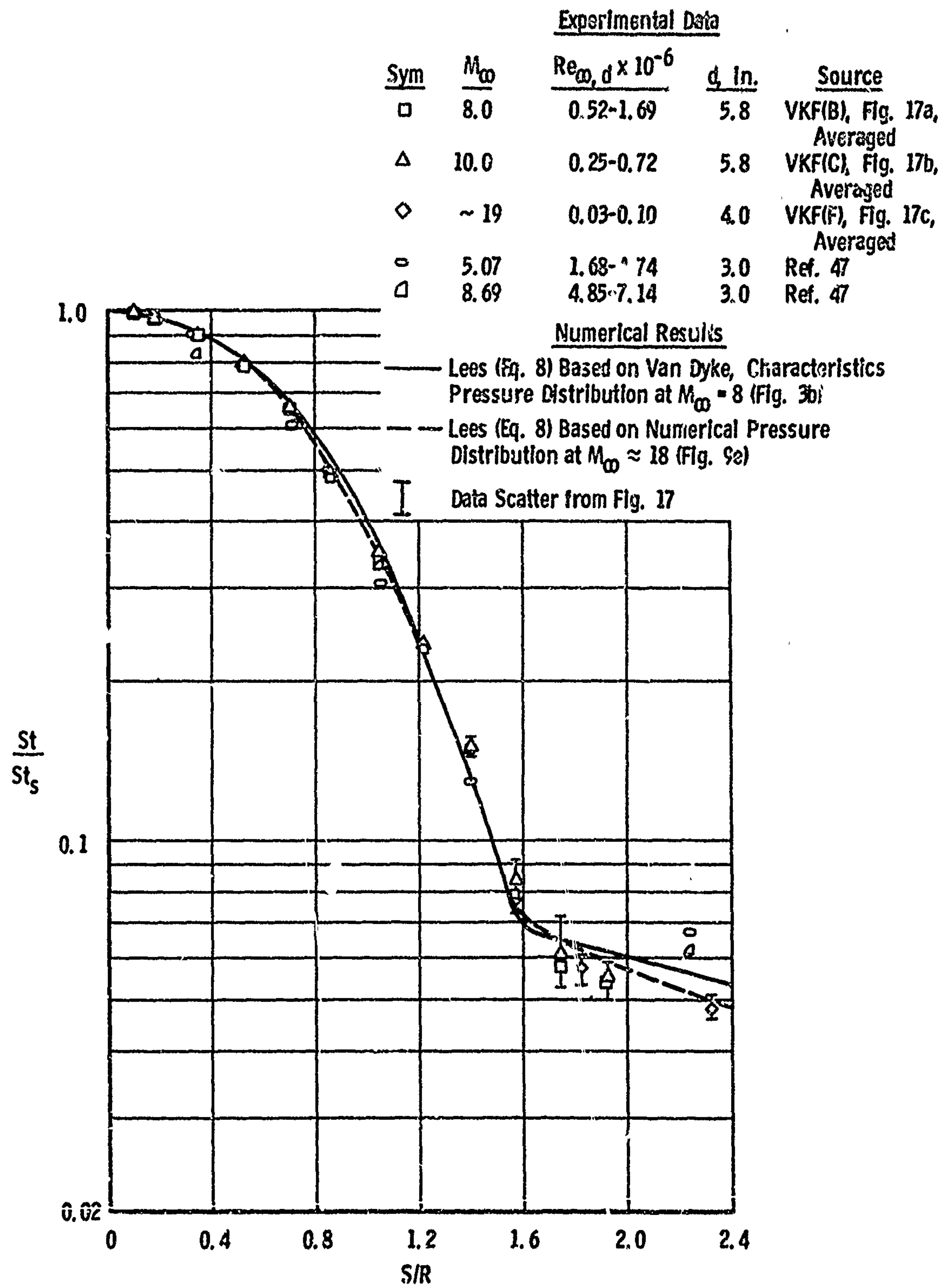

Fig. 18 Hemisphere Cylinder Model Heat-Transfer Data Summary

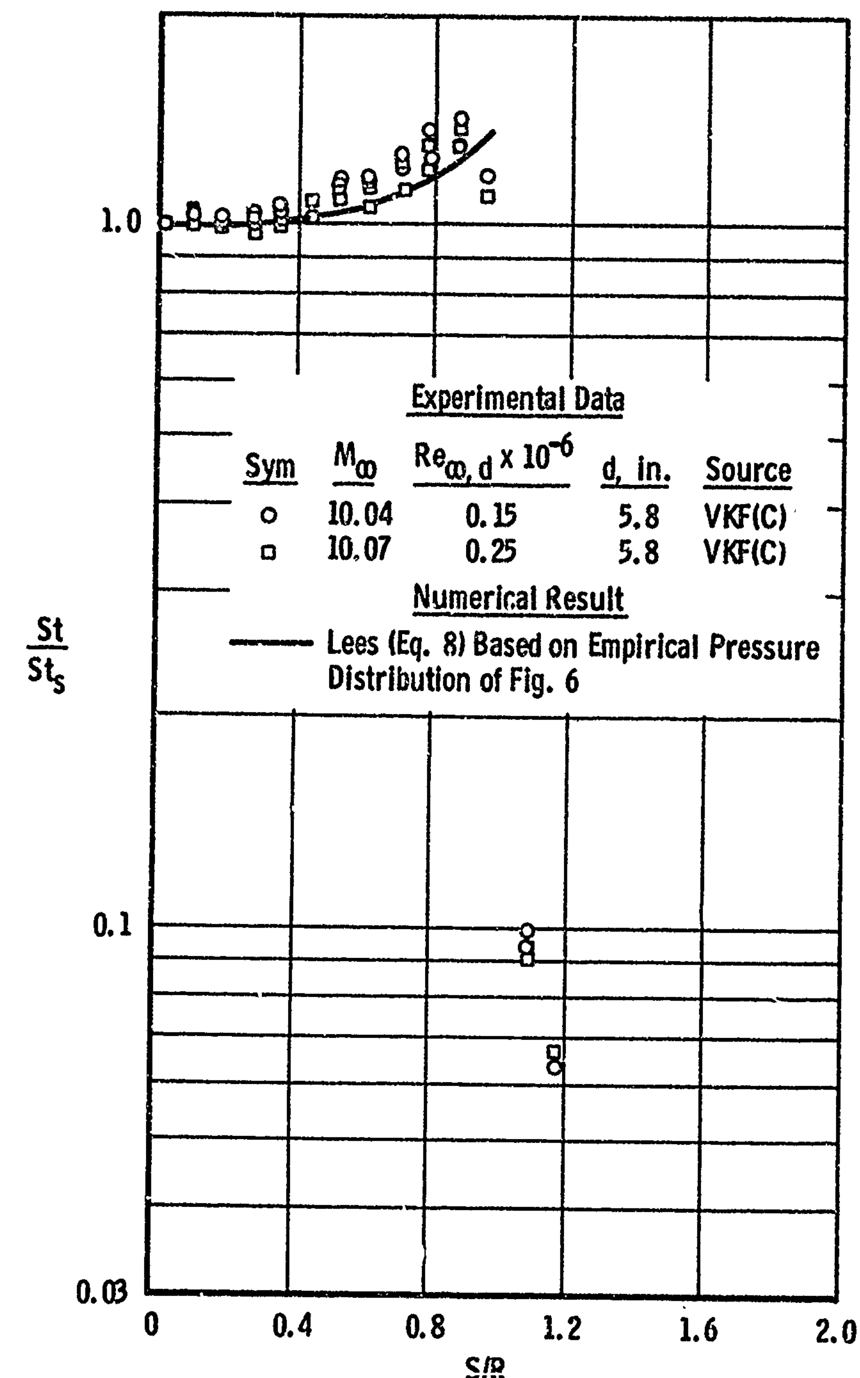

a. $M_\infty = 10$

Fig. 19 Experimental and Theoretical Heat-Transfer Distributions on a Flat-Face Cylinder Model

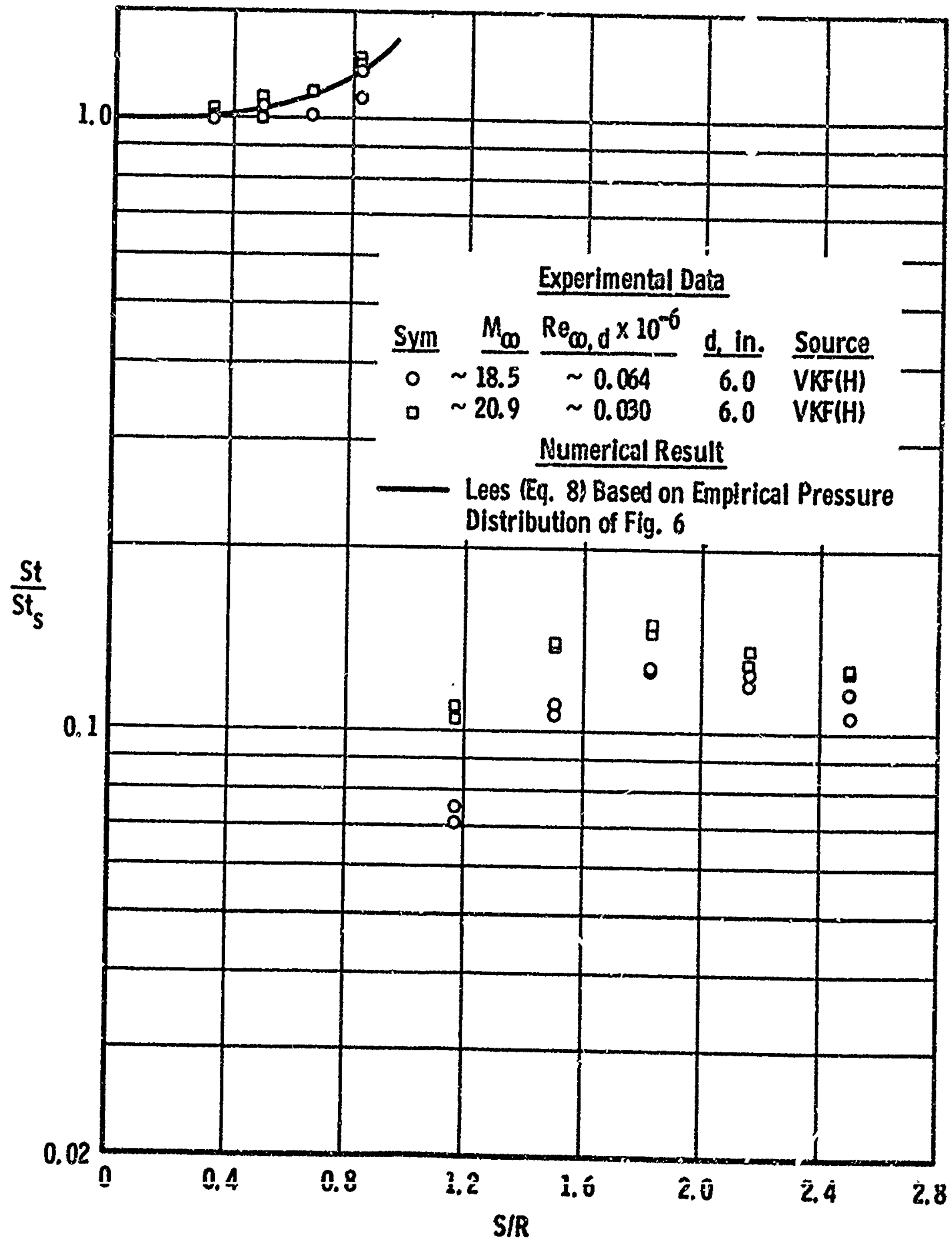

b. $M_\infty = 19$
Fig. 19 Concluded

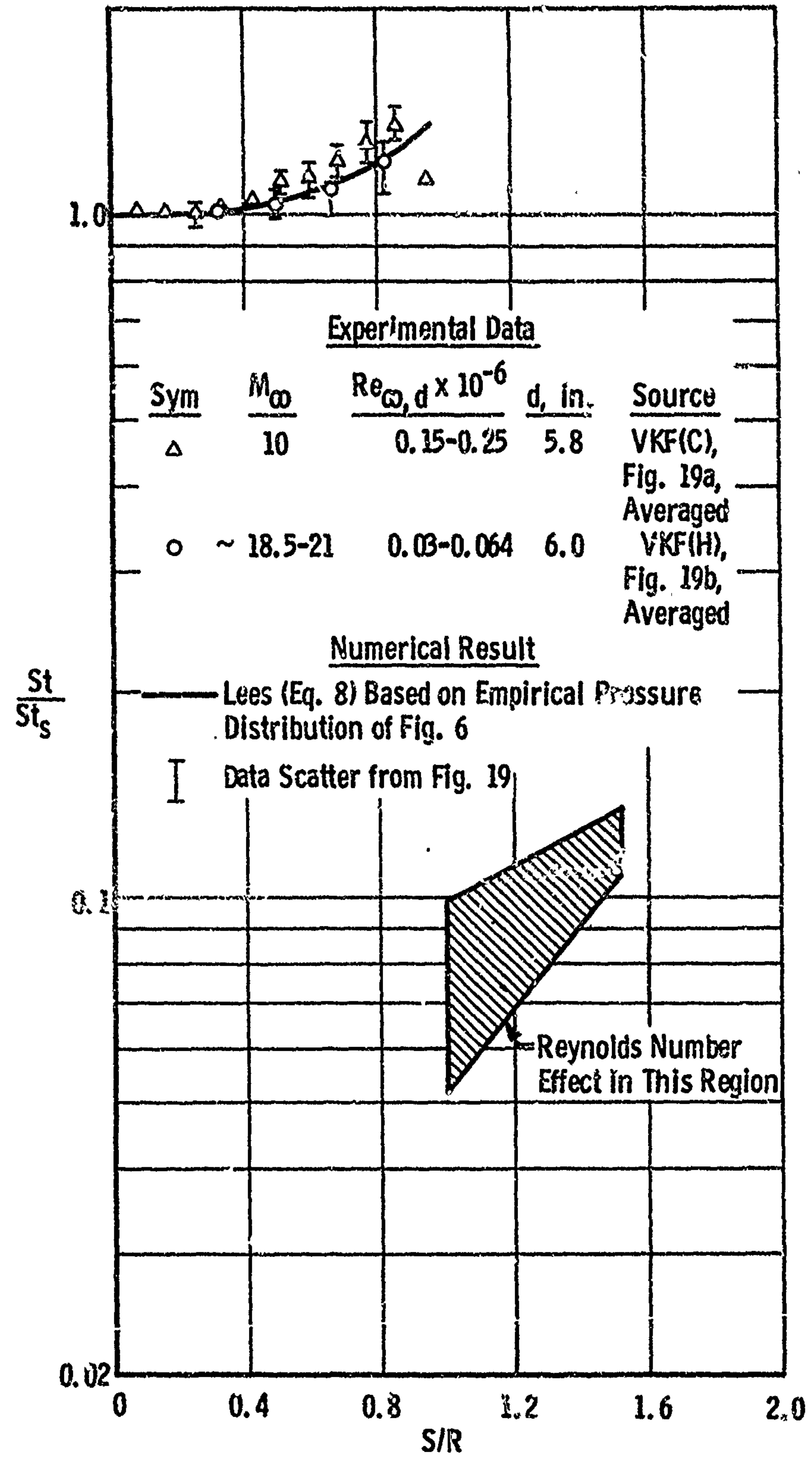

Fig. 20 Flat-Face Cylinder Model Heat-Transfer Data Summary

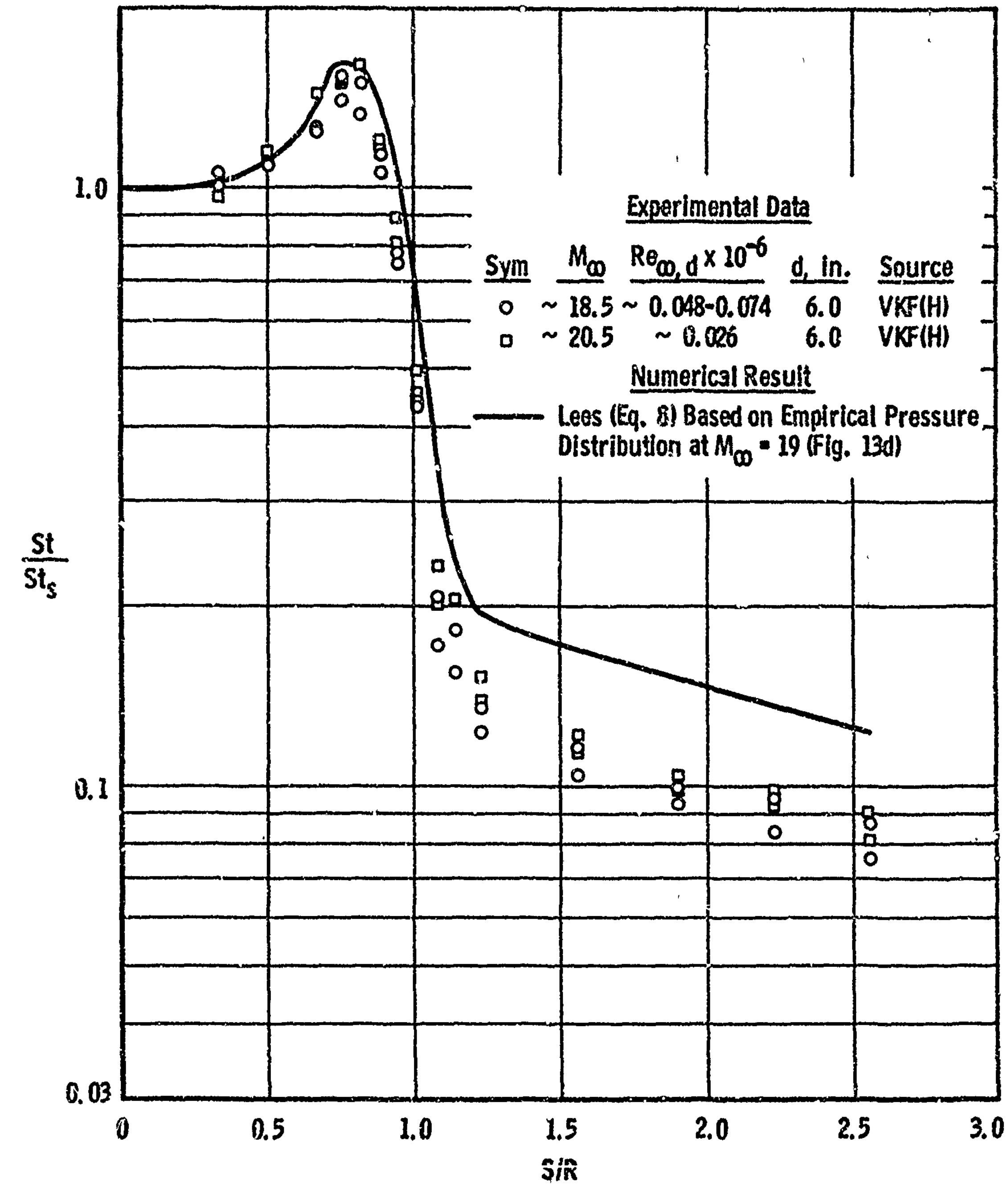

Fig. 21 Experimental and Theoretical Heat-Transfer Distributions on a Rounded-Shoulder Flat-Face Cylinder Model at M_∞ = 19

TABLE I
SUMMARY OF TEST CONDITIONS AND DATA SOURCES

Model	d, in.	M_∞	$Re_{\infty,d} \times 10^{-6}$	Source	Reference	Type Data° Pressure	Type Data° Heat
Hemisphere Cylinder	5.8	6	0.18-2.16	AEDC - VKF(B)	Present Data	N - A	N - A
	5.8	8	0.57-1.68	AEDC - VKF(B)	↓	N - A	N - A
	5.8	10	0.34-1.15	AEDC - VKF(C)	↓	N - A	N - A
	4.0	19	0.014-0.055	AEDC - VKF(F)‡	↓	N - A	N - A
	1.0	19	0.013	AEDC - VKF(H)	↓	A	----
	5.8	5-8	1.28-2.96	Baer, AEDC - VKF	36	N - A	----
	5.8-1.38	10	0.15-0.63	Clark, AEDC - VKF(C)	4	N - A	----
	3.0	4.76	1.50	Kendall, JPL 20-in.	37	N	----
	1.5	5	0.42	Reichle, NASA-MSFC 12-in.	39	N	----
	3.0	5-8.7	1.68-7.14†	Laumann, JPL 20-in.	47		N
	3.0-3.025	6.8	0.52-1.1	Crawford and McCauley, Langley 11-in.	38	N	----
	0.625	14.4	0.0062	Kuehn, Ames 6-in.	45	A	----
	5.0	15.5	0.103	Ellison, CAL 46-in.	40	N - A	N - A
Flat-Face Cylinder	2.9	8	1.68	AEDC - VKF(E)	Present Data	N	----
	5.8	6	0.97-2.12	AEDC - VKF(B)	↓	N - A	----
	5.8	8	0.14-1.13	AEDC - VKF(B)	↓	N - A	----
	5.8	10	0.14-1.16	AEDC - VKF(C)	↓	N - A	N - A
	6.0	19	0.030-0.064	AEDC - VKF(H)	↓	N - A	N - A
	1.0	19	0.0094	AEDC - VKF(H)	↓	A	----
	3.0	4.76	1.03	Bolson and Curtiss, JPL 20-in.	43	N	---
	2.5	4.76	1.25	Kendall, JPL 20-in.	37	N	----
	3.0	4.8-7.9	0.19-0.93†	Chones, NOL (SWT 2)	42	N	----
	0.625	14.4	0.0062	Kuehn, Ames 6-in.	40	A	----
Rounded-Shoulder Flat-Face Cylinder	5.8	6	1.00-2.16	AEDC - VKF(B)	Present Data	N - A	----
	5.8	8	0.47-1.13	AEDC - VKF(B)	↓	N - A	----
	5.8	10	0.14-1.16	AEDC - VKF(C)	↓	N - A	----
	6.0	19	0.026-0.074	AEDC - VKF(H)	↓	N - A	N - A

° N - Nose Data
A - Afterbody Data
† The exact Reynolds number for the data presented is not specified in the reference.
‡ Some previously reported data in Ref. 27.

TABLE II
HEMISPHERE AND HEMISPHERE CYLINDER PRESSURE DATA

Model →	Hemisphere																	
d, in.	5.8																	
Tunnel	B												C					
M_∞	5.98		5.99		6.05		7.99		8.02		8.01		10.10		10.16		10.20	
$Re_\infty \times 10^{-5}$, in.$^{-1}$	0.032		0.157		0.228		0.16		0.23		0.29		0.058		0.106		0.198	
p_∞, psia	0.013		0.063		0.090		0.041		0.061		0.081		0.011		0.121		0.041	
p_o, psia	20		98		150		399		601		798		498		1001		1099	
T_o, °R	836		843		848		1270		1317		1340		1741		1843		1918	
p_s, psia	0.593		2.929		4.207		3.406		5.069		6.725		1.445		2.832		5.559	
S/R	$(p/p_s)_+$	$(p/p_s)_-$	$(p/p_s)_+$	$(p/p_s)_-$	$(p/p_s)_+$	$(p/p_s)_-$	$(p/p_s)_+$	$(p/p_s)_-$	$(p/p_s)_+$	$(p/p_s)_-$	$(p/p_s)_+$	$(p/p_s)_-$	$(p/p_s)_+$	$(p/p_s)_-$	$(p/p_s)_+$	$(p/p_s)_-$	$(p/p_s)_+$	$(p/p_s)_-$
0	1.000	1.000	1.000	1.000	1.000	1.000	1.000	1.000	1.000	1.000	1.000	1.000	1.000	1.000	1.000	1.000	1.000	1.000
0.17	0.989	0.995	0.942	0.957	0.984	0.969	0.974	0.974	0.974	0.974	0.968	0.968	0.969	0.972	0.971	0.978	0.975	0.976
0.35	0.905	0.905	0.825	0.836	0.851	0.826	0.882	0.881	0.883	0.882	0.874	0.873	0.876	0.863	0.877	0.886	0.885	0.888
0.52	0.762	0.763	0.688	0.695	0.710	0.715	0.737	0.737	0.737	0.738	0.730	0.729	0.739	0.737	0.735	0.739	0.733	0.739
0.70	0.591	0.597	0.537	0.541	0.552	0.553	0.562	0.565	0.562	0.559	0.559	0.563	0.568	0.573	0.566	0.564	0.558	0.563
0.87	0.424	0.430	0.384	0.385	0.395	0.395	0.396	0.396	0.395	0.395	0.391	0.394	0.401	0.407	0.395	0.398	0.394	0.392
1.05	0.279	0.284	0.253	0.255	0.261	0.259	0.256	0.257	0.256	0.258	0.250	0.254	0.258	0.267	0.256	0.257	0.255	0.253
1.22	0.168	0.173	0.154	0.155	0.159	0.159	0.155	0.155	0.154	0.154	0.149	0.151	0.156	---	0.152	0.156	0.151	0.151
1.40	0.096	0.100	0.088	0.089	0.090	0.090	0.085	0.086	0.084	0.085	0.082	0.083	0.089	0.091	0.084	0.087	0.082	0.084
1.57	0.093	0.057	0.049	0.050	0.050	0.050	0.047	0.047	0.046	0.046	0.044	0.044	0.049	0.049	0.046	0.048	0.044	0.046

Note: + Measured along model upper surface
- Measured along model lower surface

TABLE II (Continued)

Model →	Hemisphere-Cylinder						
d, in.	5.8						
Tunnel	B				C		
M_∞	6.00	6.07	7.98	7.99	10.03	10.08	10.17
$Re_\infty \times 10^{-6}$, in.$^{-1}$	0.172	0.373	0.098	0.191	0.058	0.106	0.198
p_∞, psia	0.073	0.149	0.026	0.052	0.011	0.021	0.041
p_o, psia	115	252	254	506	498	1001	[illegible]
T_o, °R	857	[illegible]	[illegible]	1318	1741	1843	1918
p_s, psia	3.40	[illegible]	2.160	4.322	1.445	[illegible]	5.559
S/r	$(p/p_s)_+$	$(p/p_s)_+$	(p/p_s)	(p/p_s)	$(p/p_s)_-$	$(p/p_s)_-$	$(p/p_s)_+$
1.92	0.041	0.042	0.039	0.038	0.039	0.037	0.036
2.26	---	0.040	0.037	0.036	0.035	0.034	0.033
2.61	0.036	0.037	0.034	0.034	0.033	0.032	0.031
3.41	0.032	0.032	0.030	0.030	0.028	0.028	0.028
4.10	0.030	0.030	0.027	0.027	0.025	0.026	0.026
4.78	0.028	0.028	0.025	0.025	0.025	0.022	0.022
5.47	0.026	0.027	0.023	0.022	0.020	0.020	0.020
6.16	0.025	0.025	0.021	0.021	0.018	0.019	0.019
6.85	0.024	0.024	0.020	0.019	0.017	0.017	0.017
7.55	0.023	0.023	0.019	0.018	0.017	0.016	0.016
8.24	0.022	0.023	0.018	0.017	0.016	0.016	0.015
8.93	0.022	0.022	0.017	0.016	0.015	0.014	0.014
9.62	0.021	0.022	0.016	0.016	0.013	0.013	0.014
10.30	0.021	0.021	0.016	0.015	0.013	0.013	0.013
11.00	0.021	0.021	0.016	0.015	0.012	0.012	0.012
11.68	---	0.021	0.015	0.014	0.012	0.012	0.012
12.20	0.021	0.021	0.015	0.014	---	---	---
12.38	---	---	---	---	---	0.013	0.011
12.72	0.020	0.021	0.014	0.014	---	---	---
13.06	---	---	---	---	0.012	0.011	0.011
13.22	0.020	0.021	0.014	0.014	---	---	---
13.91	---	---	0.012	0.012	---	---	---

TABLE II (Continued)

Model	Hemisphere-Cylinder																			
d, in.	4																			
Tunnel	H																			
M_∞	18.0		18.2		18.3		18.5		18.5		18.8		19.1		20.6		20.8		20.8	
$Re_\infty \times 10^{-6}$, in.$^{-1}$	0.0053		0.00845		0.01040		0.00990		0.01160		0.00993		0.01380		0.00355		0.00437		0.00541	
p_∞, psia	0.00175		0.00159		0.00152		0.00161		0.00181		0.00150		0.00142		0.00050		0.00057		0.00055	
p_o, psia	8330		7100		6460		7550		8560		8010		7390		6080		7080		5760	
T_o, °R	8100		7130		6200		6540		6590		6860		5530		8280		8540		7150	
p_s, psia	0.787		0.695		0.734		0.744		0.755		0.756		0.708		0.284		0.349		0.330	
S/R	$(p/p_s)_+$	$(p/p_s)_-$	$(p/p_s)_+$	$(p/p_s)_-$	$(p/p_s)_+$	$(p/p_s)_-$	$(p/p_s)_+$	$(p/p_s)_-$	$(p/p_s)_+$	$(p/p_s)_-$	$(p/p_s)_+$	$(p/p_s)_-$	$(p/p_s)_+$	$(p/p_s)_-$	$(p/p_s)_+$	$(p/p_s)_-$	$(p/p_s)_+$	$(p/p_s)_-$	$(p/p_s)_+$	$(p/p_s)_-$
0.262	0.92[illegible]		0.965		0.980		0.962		0.985		0.928		0.980		0.890		0.935		0.962	
0.524		0.715		0.762		0.680		0.700		0.765		0.693		0.734		0.716		0.720		0.889
0.889	0.37[illegible]		0.385		0.392		0.398		0.431		0.366		0.406		0.390		0.398		0.400	
1.22		0.150		0.155		0.147		0.151		0.156		0.140		0.157		0.162		0.162		0.155
1.57	0.0418		0.0437		0.0427		0.0445		0.0461		0.0416		0.0437		0.0492		0.0484		0.0492	
1.82		0.0389		0.0389		0.0348		0.0350		0.0379		0.0341		0.0357		0.0398		0.0398		0.0378
2.32	0.0318		0.0328		0.0294		0.0324		0.0329		0.0309		0.0327		0.0334		0.0330		0.0324	
2.82		0.0260		0.0269		0.0245		0.0249		0.0256		0.0247		0.0254		0.0254		0.0249		0.0241
3.32	0.0217		0.0243		0.0226		0.0281		0.0248		0.0239		0.0238		0.0227		0.0239		0.0223	

TABLE II (Concluded)

Model ⟶	Hemisphere-Cylinder																
d, in.	4															1	
Tunnel	F															H	
M_∞	18.1		18.2		19.0		19.3		19.3		19.8		20.1			18.8	19.0
$Re_\infty \times 10^{-6}$, in.$^{-1}$	0.0237		0.0258		0.00748		0.00820		0.00830		0.00952		0.0131			0.0130	0.0135
p_∞, psia	0.00250		0.00250		0.00116		0.00108		0.00112		0.00101		0.00105			0.00130	0.00140
p_o, psia	8170		8140		6810		7000		7080		7210		7360			6720	6950
T_o, °R	5000		4740		7050		6710		6750		6200		5370			6400	0.5450
p_s, psia	1.12		1.04		0.534		0.525		0.563		0.540		0.609			0.607	0.634
S/R	$(p/p_s)_+$	$(p/p_s)_-$	$(p/p_s)_+$	$(p/p_s)_-$	$(p/p_s)_+$	$(p/p_s)_-$	$(p/p_s)_+$	$(p/p_s)_-$	$(p/p_s)_+$	$(p/p_s)_-$	$(p/p_s)_+$	$(p/p_s)_-$	$(p/p_s)_+$	$(p/p_s)_-$	S/R	$(p/p_s)_+$	$(p/p_s)_+$
0.524		0.715		0.743		0.719		0.746		0.706		0.714		0.711	2.17	0.0384	0.0385
0.873					0.383		0.393		0.368		0.378		0.379		3.87	0.0232	0.0246
1.57	0.0443		0.0462		0.0481		0.0496		0.0468		0.0478		0.0468		5.87	0.0160	0.0172
1.82		0.0382		0.0394		0.0400		0.0415		0.0396		0.0400		0.0394	7.87	0.0123	0.0135
2.32			0.0322		0.0325		0.0342				0.0329		0.0320		9.87	0.0100	0.0107
2.82		0.0289		0.0294		0.0288		0.0301		0.0298		0.0294		0.0281			
3.32	0.0257		0.0262		0.0264		0.0273		0.0260		0.0253		0.0251				
4.07		0.0223		0.0221				0.0232		0.0216				0.0216			
4.57	0.0210	0.0208	0.0209	0.0199			0.0227	0.0206	0.0208	0.0195			0.0206	0.0190			
7.07	0.0147		0.0143				0.0136		0.0130				0.0132				
9.07		0.0110		0.0114				0.0106		0.0101				0.0094			
11.57	0.0102		0.0105				0.0101		0.0096				0.0093				
14.57		0.0075								0.0061				0.0065			

TABLE III
FLAT-FACE AND FLAT-FACE CYLINDER PRESSURE DATA

Model →	Flat-Face															
d, in.	2.9		5.8													
Tunnel	E		B										C			
M_∞	6.02		6.06		6.09		7.84		7.92		7.98		10.01		10.11	
$Re_\infty \times 10^{-6}$, in.$^{-1}$	0.579		0.169		0.365		0.024		0.086		0.157		0.024		0.057	
p_∞, psia	0.248		0.066		0.149		0.006		0.022		0.041		0.004		0.011	
p_o, psia	400		112.5		245		51		203		396		180		504	
T_o, °R	870		856		852		1150		1230		1280		1630		1767	
p_s, psia	11.62		3.18		6.79		0.474		1.796		3.404		0.543		1.457	
S/R	$(p/p_s)_+$	$(p/p_s)_-$	$(p/p_s)_+$	$(p/p_s)_-$	$(p/p_s)_+$	$(p/p_s)_-$	$(p/p_s)_+$	$(p/p_s)_-$	$(p/p_s)_+$	$(p/p_s)_-$	$(p/p_s)_+$	$(p/p_s)_-$	$(p/p_s)_+$	$(p/p_s)_-$	$(p/p_s)_+$	$(p/p_s)_-$
0	1.000	1.000	1.000	1.000	1.000	1.000	1.000	1.000	1.000	1.000	1.000	1.000	1.000	1.000	1.000	1.000
0.10	---	---	---	0.999	1.003	0.999	---	---	---	---	---	---	1.002	0.998	1.000	1.002
0.15	---	0.999	---	0.994	---	---	0.999	0.998	0.998	0.997	---	0.999	1.002	0.997	0.997	0.999
0.20	---	0.999	0.999	---	1.005	0.997	1.003	---	1.001	---	1.002	---	0.999	0.997	0.999	0.999
0.25	0.997	---	---	0.904	1.007	0.996	---	0.996	---	0.993	---	0.998	1.003	0.994	0.999	1.003
0.30	---	0.995	---	0.998	---	---	0.998	0.990	0.988	9.993	---	1.000	1.003	0.996	0.999	1.002
0.35	---	0.995	0.994	---	1.006	0.993	1.000	---	---	---	1.002	---	0.999	0.994	0.998	1.000
0.40	---	---	---	0.087	1.004	0.991	---	0.993	---	0.984	---	0.996	0.999	0.993	0.993	[illegible]
0.45	---	0.988	---	0.980	---	---	0.998	0.989	0.983	---	---	0.993	0.995	0.992	0.991	0.995
0.50	0.985	---	0.984	--	0.997	0.986	0.885	---	---	0.970	0.994	-	0.990	0.989	0.991	0.995
0.55	0.982	---	---	0.973	0.991	0.984	---	0.977	0.923	0.971	---	0.984	0.987	0.987	0.986	0.994
0.60	---	0.975	---	0.968	---	---	0.978	0.967	0.964	---	---	0.984	0.981	0.980	0.981	0.986
0.65	0.969	---	0.967	---	0.978	0.973	0.968	---	---	0.949	0.980	---	0.975	0.975	0.978	0.979
0.70	0.958	---	---	0.954	0.968	0.966	---	0.957	0.946	0.943	---	0.966	0.964	0.969	0.967	0.976
0.75	---	0.946	---	0.942	---	---	0.950	0.955	0.931	---	---	0.957	0.953	0.960	0.957	0.965
0.80	0.934	---	0.935	---	0.942	0.942	0.935	---	---	0.905	0.944	---	0.937	0.942	0.942	0.948
0.85	0.911	---	---	0.908	0.922	0.923	---	0.915	0.879	0.877	---	0.921	0.911	0.924	0.921	[illegible]
0.90	---	0.880	---	0.877	---	---	0.885	0.881	0.838	---	---	0.892	0.882	0.896	0.893	[illegible]
0.95	0.823	---	0.845	---	0.855	0.856	0.840	---	---	0.774	0.852	---	0.838	0.851	0.854	[illegible]
0.98	0.766	---	---	---	0.795	0.795	---	0.774	---	---	---	0.792	0.770	0.784	0.791	[illegible]

TABLE III (Concluded)

Model →	Flat-Face Cylinder														
d, in.	5.8								1			6			
Tunnel	B				C				H			H			
M_∞	6.01	6.05	7.97	8.00	10.03	10.10	10.17		18.4	18.5		17.9	19.0	20.6	21.1
$Re_\infty \times 10^{-6}$, in.$^{-1}$	0.169	0.367	0.099	0.195	0.058	0.105	0.200		0.00872	0.0101		0.0103	0.0111	0.00448	0.00542
p_∞, psia	0.070	0.151	0.026	0.052	0.011	0.021	0.041		0.00147	0.00146		0.00194	0.00167	0.00066	0.00057
p_o, psia	112	251	252	511	505	1000	2002		6840	6700		7550	9420	7840	7020
T_o, °R	856	865	1287	1308	1754	1852	1906		6850	6300		6900	6900	8350	7200
p_s, psia	3.30	7.18	2.175	4.348	1.458	2.832	5.577		0.676	0.650		0.815	0.78	0.369	0.333
S/R	$(p/p_s)_+$	$(p/p_s)_+$	$(p/p_s)_-$	$(p/p_s)_-$	$(p/p_s)_-$	$(p/p_s)_+$	$(p/p_s)_-$	S/R	$(p/p_s)_+$	$(p/p_s)_+$	S/R	$(p/p_s)_+$	$(p/p_s)_+$	$(p/p_s)_+$	$(p/p_s)_+$
1.03	0.008	0.011	0.006	0.005	0.015	0.010	0.007	2.6	0.0419	0.0451	0.167	1.02	0.990	0.985	0.980
1.17	0.014	0.013	0.011	0.013	0.019	0.013	0.014	4.3	0.0315	0.0334	0.333	0.995	1.03	---	0.985
1.35	0.017	0.015	0.021	0.020	0.023	0.020	0.020	6.3	0.0247	0.0256	0.500	0.930	0.943	---	0.945
1.65	0.014	---	0.035	0.034	0.038	0.033	0.034	8.3	0.0172	0.0182	0.666	0.960	0.950	0.912	0.912
2.34	0.045	0.048	0.047	0.046	0.045	0.046	0.046	10.3	0.0131	0.0138	0.833	0.907	0.883	0.877	0.921
3.03	---	---	0.045	0.045	0.041	0.044	0.043				1.17	0.0159	0.0177	0.0191	0.0229
3.72	0.043	0.043	0.041	0.040	0.038	0.039	0.038				1.50	0.0293	0.0323	0.0357	0.0371
4.41	0.040	0.040	0.036	0.036	0.033	0.035	0.034				1.83	0.0374	0.0401	0.0386	0.0427
5.10	---	---	0.032	0.032	0.029	0.031	0.031				2.16	0.0422	0.0430	0.0422	0.0443
5.78	0.033	0.033	0.029	0.029	0.026	0.028	0.028				2.50	0.0431	0.0452	0.0402	0.0434
6.47	0.031	0.031	0.026	0.026	0.025	0.025	0.025								
7.16	---	---	0.024	0.024	0.023	0.023	0.023								
7.85	0.027	0.028	0.022	0.022	0.019	0.020	0.029								
8.54	0.026	0.026	0.020	0.021	0.017	0.019	0.019								
9.24	0.025	0.025	---	0.020	0.017	0.017	0.018								
9.92	---	---	---	0.019	0.015	0.016	0.016								
10.61	0.024	0.024	0.018	0.018	0.014	0.015	0.016								
11.13	0.023	0.023	0.017	0.017	---	---	---								
11.30	---	---	---	---	0.013	0.014	0.015								
11.65	0.023	0.024	0.016	0.017	---	---	---								
11.99	---	---	---	---	---	0.014	0.014								
12.18	0.022	0.022	0.016	0.017	---	---	---								
12.87	0.021	0.022	0.015	0.016	---	---	---								

TABLE IV
ROUNDED-SHOULDER FLAT-FACE AND ROUNDED-SHOULDER FLAT-FACE CYLINDER PRESSURE DATA

Model →	Rounded-Shoulder Flat-Face										
d, in.	5.8										
Tunnel	B							C			
M_∞	6.02		6.05		7.81	7.98	8.00	10.01		10.01	
$Re_\infty \times 10^{-6}$, in.$^{-1}$	0.17		0.37		0.02	0.10	0.19	0.023		0.058	
p_∞, psia	0.069		0.150		0.005	0.026	0.061	0.004		0.011	
p_o, psia	111		252		50	251	511	175		506	
T_o, °R	850		856		1125	1287	1310	1644		1764	
p_s, psia	3.25		7.22		0.471	2.156	4.331	0.532		1.467	
S/R	$(p/p_s)_+$	$(p/p_s)_-$	$(p/p_s)_+$	$(p/p_s)_-$	$(p/p_s)_-$	$(p/p_s)_-$	$(p/p_s)_-$	$(p/p_s)_+$	$(p/p_s)_-$	$(p/p_s)_+$	$(p/p_s)_-$
0	1.000	1.000	1.000	1.000	1.000	1.000	1.000	1.000	1.000	1.000	1.000
0.10	1.000	0.995	0.998	0.999	0.999	0.997	0.997	1.001	0.999	1.001	1.003
0.20	1.002	0.990	0.996	0.993	0.993	0.994	0.994	1.000	0.995	1.002	1.001
0.30	0.995	0.982	0.984	0.988	0.997	0.992	0.988	0.996	0.994	1.000	1.003
0.40	0.986	0.976	0.971	0.981	0.992	0.987	0.982	0.992	0.988	0.996	0.999
0.50	0.968	0.9[illegible]6	0.953	0.967	0.981	0.978	0.970	0.981	0.978	0.985	0.971
0.60	0.944	0.947	0.929	0.942	0.951	0.957	0.951	0.958	0.958	0.970	0.972
0.75	0.833	0.838	0.826	0.825	0.842	0.856	0.848	0.844	0.859	0.855	0.857
0.82	0.664	0.667	0.666	0.652	0.680	0.695	0.688	0.678	0.703	0.715	0.713
0.88	0.475	0.471	0.479	0.457	0.497	0.506	0.498	0.492	0.516	0.512	0.509
0.95	0.311	0.306	0.310	0.297	0.327	0.328	0.322	0.319	0.338	0.335	0.330
1.01	0.173	0.175	0.176	0.170	0.193	0.189	0.185	0.189	0.200	0.197	0.193
1.08	0.094	0.090	0.088	0.086	0.108	0.098	0.094	0.101	0.111	0.105	0.103
1.14	0.043	0.041	0.039	0.039	0.046	0.047	0.044	0.053	0.062	0.054	0.055

TABLE IV (Concluded)

Model →	Rounded Shoulder Flat-Face Cylinder											
d, in.	5.8								6			
Tunnel	B				C				H			
M_∞	6.03	6.05	7.98	8.00	10.03	10.09	10.17		18.5	18.8	20.4	20.7
$Re_\infty \times 10^{-6}$, in.$^{-1}$	0.174	0.37	0.099	0.194	0.058	0.106	0.199		0.00804	0.0123	0.00410	0.00458
p_∞, psia	0.070	0.150	0.026	0.061	0.011	0.021	0.041		0.00144	0.00152	0.00058	0.00053
p_o, psia	116	252	251	511	507	1003	2000		7190	7470	6160	5930
T_o, °R	860	856	1287	1310	1764	1843	1909		7240	6000	7940	7330
p_s, psia	3.32	7.22	2.156	4.331	1.467	2.844	5.568		0.644	0.204	0.315	0.299
S/R	$(p/p_s)_+$	$(p/p_s)_+$	$(p/p_s)_-$	$(p/p_s)_-$	$(p/p_s)_+$	$(p/p_s)_+$	$(p/p_s)_-$	S/R	$(p/p_s)_+$	$(p/p_s)_+$	$(p/p_s)_+$	$(p/p_s)_+$
1.23	0.038	0.035	0.041	0.039	0.041	0.037	0.036	0.333	1.01	1.03	1.02	1.04
1.39	0.042	0.038	0.042	0.041	0.042	0.038	0.040	0.500	1.00	1.02	1.02	1.01
1.54	0.044	0.040	0.043	0.043	0.043	0.041	0.042	0.667	0.935	0.980	0.980	0.945
2.23	---	0.045	0.045	0.045	0.044	0.043	0.042	0.750	0.795	0.831	0.830	0.798
2.92	0.043	0.043	0.041	0.041	0.039	0.039	0.039	0.817	0.645	0.680	0.666	0.648
3.61	---	0.040	0.037	0.037	0.034	0.035	0.035	0.882	0.444	0.492	0.508	0.480
4.30	0.036	0.036	0.032	0.032	0.030	0.031	0.030	0.946	0.306	0.314	0.318	0.316
4.99	0.033	0.033	0.029	0.029	0.028	0.028	0.027	1.01	0.173	0.172	0.189	0.183
5.68	0.030	0.031	0.026	0.026	0.025	0.025	0.025	1.08	0.0795	0.0725	0.0810	0.0820
6.37	0.029	0.028	0.023	0.024	0.023	0.022	0.022	1.14	0.0542	0.0537	0.0643	0.0618
7.06	0.027	0.027	0.022	0.022	0.021	0.021	0.020	1.23	0.0420	0.0459	0.0486	0.0491
7.75	---	0.026	0.021	0.020	0.018	0.019	0.018	1.56	0.0419	0.0455	0.0460	0.0456
8.44	0.025	0.025	0.019	0.019	0.017	0.017	0.017	1.90	0.043	---	0.0428	0.0411
9.13	0.024	0.024	0.019	0.018	0.015	0.016	0.016	2.23	0.0394	0.0386	0.0394	0.0384
9.82	---	0.023	---	0.018	0.015	0.015	0.015	2.56	0.0385	0.0372	0.0365	0.0350
10.51	---	0.023	0.017	0.017	0.014	0.015	0.014					
11.03	---	0.023	0.017	0.016	---	---	---					
11.19	---	---	---	---	0.014	0.014	0.014					
11.54	0.022	0.022	0.016	0.016	---	---	---					
11.94	---	---	---	---	0.013	0.013	0.013					
12.08	0.021	---	0.015	0.015	---	---	---					
12.75	0.016	---	0.014	0.014	---	---	---					

TABLE V
HEMISPHERE CYLINDER HEAT-TRANSFER DATA

Model →	Hemisphere-Cylinder															
d, in.	5.8															
Tunnel	B								C							
M_∞	7.92		7.97		7.99		8.01		10.07		10.10		10.14		10.16	
$Re_\infty \times 10^{-6}$, in.$^{-1}$	0.08		0.15		0.23		0.29		0.043		0.058		0.087		0.124	
$\rho_\infty \times 10^{6}$, lb_m/ft^3	672		1180		1760		2270		246		337		513		739	
u_∞, fps	3660		3790		3810		3860		4520		4590		4670		4740	
H_o, Btu/lb_m	289		309		312		322		412		423		437		449	
p_o, psia	203		394		597		801		353		505		808		1209	
T_o, °R	1200		1280		1300		1340		1720		1760		1820		1870	
St_s	0.100		0.077		0.063		0.056		0.180		0.155		0.127		0.110	
S/R	$\left(\frac{St}{St_s}\right)_+$	$\left(\frac{St}{St_s}\right)_-$	$\left(\frac{St}{St_s}\right)_+$	$\left(\frac{St}{St_s}\right)_-$	$\left(\frac{St}{St_s}\right)_+$	$\left(\frac{St}{St_s}\right)_-$	$\left(\frac{St}{St_s}\right)_+$	$\left(\frac{St}{St_s}\right)_-$	$\left(\frac{St}{St_s}\right)_+$	$\left(\frac{St}{St_s}\right)_-$	$\left(\frac{St}{St_s}\right)_+$	$\left(\frac{St}{St_s}\right)_-$	$\left(\frac{St}{St_s}\right)_+$	$\left(\frac{St}{St_s}\right)_-$	$\left(\frac{St}{St_s}\right)_+$	$\left(\frac{St}{St_s}\right)_-$
0	1.000	1.000	1.000	1.000	1.000	1.000	1.000	1.000	1.000	1.000	1.000	1.000	1.000	1.000	1.000	1.000
0.09	1.011	0.990	0.984	1.008	1.018	0.985	1.015	0.981	0.998	0.999	0.986	0.981	1.001	0.994	0.986	0.988
0.17	1.003	---	---	1.003	1.017	---	1.004	0.770	0.970	0.991	0.959	0.973	0.962	0.991	0.927	0.996
0.35	0.903	0.882	0.892	0.911	0.914	0.894	0.900	0.871	0.895	0.902	0.888	0.896	0.893	0.902	0.876	0.907
0.52	0.794	0.771	0.788	0.803	0.805	0.782	0.794	0.767	0.795	0.802	0.792	0.799	0.795	0.804	0.776	0.792
0.70	---	0.650	0.663	---	---	0.657	---	0.653	0.680	0.659	0.674	0.642	0.676	0.649	0.654	0.635
0.87	0.470	0.482	0.491	0.483	0.485	0.492	0.479	0.484	0.513	0.483	0.494	0.479	0.501	0.482	0.492	0.472
1.05	0.333	0.338	0.345	0.342	0.342	0.347	0.336	0.340	0.352	0.352	0.339	0.343	0.361	0.345	0.347	0.334
1.22	0.223	0.232	0.238	0.227	0.226	0.242	0.221	0.235	0.238	0.225	0.235	0.219	0.251	0.227	0.242	0.222
1.40	---	0.149	0.147	---	---	0.150	---	0.144	0.156	0.152	0.152	0.147	0.149	0.152	0.148	0.145
1.57	0.078	0.081	0.082	0.076	0.078	0.085	0.074	0.061	0.090	0.083	0.086	0.079	0.092	0.081	0.084	0.077
1.74	0.058	0.059	0.059	0.057	0.058	0.061	0.055	0.059	0.072	0.062	0.066	0.055	0.062	0.060	0.054	0.056
1.92	0.050	0.055	0.054	0.054	0.053	0.055	0.051	0.055	0.057	0.059	0.054	0.058	0.054	0.055	0.054	0.053

TABLE V (Concluded)

Model	Hemisphere-Cylinder													
d, in.	4													
Tunnel	F													
M_∞	18.1		18.2		19.0		19.3		19.3		19.8		20.1	
$Re_\infty \times 10^{-6}$, in.$^{-1}$	0.02317		0.02563		0.00748		0.00820		0.00830		0.00952		0.01312	
$\rho_\infty \times 10^6$, lb_m/ft^3	74.2		79.5		26.2		26.8		27.5		28.5		35.6	
u_∞, fps	8470		8220		10170		9900		9930		9490		8790	
H_o, Btu/lb_m	1450		[illegible]		2090		1990		1990		1820		1560	
p_o, psia	8170		8140		6810		7000		7080		7210		7360	
T_o, °R	5000		4740		7050		6710		6750		6200		5370	
St_s	0.0319		0.0401		0.0925		0.0736		0.109		0.0792		0.0506	
S/R	$\left(\frac{St}{St_s}\right)_+$	$\left(\frac{St}{St_s}\right)_-$	$\left(\frac{St}{St_s}\right)_+$	$\left(\frac{St}{St_s}\right)_-$	$\left(\frac{St}{St_s}\right)_+$	$\left(\frac{St}{St_s}\right)_-$	$\left(\frac{St}{St_s}\right)_+$	$\left(\frac{St}{St_s}\right)_-$	$\left(\frac{St}{St_s}\right)_+$	$\left(\frac{St}{St_s}\right)_-$	$\left(\frac{St}{St_s}\right)_+$	$\left(\frac{St}{St_s}\right)_-$	$\left(\frac{St}{St_s}\right)_+$	$\left(\frac{St}{St_s}\right)_-$
0.524	0.787		0.771		0.796		0.791		0.791		0.786		0.759	
0.873		0.485		0.495		0.494		0.484		0.484		0.486		0.503
1.57		0.0773		0.0782		0.0734		0.0736		0.0798		0.0767		0.0744
1.82	0.0579		0.0556		0.0564		0.0531		0.0609		0.0584		0.0571	
2.32		0.0501		0.0478		0.0468		0.0464		0.0510		0.0488		0.0470
2.82	0.0397		0.0370		0.0398		0.0303		0.0431		0.041[illegible]		0.0406	
3.32		0.0373		0.0362				0.0358		0.0376				0.0345
4.07	0.0320		0.0292				0.0332		0.0310				0.0275	
5.07	0.0248		0.0242				0.0264		0.0262				0.0239	
5.57	0.0251		0.0213				0.0226	0.0218	0.0239	0.0249			0.0214	0.0230
6.32	0.0202		0.0193				0.0197		0.0212				0.0187	
7.07	---		---					0.0184		0.0205				0.0195
8.07	0.0177		0.0151				0.0160		0.0172				0.0158	
9.07	0.0142		0.0238				0.0144		0.0164				0.0145	
11.57		0.0145		0.0136				0.0126		0.0151				0.0127
12.82	0.0126		0.0112				0.0118		0.0133				0.0109	
14.57	0.0103		0.0099						0.0113				0.0100	

TABLE VI
FLAT-FACE CYLINDER AND ROUNDED-SHOULDER FLAT-FACE CYLINDER HEAT-TRANSFER DATA

Model →	Flat-Face Cylinder					Flat-Face Cylinder					Rounded-Shoulder Flat-Face Cylinder			
d, in.	5.8					6					6			
Tunnel	C					H					H			
M_∞	10.04		10.07			17.9	19.0	20.6	21.1		18.5	18.8	20.4	20.7
$Re_\infty \times 10^{-6}$, in.$^{-1}$	0.026		0.043			0.01034	0.01105	0.00448	0.00542		0.00804	0.01229	0.00410	0.00458
$\rho_\infty \times 10^6$, lb_m/ft^3	147		245			65.5	63.0	24.0	25.7		49.3	65.6	21.8	22.5
u_∞, fps	4440		4520			10050	10080	11160	10290		10310	9340	10840	10370
H_o, Btu/lb_m	399		413			2050	2060	2520	2140		2150	1770	2370	2170
p_o, psia	201		353			7550	9420	7840	7020		7190	7470	6160	5930
T_o, °R	1660		1720			6900	6900	8350	7200		7240	6000	7940	7330
St_s	0.121		0.096			0.0249	0.0182	0.0271	0.0266		0.0209	0.0224	0.0266	0.0288
S/R	$(St/St_s)_+$	$(St/St_s)_-$	$(St/St_s)_+$	$(St/St_s)_-$	S/R	$(St/St_s)_-$	$(St/St_s)_-$	$(St/St_s)_-$	$(St/St_s)_-$	S/R	$(St/St_s)_-$	$(St/St_s)_-$	$(St/St_s)_-$	$(St/St_s)_-$
0	1.000	1.000	1.000	1.090	0.333	0.995	1.000	1.010	1.040	0.333	1.01	1.06	1.03	0.96
0.09	1.031	1.029	0.999	1.037	0.500	1.05	1.01	1.01	1.08	0.500	1.10	1.09	1.10	1.14
0.17	1.029	1.012	0.996	1.018	0.666	1.12	1.02	1.11	1.11	0.666	1.24	1.27	1.43	---
0.26	1.002	1.026	0.963	1.034	0.833	1.20	1.08	1.24	1.28	0.750	1.54	1.40	1.52	1.49
0.34	1.075	1.030	0.994	1.019	1.17	0.0706	0.0750	0.109	0.104	0.917	1.50	1.33	1.50	1.61
0.43	---	1.038	---	1.090	1.50	0.106	0.111	0.135	0.138	0.[illegible]82	1.14	1.06	1.20	1.17
0.52	1.160	1.148	1.078	1.119	1.83	0.126	0.127	0.143	0.149	0.940	0.750	0.785	0.805	0.890
0.60	1.153	1.182	1.064	1.154	2.16	0.119	0.124	0.128	0.137	1.01	0.430	0.438	0.454	0.498
0.69	1.220	1.264	1.138	1.232	2.50	0.116	0.106	0.125	0.126	1.08	0.208	0.171	0.231	0.217
0.78	1.255	1.362	1.208	1.317						1.14	0.181	0.154	0.181	0.206
0.86	1.289	1.446	1.295	1.427						1.23	0.134	0.122	0.137	0.182
0.95	---	1.175	---	1.111						1.56	0.116	0.104	0.113	0.121
1.09	0.100	0.095	0.094	0.091						1.90	0.099	0.093	0.098	0.104
1.17	0.064	---	0.067	---						2.23	0.095	0.083	0.092	0.098
1.26	0.056	0.089	0.049	0.082						2.56	0.086	0.075	0.090	0.081

Security Classification

DOCUMENT CONTROL DATA - R & D

(Security classification of title, body of abstract and indexing annotation must be entered when the overall report is classified)

1. ORIGINATING ACTIVITY (Corporate author) Arnold Engineering Development Center ARO, Inc., Operating Contractor Arnold Air Force Station, Tennessee	2a. REPORT SECURITY CLASSIFICATION UNCLASSIFIED 2b. GROUP N/A

3. REPORT TITLE

COMPARISON OF THEORETICAL AND EXPERIMENTAL PRESSURE AND HEAT-TRANSFER DISTRIBUTIONS ON THREE BLUNT NOSED CYLINDERS IN HYPERSONIC FLOW

4. DESCRIPTIVE NOTES (Type of report and inclusive dates)
Summary Report

5. AUTHOR(S) (First name, middle initial, last name)

R. K. Matthews and R. H. Eaves, Jr., ARO, Inc.

6. REPORT DATE	7a. TOTAL NO. OF PAGES	7b. NO. OF REFS
September 1967	84	47

8a. CONTRACT OR GRANT NO. AF 40(600)-1200 b. PROJECT NO. c. Program Element 65402234 d.	9a. ORIGINATOR'S REPORT NUMBER(S) AEDC-TR-67-148 9b. OTHER REPORT NO(S) (Any other numbers that may be assigned this report) N/A

10. DISTRIBUTION STATEMENT
This document is subject to special export controls and each transmittal to foreign governments or foreign nationals may be made only with prior approval of AEDC (AETS), Arnold Air Force Station, Tennessee.

11. SUPPLEMENTARY NOTES	12. SPONSORING MILITARY ACTIVITY
Available in DDC	Arnold Engineering Development Center, Air Force Systems Command Arnold Air Force Station, Tenn.

13. ABSTRACT

Pressure and heat-transfer data over flow-aligned cylinders with three nose shapes (hemisphere, flat-face, and rounded-shoulder flat-face) have been obtained at nominal Mach numbers of 6, 8, 10, and 19 and over the Reynolds number range of 0.009×10^6 to 2.16×10^6, based on model diameter. The experimental pressure and heat-transfer distributions are compared with theoretical predictions and with selected previously published data from other facilities. The agreement between the experimental results and selected theories for the hemisphere cylinder model is good. However, the pressure and heat-transfer distributions on the other two configurations could not be adequately predicted over the entire model surface.

This document is subject to special export controls and each transmittal to foreign governments or foreign nationals may be made only with prior approval of Arnold Engineering Development Center (AETS), Arnold Air Force Station, Tennessee.

DD FORM 1 NOV 65 1473

Security Classification

14. KEY WORDS	LINK A		LINK B		LINK C	
	ROLE	WT	ROLE	WT	ROLE	WT
hypersonic flow						
blunt nosed cylinders						
heat-transfer distributions						
structural loadings						
vehicle performance						